An Investigation of the Stability and Characteristics of Plasma Generated at the Focus of a Continuous-Wave Microwave Beam

by

Adrian Lopez

A dissertation submitted in partial fulfillment
of the requirements for the degree of
Doctor of Philosophy
(Nuclear Engineering and Radiological Sciences)
in the University of Michigan
2019

Doctoral Committee:

Professor John Foster, Co-Chair
Dr. Remington Reid, Co-Chair
Professor Ronald Gilgenbach
Professor Mark Kushner

Adrian Lopez

alopz@umich.edu

ORCID iD: 0000-0003-3652-7747

Para mi mamá,

Sin ella, esto no hubiese sido realidad.

To Emily,

My wonderful wife and best friend.

To my daughter Maryn,

Can’t wait to welcome you to this world.

Acknowledgements

First and foremost, I must thank my research advisors, Professor John Foster and Dr. Remington Reid, for their guidance, support, and mentorship over the last few years. It was Professor Foster's enthusiastic lectures and passion for plasmas that made the complex topics of plasma physics easier to understand when I was an undergraduate; this is also one of the reasons why I applied to do my Ph.D. research under his aegis. Professor Foster also arranged for me to complete my dissertation work at the Air Force Research Laboratory (AFRL) under another great mentor, and for that, I am grateful. Dr. Remington Reid has been a great mentor and friend over the last two years I have been working under him at the AFRL. I could not have asked for better mentors. I would also like to thank Professors Ron Gilgenbach and Mark Kushner for being part of my doctoral committee and making the plasma courses enjoyable; I actually had the privilege to take NERS 575 the last year Professor Gilgenbach taught the class.

I would like to thank all my friends and colleagues who have supported me throughout my time at Michigan and the AFRL. I would like to give special thanks to Dr. Alexander Englesbe, Kenneth Engeling, Dr. Ted Lane, Dr. Ryan Phillips, and Yao Kovach for making my Ph.D. experience a memorable one. I would also like to thank Erin Thornton for setting up the spectroscopy system used in this investigation and for keeping me company in the laboratory during those long experimental campaigns; I am happy that you are joining us as a SMART scholar. A big thank you to Dean Henley who machined and built the translation stage that was an essential component of my experiments. Also, a big thank you to Shuo Huang, from Professor

Kushner's group, who took the time to help me get started with *GlobalKin* to simulate my experiments.

I would like to thank my family who has been supporting and encouraging me in every stage of my academic career. My mother has been the most significant source of inspiration throughout this journey. All this would not have been possible without the hard work and sacrifices she had to endure to provide my siblings and me a better life in this country – ¡gracias mamá! Finally, I would like to thank the other most important woman in my life, my wife, Emily. Thank you for the love, support, and encouragement you have provided me throughout my graduate career. Most importantly thank you for dealing with my long work hours over the past six years. I could not have done this without you. Te amo mucho and can't wait to welcome our daughter Maryn to this world.

Table of Contents

List of Figures

List of Tables

List of Appendices

Appendix

List of Abbreviations

AFRL	Air Force Research Laboratory
CW	continuous wave
ICEPIC	Improved Concurrent Electromagnetic Particle-In-Cell
EEDF	electron energy distribution function
ALP	Automated Langmuir Probe
HPM	high-power microwave
ECR	electron cyclotron resonance
CCD	charge-coupled device
NIR	near-infrared
DAQ	data acquisition
CCD	charge-coupled device
ICCD	intensified charge-coupled device
CRM	collisional radiative model
RMS	root-mean-square

Abstract

Developing accurate simulations requires benchmarking numerical codes against high-quality experimental data. To validate and improve theoretical models of microwave-plasma interactions in free space, the Air Force Research Laboratory (AFRL) designed and constructed an experimental setup to study plasma generated at the focus of a high power continuous-wave (CW) microwave beam. Discharges were sustained in the center of a vacuum chamber far removed from the chamber walls, which helped prevent non-ideal effects, such as contaminants, secondary electron emission, and plasma-induced desorption, from influencing the properties and behavior of the discharge. A thorough description of the behavior and characteristics of the discharges produced in the AFRL's experimental setup is the first step towards producing the high-quality data needed.

Experiments were conducted with gas mixtures of argon, nitrogen, and oxygen at gas pressures ranging from 100 to 200 mTorr. Three types of discharges were observed during these experiments: unstable, quasi-stable, and stable discharges. It was determined that the stability of the discharges could be controlled through adjustments of the gas composition, gas pressure, and power of the microwave beam; the operational conditions in which each of the discharges was observed was documented.

Invasive (electrostatic probe) and non-invasive (optical emission spectroscopy) plasma diagnostic methods were implemented to characterize the discharges generated in the experimental setup. From these studies, it was determined that quasi-stable discharges were driven by instabilities resulting in the periodic propagation of ionization fronts. In stable discharges,

striations were observed in all tested conditions; up to three different striation patterns were observed simultaneously. An anticorrelation of the electron temperature and density along the path of the striations was observed in the measurements of the plasma parameters; this is consistent with behavior reported in the literature of striations in DC, and RF discharges. While the source of the striations is still not fully understood, experimental and simulation results suggest that standing waves within the discharge might be the underlying cause of the striated patterns.

Experimental measurements of the electron temperature and density showed similar trends in all tested gas mixtures (Ar-N_2, Ar-O_2, and Ar-N_2-O_2) as the gas pressure, the concentration of the molecular gas and power of the microwave beam were varied. However, there was disagreement in the electron temperatures measured by the invasive and non-invasive diagnostic systems in discharges containing oxygen. *GlobalKin*, a zero-dimensional plasma kinetics model, was also used to study the plasma parameters of the microwave-driven discharges. Results from the simulations closely agreed with the electron temperatures measured by the non-invasive method, suggesting the presence of oxygen in the discharge affected the measurements of the invasive method. In general, *GlobalKin* simulations showed good agreement with experimental results.

Chapter I

Introduction

1.1 Overview

1.1.1 Motivation

Predictive modeling is a powerful tool in plasma research as it provides investigators with some insight into the characteristics and behavior expected in plasma generated under different conditions. The ability to predict the results of experiments that have not yet been conducted can be viewed as having a thorough understanding of the physical phenomena present in the experiment. However, developing accurate simulations requires benchmarking numerical codes against high-quality experimental data. Most laboratory plasmas are in contact with the surfaces of the chamber walls and plasma sources, which can cause significant uncertainties and errors in experimental measurements. By eliminating the sources of non-ideal effects, such as the bounding surfaces, one can improve the accuracy of experimental measurements.

Minimizing the effects that contaminants have in plasma discharges can help improve the accuracy of measurements of the plasma parameters, such as breakdown thresholds, ionization rates, and diffusion rates. Electrodeless plasmas, such inductively coupled plasmas, eliminate the introduction of contaminants from sputtering of the electrodes; however, the plasma is still subject to contaminants and perturbations from the plasma-wall interactions. The ideal plasma for these types of measurements would be plasma created in free space, which is plasma formed without any contact with walls or electrodes. This kind of plasma can be generated at the focal region of

a laser or microwave beam when the electric field is strong enough to induce gas breakdown; free electrons accelerated by the electric field of the beam transfer their energy to neutral gas molecules via collisions. Generating plasma discharges far removed from bounding wall surfaces, help prevent non-ideal effects, such as contaminants, secondary electron emission, and plasma-induced desorption, from influencing the properties and behavior of the discharges. Note that plasma generated in the focus of a beam approaches the free space condition as the distance from the edge of the discharge to the nearest wall gets much larger than the characteristic lengths of the discharge, such as the wavelength of the beam, diffusion length, and collisional mean free path to name a few.[1]

In an effort to study microwave-driven free space plasma (also known as free-localized microwave discharges) in laboratory conditions, scientists at the Air Force Research Laboratory (AFRL) in Kirtland Air Force Base, NM designed and constructed an experimental setup capable of generating plasma that approaches free space conditions. The discharges are generated at the focus of a multi-kilowatt, 4.7 GHz continuous-wave (CW) microwave beam far from the chamber walls; the radius of the chamber is approximately 10 times larger than the wavelength of the microwave beam, which puts the edge of the plasma at approximately 8 to 9 wavelengths away from the nearest wall. The discharges could also have been generated with a pulsed power beam, but the short lifetimes of pulsed microwave plasmas make them more challenging to diagnose than plasmas sustained in steady state. While experiments conducted with pulsed microwave sources can provide useful information on the plasma parameters as the discharge evolves through the duration of the pulse (typically in the nanosecond to microsecond time-scale), they lack detail on the long-term (millisecond to hour time-scales) stability and characteristics of free space plasma.

During initial testing of the experimental setup, two types of discharges were observed: a stable discharge whose size, shape, and brightness remained constant over extended periods (hours), and a quasi-stable discharge whose shape, position, and brightness oscillated in time; images captured of the discharges during this set of experiments are shown in Fig. 1.1.[2] This thesis investigation is a continuation of the experiments conducted by Hoff *et al.* and the AFRL's efforts to understand the behavior and characteristics of microwave-driven free space plasmas.[2] Understanding what factors affect the stability, appearance, and characteristics of the discharges generated in the AFRL's experimental setup is the first step towards a better understanding of the physical phenomena present in the discharge (e.g., striations), and the generation of high quality data that can be used for the validation and improvement of theoretical models, such as the Improved Concurrent Electromagnetic Particle-In-Cell (ICEPIC) code developed by the AFRL.

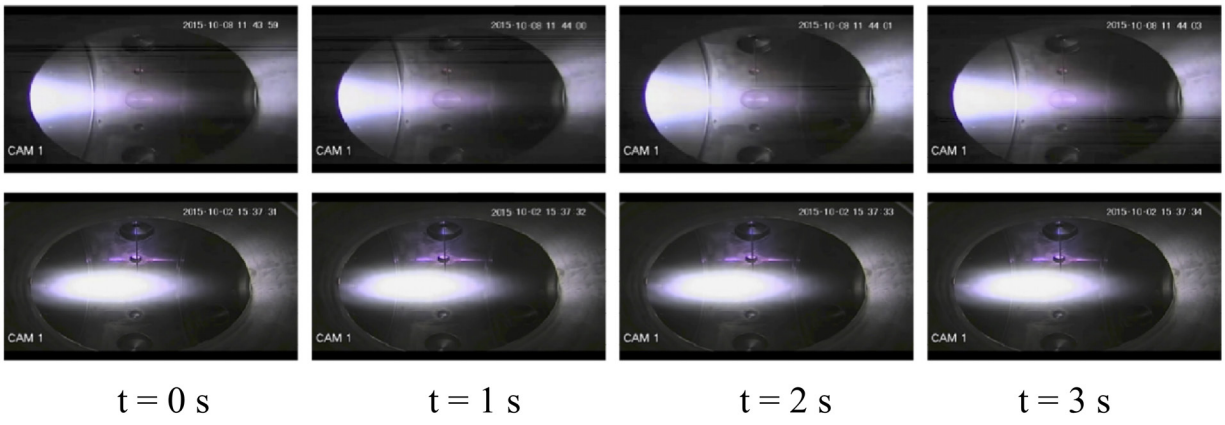

Figure 1.1: Visual comparison of the quasi-stable (top row) and stable (bottom row) discharge modes. From left to right, the images are taken at 1 s intervals. The quasi-stable discharge noticeably changes in brightness and extends while the stable discharge remains at a constant brightness for a given RF power level. Discharges generated were approximately 45-60 cm in length with a 20-30 cm diameter. Reprinted from B. W. Hoff *et al*., *Rev. Sci. Instrum*. **87**, 033507 (2016), with the permission of AIP Publishing.

1.1.2 Unanswered Questions

At the beginning of this investigation, little was known of the discharges that could be generated in the experimental setup at the AFRL. During preliminary testing, stable and quasi-stable argon discharges were observed in the experimental setup by Hoff *et al*.; however, it was

unclear what factors determined the discharge mode one would observe.[2] During testing, it was noted that the stable discharges could not be obtained when the base pressure of the vacuum chamber was below 10^{-5} Torr before testing. This suggested that contaminants (air molecules and trapped moisture) in the argon discharge played an important role in determining the stability of the discharge. To test this hypothesis, additional mass flow controllers were added to the experimental setup to introduce molecular gases (nitrogen and oxygen) into the argon discharge in a controlled manner. Results from these preliminary experiments with added nitrogen made it clear that adding a molecular gas indeed helped stabilize the discharge, but it was unclear how much of an impact the other control parameters, such as the power of the microwave beam and gas pressure, had on the stability of the discharge. Furthermore, not much was known about the electron temperature and density of the discharges and how they were affected by changes in the gas composition, pressure, and power of the microwave beam.

The discharges generated at the AFRL's experimental setup were not well understood, so the primary objective of this investigation was to address the following questions:

1. What is the general behavior of the instabilities in the discharge?
2. Are they controllable? If so, under what conditions is stability of the discharge achieved?
3. What are the origins of the striations on the stable discharges?
4. How are the characteristics (electron temperature and density) and appearance (brightness and size) of the stable striated discharges affected by changes in the gas composition, pressure, and power of the microwave beam?

Understanding the underlying control parameters will allow for better predictions and control of the characteristics and stability of CW microwave-driven free space plasmas.

1.1.3 Structure of the Dissertation

To address the aforementioned questions in a comprehensive manner, an overview of the research approach taken to answer these questions is first provided in the next section. There, the plasma diagnostic methods considered for this investigation are discussed to provide some insight into how the diagnostic methods used for this investigation were selected. A literature review of CW and pulsed microwave discharges in conditions that approach free space is provided in Sect. 1.3 in order to develop the appropriate context for this work; the review covers from the first recorded experiment of a localized microwave discharge in 1960 to the most recent set of millimeter-wave discharge experiments.

Details of the experimental setup and diagnostic systems used in this investigation are provided in Chapter II. Chapter III expands on the plasma diagnostic methods and theory used for analysis of the data collected. A brief background on sheath formation is provided along with a thorough discussion of the probe theory used for calculations of the electron temperature and density. In the optical emission spectroscopy section, a brief review of a few selected quantum mechanics topics is provided for readers not familiar with spectroscopy notation, atomic processes, and molecular spectra. A thorough discussion of the collisional radiative model and molecular spectra models used for calculations of the electron temperature and gas temperature is then provided.

The last three chapters of the dissertation discusses the results of this investigation and areas in the field that will be explored in the future. Chapter IV discusses the stability and behavior of microwave-driven discharges generated under various gas compositions, pressures, and microwave beam powers; the operational conditions in which stable discharges can be generated are defined. Stable discharges within the defined boundaries are then characterized through

experimental and theoretical results in Chapter V; a correlation between oscillatory features on the triple probe measurements and the striated pattern observed on the stable discharges is then made. The dissertation concludes with a summary of the results and a discussion of the future of CW microwave plasma research at the AFRL.

1.2 Research Approach

1.2.1 Selection of Plasma Diagnostic Methods

Preliminary measurements of a stable argon discharge were made with a single Langmuir probe and a low-resolution spectrometer by Hoff *et al.*, so the initial plan was to replicate the measurements; however, with a great variety of invasive and non-invasive plasma diagnostic methods available, the first task was to determine which methods would work best with the experimental setup.[2] Electrostatic probes are the simplest and most economical systems to build that can provide some insight into the plasma parameters, such the electron temperature and density, at the cost of localized disturbances to the plasma and microwave beam. There are several electrostatic probe designs and methods, each of them with their advantages and disadvantages. Single Langmuir probes are the most common type of electrostatic probe used in plasma diagnostics as it not only provides information about the electron temperature and density, but also of the plasma potential, floating potential, and electron energy distribution function (EEDF).[3]–[11] However, Langmuir probes must be biased against a reference electrode that is also immersed in the plasma, otherwise, the current drawn by the probe would not return to the system; the plasma must complete the circuit between the probe and the reference electrode. This means single probes cannot be used to characterize electrodeless free space discharges without introducing a secondary reference probe.

Adding a reference wire to the single probe (making it a double probe) for measurements of the electron temperature and density was first proposed by Johnson and Malter in 1950.[12] Similar to single probes, a voltage sweep must be performed to measure the current-voltage characteristic, which is used to determine the electron temperature and density of the discharge.[12]–[15] Unlike single probes, the EEDF cannot be determined from double probe measurements unless the surface area of the reference probe wire is several thousand times larger than the measuring probe wire (ratio depends on the mass of the ions); the ion current to the larger reference probe must be able to match the electron current over the whole energy range of the EEDF.[16]–[19] The required surface area ratio of an asymmetrical double probe is so large that even when using a relatively thin wire (diameter in the order of a tenth of a millimeter) the surface area of the reference probe would be so large that it would significantly perturb the plasma and microwave beam. This makes any asymmetrical multi-tip probe unusable for the characterization of the discharges generated in the AFRL's experimental setup.

The symmetrical double probe could still be used but given that it can only provide information of the electron temperature and density of the plasma, adding a third wire to the double probe to make a symmetrical triple probe was a much better option. The triple probe can take instantaneous measurements of the electron temperature, and density as no voltage sweep is required. The response time of the probe is in the order of microseconds, which is fast enough to detect the oscillations in the quasi-stable discharge observed by Hoff *et al*.; the fact that the flickering of the discharge was observed through a video camera meant that the oscillations were occurring in the millisecond timescales (10s of Hertz).[2] Furthermore, batteries can be used as the voltage source of the probe, which helps eliminate electrical noise from the power supply.

More details of the triple probe system constructed for this investigation can be found in Sect. 2.2; probe theory used to analyze the data is discussed in Sect. 3.1.

While triple probes were a great option to begin the characterization of the plasma, they are invasive (perturb the plasma and microwave beam) and are subject to significant measurement errors due to the arbitrariness of ion current approximations and deviations of the EEDF from Maxwellian.[11], [20]–[22] To assess the effects of triple probe perturbations on the plasma, experiments were also conducted with an optical emission spectroscopy system to measure the electron temperature without perturbing the plasma and microwave beam. From the spectral measurements, the gas temperature was also determined from nitrogen's rovibrational bands in the visible spectrum. Non-invasive measurements of the electron density were also planned using microwave interferometry. However, a combination of the expected low electron densities (10^{14} to 10^{16} m^{-3}), the relatively long plasma path (approximately 25 cm) between the transmitting and receiving horn antennas, and the hardware needed to resolve features of interest (striations) in the discharge, made it challenging to design a system within budget that could work with the experimental setup.

1.2.2 Planning of Experiments

The experimental setup control parameters included the microwave beam power, gas composition, gas pressure, and gas flow rate. To study the behavior of quasi-stable discharges, an optical fast frame rate camera was first used to capture images of an argon discharge to explore the flickering of the discharge observed by Hoff *et al*.[2] A triple probe system was then integrated to the experimental setup to study the oscillatory behavior of the quasi-stable discharge. The effect of the gas flow rate on discharge behavior was also investigated; gas flow rate was kept constant for all experiments proceeding this one based on the findings of the study. Unfortunately, the

plasma diagnostic systems used in this investigation were unable to properly characterize the quasi-stable discharge; however, the limited information (traces of the electron temperature and density) gathered through the diagnostic systems did provide some insight into the behavior and characteristics of the discharge.

Experiments with stable discharges were significantly more straightforward to plan as the discharge could be sustained in steady-state for extended periods of times (hours). A linear translation stage was added to the experimental setup allowing the diagnostic systems to make measurements along the axis of the plasma. Experiments were first conducted to determine the lower and upper gas pressure limits at which stable discharges could be sustained in the presence of a triple probe; 100 mTorr and 200 mTorr were determined to be the limits for the experimental setup. The next phase of the investigation was to determine the concentrations of nitrogen and oxygen that could be added to the argon discharge before it was no longer sustainable; the concentrations of the molecular gases were adjusted in increments of 2%. The range of the microwave beam power for which the discharge was stable was also determined at each of the tested gas pressures and compositions by decreasing the beam power 500 W at a time starting from maximum power; triple probe measurements were made at every tested condition. This procedure was repeated with the optical emission spectroscopy system for comparison purposes. Finally, a zero-dimensional global-kinetics model was used to simulate the tested conditions and provide some insight into the electron temperature and density expected solely on the chemical kinetics of the discharge. The densities of species acquired in this work, such as ions and excited states of atoms and molecules, were also valuable with regards to model validation and understanding the experimentally determined response of the discharge.

1.3 Prior Investigations

1.3.1 CW Microwave Discharges

To the author's knowledge, there has been only one other experimental setup (reported in literature) in which CW microwaves were used to generate discharges removed from chamber wall surfaces; note that there has been extensive studies in CW microwave cavity discharges, but they are far from approaching free space conditions.[23]–[26] In 1962, Allison *et al*. reported producing a striated argon discharge with a 2 kW, 8.8 GHz CW microwave source at pressures ranging from 500 mTorr to 400 Torr; a picture of the observed discharge is shown in Fig. 1.2.[27] However, the edge of the discharge was only a few centimeters away from the nearest glass wall making unclear if there were any non-ideal effects present on the discharge due its proximity to the chamber walls. Furthermore, the thickness of the glass chamber is not reported, so it is unclear how much of the microwave beam is being reflected by the glass walls. The authors only reported on the visible appearance of the argon discharge as gas pressure, and power of the microwave beam were varied; information on the purpose of the experiment and the plasma parameters was not reported.[27]

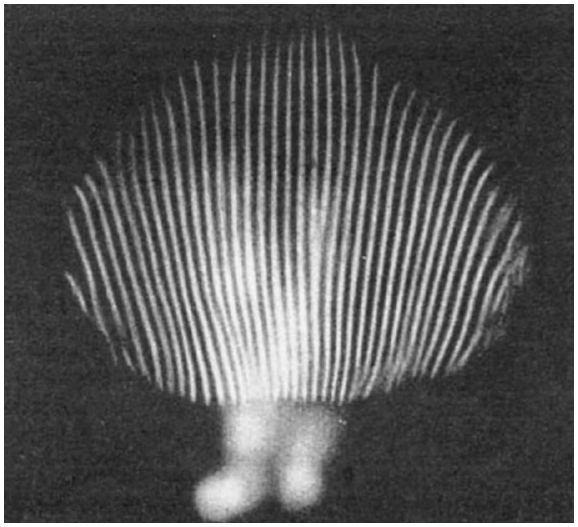

Figure 1.2: Stable striated argon discharge reported by Allison *et al*. The discharge is roughly a spheroid with a major axis of approximately 60 cm and minor axis of about 10 cm.[27]

While the operational conditions of their experiments were different from the ones in the AFRL's experimental setup, the reported observations did provide some insight into the features and behaviors one could expect from CW microwave discharges. For example, they were able to generate stable argon discharges at the focus of a CW microwave beam as they varied the power of the beam and gas pressure. Also, they were unable to sustain the discharge in a 2-kW beam when the gas pressure was reduced below 500 mTorr. They also observed striations in the discharge, but their origins were unclear. A comparison of the operational conditions between the AFRL's experimental setup and the one reported in literature by Allison *et al.* is shown in Fig. 1.3. [27]

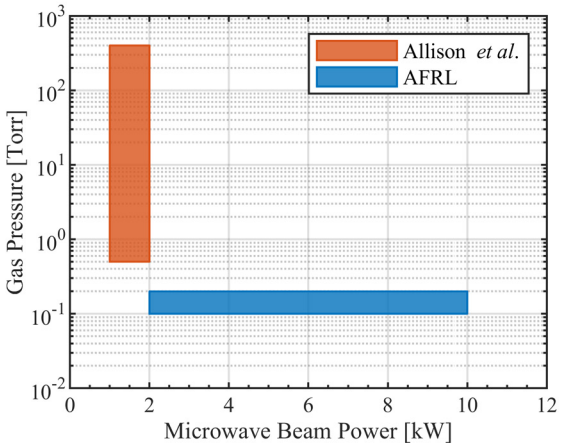

Figure 1.3: Operational conditions of experiments conducted in the AFRL's and Allison *et al.* setups.[27]

1.3.2 Pulsed Microwave Discharges

There have been many experimental studies on the characteristics and instabilities of free space plasma generated by pulsed microwave sources. In 1960, Hamilton reported generating a localized pulsed microwave air discharge at the focal region of a parabolic reflector.[28] While the author claimed the discharge was isolated from the glass walls of the discharge vessel, it is unlikely that the conditions of the experimental setup approached those of free space as the plasma was only a few centimeters away from the glass chamber wall. Furthermore, Hamilton reported

that the discharge was perturbed by reflections of the microwaves within the glass chamber, indicating the chamber influenced the behavior of the discharge.[28] It was not until the 1980s that experimental research of microwave-driven discharges that approached the free space condition started to be published by different institutions. Many of these investigations were conducted at the Institute of General Physics in Russia, where they built an experimental setup capable of generating discharges that approached the free space conditions; a diagram of the experimental setup is shown in Fig. 1.4.[29]–[34] Most of the reported studies on this experimental setup focused on the breakdown thresholds of air, the time evolution of species in the plasma, and plasma chemical reactions. While these studies did not provide information on stable discharges, they did provide some insight into the behavior observed in CW microwave-driven quasi-stable discharges.

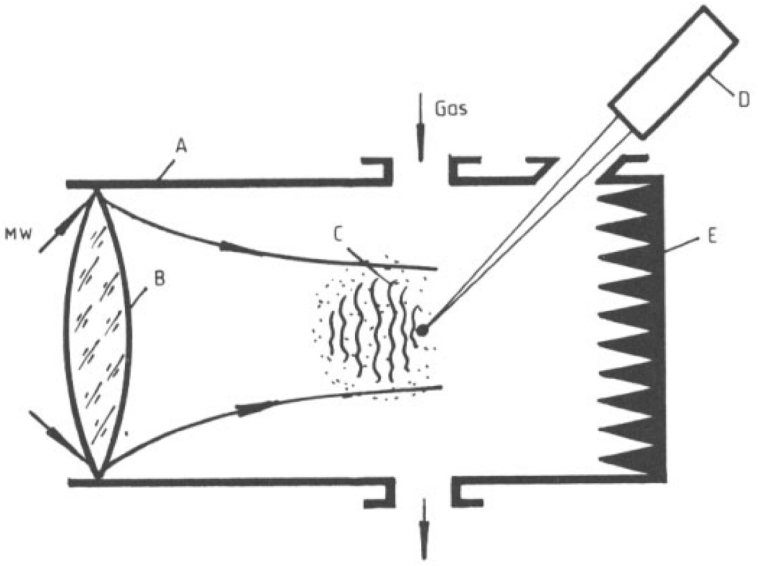

Figure 1.4: Scheme of super-clean plasma chemical reactor: "A" is the vacuum chamber, "B" is the lens, "C" is the microwave discharge, "D" is a CO_2 laser, and "E" is a microwave absorbing load.[29]

Several experimental studies reported observing ionization fronts or plasma filaments propagating towards the source of the microwave beam.[1], [28], [30], [34]–[47] These instabilities occurred as a result of the plasma density exceeding the critical density, which caused

the microwaves to completely reflect off the plasma; depending on the experimental conditions, traveling ionization fronts or self-organizing plasma structures were observed. The behavior of traveling ionization fronts resembles closely the behavior observed in quasi-stable discharges at the AFRL; however, most of the reported ionization fronts did not fully evolve due to the short duration of the microwave pulse. Secondary traveling ionization fronts in helium and nitrogen discharges were observed by Vikharev *et al*. when the duration of the pulse was increased to 100 μs, but it was unclear if the secondary ionization front was similar to the first one like in CW discharges.[42]

Chapter II

Experimental Hardware and Procedure

2.1 Experimental Setup

The experiments discussed in this investigation were conducted using an experimental setup located at the AFRL in Albuquerque, NM. The experimental setup was designed to generate and study free-space microwave-driven plasmas.[2] Plasma diagnostics systems initially implemented in the experimental setup included an Impedans Automated Langmuir Probe (ALP) System and a Thorlabs model CCS200 spectrometer. These plasma diagnostic systems were replaced by a triple Langmuir probe system and a Princeton Instruments SpectraPro HRS-500 spectrometer.

In the experimental setup, a high-power microwave (HPM) system transmits a multi-kilowatt, 4.7 GHz microwave beam through a horn antenna located inside an anechoic chamber. The microwaves propagate through free-space before passing through a metal-plate lens that focuses the microwaves into a beam waist inside a vacuum chamber. Fiberglass vacuum radomes allow the microwave beam to enter and exit the vacuum chamber with minimal incident power losses and reflections. Borosilicate windows protect the vacuum radomes from getting damaged by interactions with the discharges or sharp objects. After the microwave beam exits the chamber, it propagates through free space before being absorbed by a beam dump. The intensity of the microwave beam was not strong enough to breakdown the background gas inside the chamber, so a plasma applicator was used to populate the chamber with seed electrons to facilitate breakdown;

the plasma applicator can be turned off after breakdown. The focused microwave beam couples energy into the seed electrons to generate a localized discharge near the focal point of the beam. The diagnostic systems used to study the discharges are mounted on a linear translation stage located inside the vacuum chamber, allowing plasma parameters to be spatially resolved along the axis of the discharge. A diagram of the experimental setup is shown in Fig. 2.1..

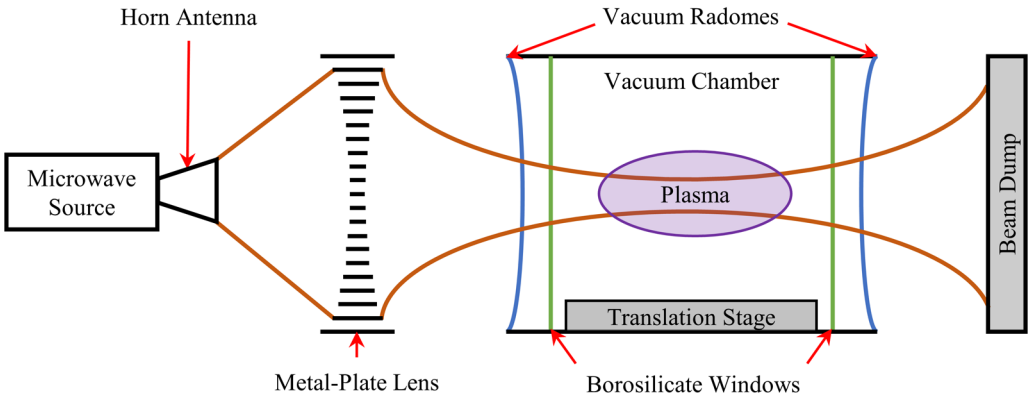

Figure 2.1: Experimental setup used to generate free-space microwave-driven plasma at the AFRL. The cylindrical vacuum chamber is 152 cm in length with an inner diameter of 122 cm.

2.1.1 High-Power Microwave System

The HPM system consists of a local oscillator, a pre-amplifier, and a high-power klystron amplifier. The local oscillator is an HP 8341B Synthesized Sweeper used to generate the 4.7 GHz input signal to be amplified. Super-high-frequency coaxial cable transmits the input signal from the local oscillator to an Empower BBM5K8CGM solid state broadband high-power pre-amplifier that amplifies the signal to meet the minimum power requirements (approximately 5 W) of the klystron. The klystron amplifier is rated for a maximum continuous-wave (CW) output power of 10 kW and a bandwidth of approximately 0.5% at a center frequency that is mechanically tunable between 4.4 and 5.4 GHz.[2] The amplified signal outputs into a WR187 waveguide where the microwaves pass through a 4.95-5.00 GHz band stop filter before being broadcast by a horn antenna inside an anechoic chamber. The band stop filter is required to prevent the HPM system

from interfering with communication systems operating in this frequency range. A water-cooled circulator is connected inline between the klystron amplifier and the band stop filter to protect the klystron amplifier from reflected power. Power reflected into the waveguide is redirected by the circulator into a water-cooled broadband microwave load. A diagram of the HPM system is shown in Fig. 2.2.

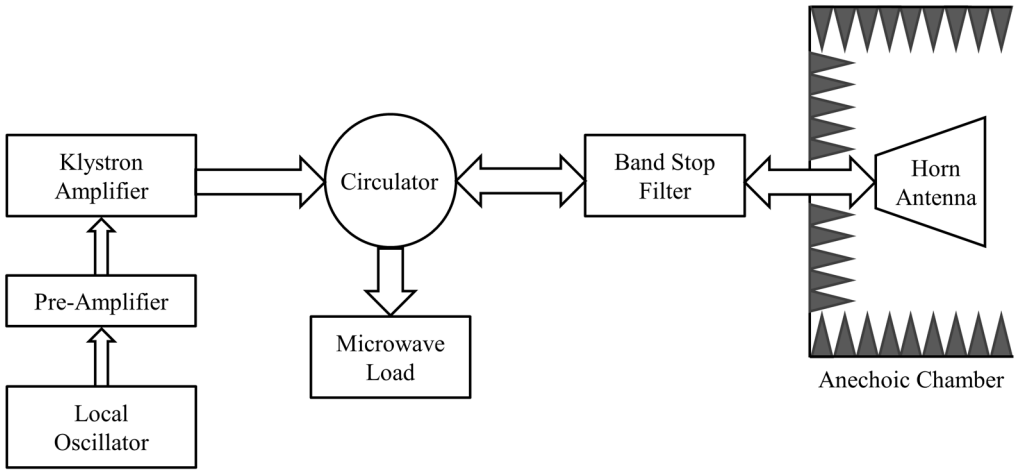

Figure 2.2: Diagram of the high-power microwave system used in the experimental setup.[2] The experimental setup was located inside the anechoic chamber.

2.1.2 Metal-Plate Lens

The microwave lens was designed based on a concept first proposed by Kock in 1946.[48] The metal-plate lens work on the principle that electromagnetic waves assume a wavelength and phase velocity greater than their phase velocity and wavelength in free space when confined to a waveguide. The same effect occurs when microwaves pass in between conductive plates that are parallel to the electric field vector and spaced apart a distance greater than half a wavelength resulting in an index of refraction less than unity. The index of refraction of such medium is given by

$$\mathrm{n} = \frac{c}{\mathrm{v_{ph}}} = \sqrt{1 - \left(\frac{\lambda_0}{2\mathrm{a_p}}\right)^2}, \tag{2.1}$$

where c is the speed of light in free-space, v_{ph} is the phase velocity of the microwaves inside the metal-plate lens medium, λ_0 is the wavelength of the microwaves in free-space, and a_p is the distance between the parallel metal plates.[48]

The array of metal plates used for the lens were cut to a spherical biconcave profile based on the lensmaker's equation for thin lenses,

$$\frac{1}{f} = (n - 1)\left(\frac{1}{R_1} - \frac{1}{R_2}\right), \tag{2.2}$$

where f is the focal length, R_1 is the curvature radius of the front side of the lens, and R_2 is the curvature radius of the back side of the lens. The parallel metal-plates are spaced 3.8 cm apart, so microwaves with a free-space wavelength of 6.4 cm (for 4.7 GHz) experience an index of refraction of approximately 0.54 when propagating through the metal-plate lens medium. The metal-plate lens was designed with a radii of curvature (front and back side of the lens) of 91.4 cm, which resulted in a focal length of 99.2 cm using Eqn. 2.2. Note that for a biconcave lens R_1 is a negative value and R_2 a positive value.

2.1.3 Gas and Vacuum System

The cylindrical vacuum chamber is 152 cm in length with an inner diameter of 122 cm. Vacuum radomes custom-fabricated out of TenCate BTCy-2 serve as the primary pressure boundaries at the ends of the chamber. The material of the vacuum radomes allow microwaves to propagate in and out of the chamber with minimal power losses at frequencies ranging from 4.4 to 5.4 GHz; it absorbs less than 0.1% of the incident power. The borosilicate windows inside the vacuum chamber were designed to withstand pressure differentials of up to 2 Torr while maximizing the transmission of microwaves propagating at frequencies near 5 GHz; thickness of windows are approximately a quarter of the microwave beam's wavelength in free space. The regions between the borosilicate windows and the vacuum radomes are differentially pumped by

a secondary turbopump to maintain the regions at lower pressures (in the order of 10^{-4} Torr) than the rest of the chamber during testing – this prevents plasma from interacting with the vacuum radomes and damaging them.

Precise gas mixtures of argon, nitrogen, and oxygen are fed into the vacuum chamber using Alicat MC gas mass flow controllers; flow rates can be set up to 500 sccm per channel. The gas pressure can be varied between a few millitorr to hundreds of millitorr by a motorized butterfly valve connected in between the vacuum chamber and the primary turbopump. The primary turbopump is water-cooled, which allow the system to sustain background gas pressures of up to 200 mTorr at gas flow rates of up to 350 sccm. Gas flows into the chamber through a CobberMuegge MA300G-012BB plasma applicator that can seed electrons into the vacuum chamber when turned on; the plasma applicator consists of a 3 kW, 2.45 GHz electron cyclotron resonance (ECR) plasma source. As the electrons are accelerated by the electric field of the microwave beam, some gain enough energy to ionize some of the background gas resulting in the formation of a discharge near the geometric focus of the beam. A diagram of the gas and vacuum system is shown in Fig. 2.3.

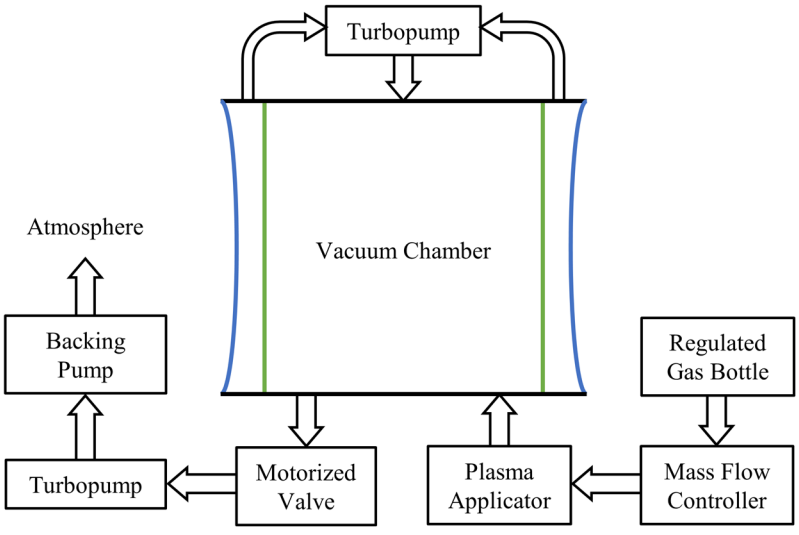

Figure 2.3: Diagram of the gas and vacuum system of the experimental setup.[2] The cylindrical vacuum chamber is 152 cm in length with an inner diameter of 122 cm.

2.1.4 Fast Frame Rate Cameras

A set of Thorlabs 340M-GE fast frame rate cameras were installed as part of an upgrade to the security cameras initially installed when the experiment was first set up. The fast frame rate cameras have an ADC resolution of 14-bits with a charge-coupled device (CCD) pixel clock speed of up to 40 MHz; the framerate of the cameras can vary from 10s to 100s of frames per second depending on the selected binning and clock speed settings. Exposure times can be adjusted in increments of 1 ms, which allow us to study instabilities in the free-space plasma such as the propagation of ionization fronts in quasi-stable discharges. The cameras can also be synchronized with other scientific instruments allowing us to link images captured by the cameras to measurements of our plasma diagnostics systems. There are two regions of interests in our experiments: upstream of the beam's geometric focus where the quasi-stable discharges occur and near the geometric focus where the stable discharges appear. A diagram of the fast frame rate cameras viewing regions is shown in Fig. 2.4.

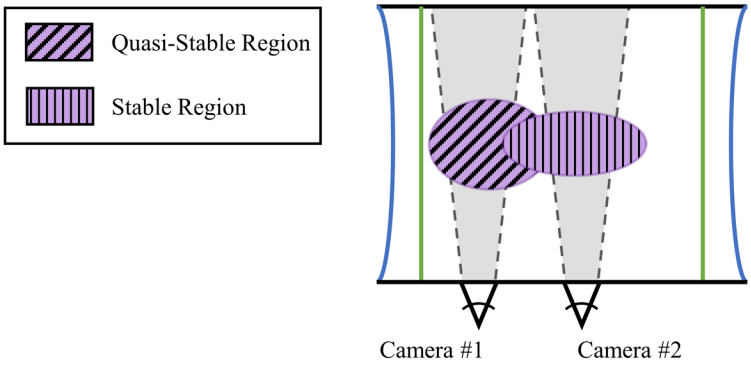

Figure 2.4: Diagram of the regions the fast frame rate cameras monitor within the vacuum chamber.

2.1.5 Translation Stage

A linear translation stage was installed inside the vacuum chamber to be able to sweep electrostatic probes and collection optics along the axis of the chamber. The platform and supporting frame of the translation stage were machined out of aluminum. The platform sits on

the aluminum housings of four linear ball bearings guided by two stainless steel support rail shafts. A Phytron VSS 56.200.1.2 stepper motor rotates a lead screw allowing a lead nut attached to the platform to move along the axis of the chamber. The translation stage has a travel distance of 105 cm, with a 2.5 μm minimum incremental motion. An MCS-2 motion controller from MDC Vacuum is used to adjust the speed and travel distance of the translation stage system. An image of the translation stage is shown in Fig. 2.5.

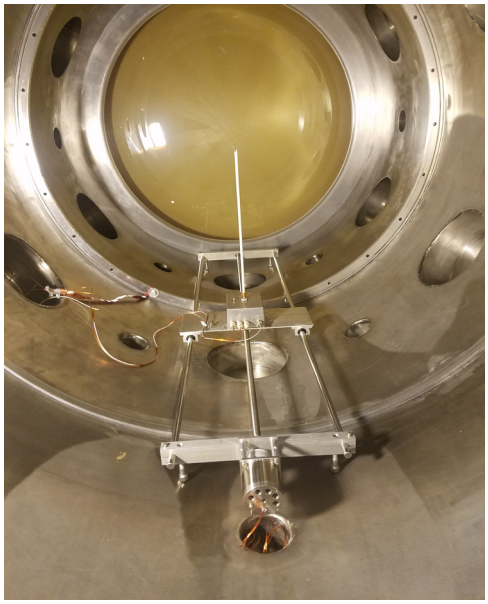

Figure 2.5: Image of the translation stage built to move our plasma diagnostic systems with electrostatic probe installed. The translation stage has a travel range of approximately 105 cm and is about 30 cm wide.

2.1.6 Plasma Diagnostic System

Invasive and non-invasive plasma diagnostic systems were used in this investigation to characterize the plasma generated at the focus of the microwave beam. The diagnostic systems were mounted on the linear translation stage, allowing us to resolve some of the plasma parameters spatially. The invasive diagnostic system consists of an electrostatic triple probe which was used to measure the local electron temperature and density of the plasma. The short intrinsic response time of the triple probe system (on the order of microseconds) in combination with the motion of the linear translation stage facilitates spatially resolved measurements; measurements were made

along the axis of the discharge for all tested conditions. The non-invasive diagnostic system consists of a plasma spectroscopy system which was used to estimate the line-of-sight average electron temperature and gas temperature of the plasma. Collecting spectra in the visible and near-infrared (NIR) wavelength range with our plasma spectroscopy system is time-consuming (approximately 7 minutes per location), so spectral measurements were taken at only a few locations along the axis of the discharge; note that the collection optics line-of-sight is along the radial direction of the discharge. A diagram of the relative locations at which measurements of the plasma parameters were made is shown in Fig. 2.6.

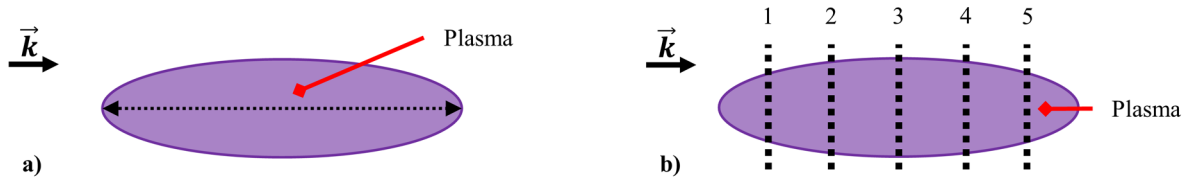

Figure 2.6: Diagram of the **a)** path of the probe (black dotted arrow) and **b)** the line-of-sight of the collection optics (black dotted lines)[1] relative to the microwave beam's propagation vector, $\vec{k}$, and the plasma generated near the focus of a microwave beam. Here location 3 is near the focus of the discharge, locations 1 and 5 are locations where the peak intensity of the 801.5 nm Ar I emission line falls to approximately 10% of the peak intensity, and locations 2 and 4 are halfway in between.

2.2 Triple Probe System

There are various configurations of the triple Langmuir probe, each one with its advantages and disadvantages. For example, asymmetrical triple probes can measure the electron energy distribution function of an electrodeless plasma, but the relatively large current drawn from the lower-energy portion of the EEDF distorts the discharge more severely than in the case of symmetrical probes; the electron current drawn by the symmetrical probe is limited to two times the ion current. Furthermore, asymmetrical triple probes require a reference probe that is

[1] It should be noted that optical emission spectroscopy measurements were made on locations 1-5 only for experiments conducted with Ar-N_2 gas mixtures as no significant changes in the electron temperature were detected along the five different locations. Spectral measurements were taken at locations 1, 3, and 5 for experiments conducted with gas mixtures of Ar-O_2 and Ar-N_2-O_2.

significantly larger than the measuring probe, which can perturb electromagnetic waves in microwave-driven discharges; the reference probe's surface area has to be at least several thousand times larger than the collecting area of the measuring probe for accurate measurements of the EEDF.[16], [49] To select the appropriate configuration, one needs to take into consideration the plasma conditions and parameters of interest; triple probes can be used in conditions ranging from stable electrodeless plasmas to magnetized turbulent plasmas.[13], [16], [49]–[52] The AFRL's experimental setup generates free-space plasma at the focus of a CW microwave beam, which limits the electrostatic probe choices to symmetrical multi-tip probes if one wants to minimize disturbances on the plasma and microwave beam.

2.2.1 Circuit Design

The symmetrical triple Langmuir probe circuit design used in this investigation is based on the instantaneous direct-display system first proposed by Chen and Sekiguchi in 1965.[50] The probe consists of three 1 mm diameter tungsten wires of equal lengths. The wires are fed through the holes of a quad-bore alumina tube leaving approximately 8 mm of the wire length exposed to the plasma. The distance between the exposed probe wires was kept at approximately 2 mm to minimize the effects of spatial variations in the plasma while preventing ion sheaths from overlapping between the wires.

Four 9 V batteries were connected in series to supply a constant voltage potential (V_{d3}) between two of the probe wires as batteries minimizes electrical noise in the measured signals while allowing the biased probes to float with the plasma; the 36 V probe bias is enough to satisfy the probe conditions as it will be discussed in Sect. 3.1. Current flows between the positively biased probe wire (P_1) and the negatively biased probe wire (P_3) when the probe is immersed in a plasma. It is important to note that all the probe wires are biased relative to the plasma floating

potential (V_f) and that all the probe wires sit at a negative potential relative to the plasma space potential (V_s) as shown in Fig. 2.7. The current flowing through the biased probe wires (I_p) can be measured with a differential data acquisition (DAQ) system by placing a resistor in series with the positively biased probe and measuring the voltage drop across it. The resistor's resistance must be high enough to produce a voltage drop that is detectable by the DAQ system, but low enough to minimize voltage losses in the circuit; a 100 Ω resistor was used in this investigation. The third probe wire in the circuit (P_2) is left floating and used as a reference to the biased probe wires. A NI-9229 DAQ was used to measure and record the current flowing through the biased probe wires, and the voltage potential (V_{d2}) between the floating and positive probe wires. A diagram of the triple probe circuit used in our experiments is shown in Fig. 2.8.

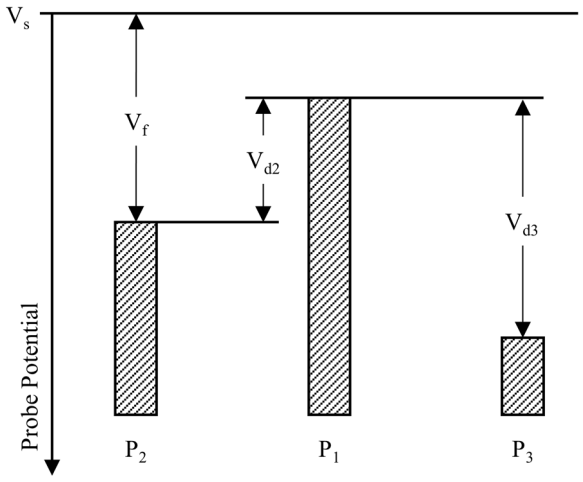

Figure 2.7: Diagram of the relative potential of each probe wire.

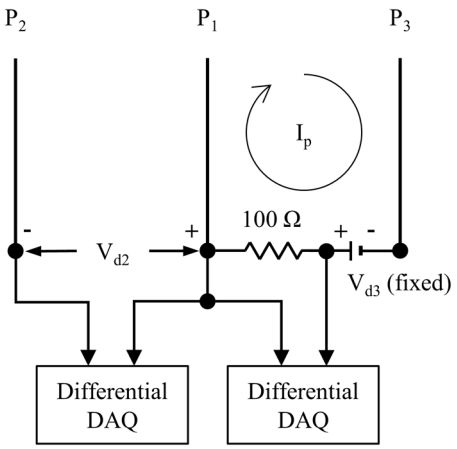

Figure 2.8: Triple probe circuit diagram constructed based on Chen's floating triple probe system.[50]

2.2.2 Design Considerations

When designing an electrostatic probe, ideally one wants to work in the thin sheath regime as it simplifies many aspects of the probe theory. However, often this is not possible in low-density discharges where the characteristic lengths of the discharge become too large to design a probe for the thin sheath regime. Under these conditions, it is preferable to design the probe for operation in the thick sheath regime where the characteristic lengths of the discharge are much larger than the radius of the probe; a thorough discussion of sheath formation and the different sheath regimes is provided in Sect. 3.1. Low electron densities were expected (on the order of 10^{14} to 10^{16} m^{-3}) in the AFRL's experimental setup based on preliminary measurements made by Hoff *et al*., so the initial approach was to design a probe for such conditions.[2] However, a correction factor was required to account for the orbital motion of ions in thick sheaths; without correction, the triple probe measurements could overestimate the plasma parameter by up to 60%.[50]

To the author's knowledge at the time the probe was designed and tested, the correction factor could only be obtained experimentally from the current-voltage characteristic curve obtained from single Langmuir probe measurements.[50] As discussed in Sect. 1.2, this approach was not feasible, so the triple probe was instead designed for operating in the upper end of the

expected electron temperature and density, where thin sheath approximations could be made with a reasonably sized probe. The maximum diameter that the probe wires could be before significantly perturbing the microwave beam was determined through simulations of the microwave beam conducted by Reid; 1 mm diameter wires were used based on the simulation results.[53] A theoretical method for correcting triple probe measurements outside the thin sheath regime was later found in literature; probe measurements presented in this dissertation work were corrected using this theoretical method, which is discussed in Sect. 3.1.3.[54]

Given that triple probe measurements can be corrected using a theoretical correction factor, the optimal wire diameter for the plasma conditions in the AFRL's experimental setup would be one that allows the probe to operate in the upper limit of the thick sheath regime – this limit is discussed in Sec. 3.1.3. When sizing the probe wires for operation in the thick sheath regime, one must keep in mind the electrical and mechanical challenges that come with working with thin tungsten wires. For example, electrical connections between the tungsten wire and the conductor (typically copper) carrying the signal to the DAQ become increasingly difficult to make without specialized hardware the thinner the wire gets. Electrostatic probes are one of the most common types of plasma diagnostics because they are inexpensive to make, so keeping electrical connections simple is an excellent way to judge how small is too small; for this work, the center pins of coaxial connectors were crimped to the probe wires.

2.3 Plasma Spectroscopy System

Plasma spectroscopy is a non-invasive diagnostic method that provides insight into plasma parameters (electron and gas temperatures) and processes based on the intensities and wavelengths at which light is emitted. Emission spectra are observed when energy is emitted in the form of photons as a result of particle interactions within the plasma, such as electron impact excitation.

In this investigation, optical emission spectroscopy was used to determine the electron and gas temperatures of the discharges.

2.3.1 Hardware Setup

Collection optics mounted on the linear translation stage located inside the vacuum chamber collected light emitted from the discharges generated at the focus of the microwave beam. The collection optics consisted of a mirror that redirected light from the plasma into an aspheric lens. The aspheric lens reduces optical aberrations, such as spherical aberrations, which can distort the light passing through it, causing a loss in the resolution of the image. The lens focused the light from the plasma into an optical fiber cable used to transmit the photons out of the chamber and into the entrance slit of a Princeton Instruments SpectraPro HRS-500 spectrometer. An optical fiber vacuum feedthrough served as the interface between the optical fiber inside the chamber and the one outside connected to the spectrometer. A diagram of the collection optics setup is shown in Fig. 2.9.

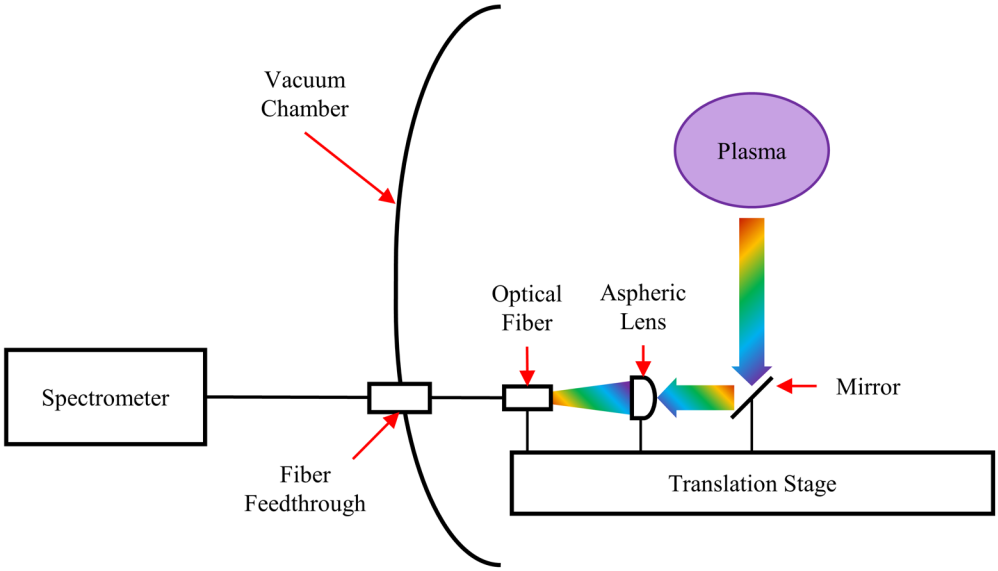

Figure 2.9: Optical emission spectroscopy setup used in this investigation.

The grating used for this investigation has a groove density of 1200 grooves/mm and a blaze wavelength of 500 nm, which is optimum for photons emitted in the 325 nm to 1000 nm wavelength range. Light reflected by the grating is refocused by a mirror into a PI-MAX4 intensified CCD (ICCD), which has a quantum efficiency ranging between 20% and 30% when collecting light emitted in the 480 nm to 850 nm wavelength range. Signals from photons detected by the ICCD are then sent to a computer where they are processed using LightField, a software developed by Princeton Instruments. The resulting image has a CCD resolution of approximately 0.05 nm (varies with wavelength) due to a combination of the 500 mm focal length of the spectrometer, the high groove density of the grating, and the 10 μm slit width. Furthermore, the ICCD has a thermoelectric cooler that reduces the CCD dark current to low levels (less than 2 electrons/second), which helps improve the signal to noise ratio. A diagram of the spectrometer and ICCD setup is shown in Fig. 2.10.

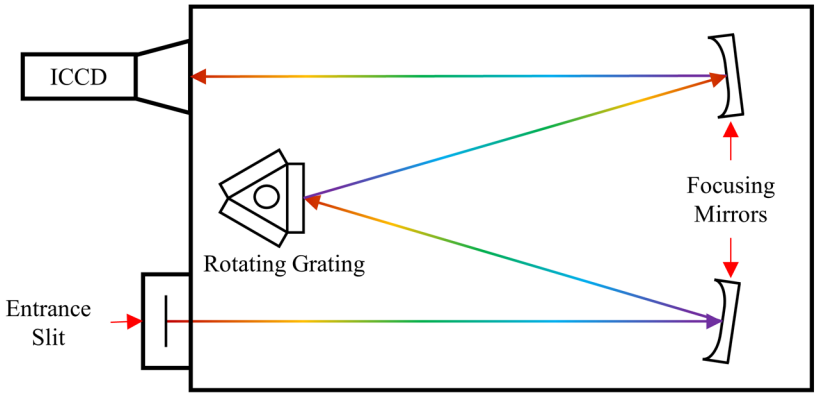

Figure 2.10: Diagram of the 0.5 m spectrometer and ICCD system setup used for optical emission spectroscopy measurements.

2.3.2 Calibration

The plasma spectroscopy system must be calibrated before being used to infer plasma conditions. Absolute wavelength and relative intensity calibrations were made in this work. The first step in calibrating the diagnostic system is determining the wavelength range in the electromagnetic spectrum that is of interest for the study. In this case, most of the photons emitted

by the plasma are in the visible and NIR regions of the spectrum, so the spectroscopy system was calibrated for spectral measurements in the 690 nm to 860 nm wavelength range. The region of interest in this work expands over a spectral range of 170 nm, which means the grating must rotate (change incident angles) five times to cover the entire wavelength range; the spectral range per frame captured by the ICCD is approximately 40 nm for the experimental setup.[2] Each time the grating rotates the centered wavelength changes, so the wavelength must be calibrated in the system to ensure the grating is at the correct angle; note that the resolution also changes due to its dependency to wavelength.

Most commercial spectrometers are supplied with some sort of wavelength calibration system that consists of a light source with well-documented emission lines. The spectrometer uses a spectral calibration system called IntelliCal that automates most of the calibration process when used with LightField. The IntelliCal system includes an atomic emission source with dual mercury and neon-argon lamps that cover the near ultraviolet to NIR regions of the electromagnetic spectrum. The neon-argon source was used for wavelength calibration of the spectroscopy system.

The spectra measured by a spectroscopy system are the convolution of the instrument response function and the input light. This dependence of the spectra on the instrument response makes it difficult to obtain reproducible accurate spectra when a component, such as the diffraction grating, changes in the system. The spectroscopy system can be calibrated against a known intensity reference to eliminate instrument dependencies from the measured spectra; note that instrumental broadening still has to be accounted for in the analysis of spectra. The IntelliCal system comes with a NIST traceable light source that automates the intensity calibration process

[2] The spectral range per frame captured by the ICCD can be increased at the cost of a decrease in the CCD resolution by using a diffraction grating with a lower groove density.

when used with LightField. Alternative intensity calibration methods are discussed by Kunze for those not using the IntelliCal system.[55]

Chapter III

Plasma Diagnostic Methods

3.1 Symmetrical Triple Langmuir Probe

The symmetrical triple Langmuir probe was first proposed by Yamamoto and Okuda in 1956 as a method for determining the EEDF in electrodeless and high-frequency discharges.[13] However, measurements of the EEDF were limited to the high energy tail end of the electron distribution as floating symmetrical probes operate outside the electron retarding region, which contains information on lower-energy electron population in the plasma. Furthermore, measurements of the EEDF using this triple probe method were time-consuming as the current going through the reference probe had to be adjusted to zero every time the potential between the double probe wires changed. Okuda and Yamamoto addressed the limitations on the energy range of the EEDF measurements in 1960 and Aisenberg proposed improvements to the time resolution of the measurements in 1964.[16], [49] However, these improvements were dependent on making the double probe wires asymmetrical, which introduced new challenges when working with electrodeless plasmas; for example, the large surface area of the reference probe would increase reflections of the electromagnetic waves in microwave discharges. In 1965, Chen and Sekiguchi proposed a symmetrical triple probe method capable of measuring the electron temperature and density instantaneously at the cost of information of the EEDF.[50] This method has since become the most common triple probe method employed when measuring the parameters of low-temperature plasmas and is one of the diagnostic methods used for this investigation.

3.1.1 Sheath Formation

Understanding how electrostatic probes work requires a basic understanding of the physics of sheaths. When a floating probe is immersed in a low-temperature plasma, the probe surfaces charge up negative relative to the plasma space potential (V_s) because electrons have much higher thermal velocities than ions allowing them to attach to the material surface at faster rates than ions. As a result of the negatively charged surface, a thin layer of positive ions surrounds the surface to balance its negative charge due to an effect called Debye shielding that helps the bulk plasma remain quasi-neutral. The length-scale of such shielding is known as the Debye length,

$$\lambda_D = \sqrt{\frac{\varepsilon_0 k_B T_e}{q_e^2 n_e}}, \tag{3.1}$$

where ε_0 is the permittivity of free space, k_B is the Boltzmann constant, T_e is the electron temperature, q_e is the elementary charge, and n_e is the electron density. As the probe potential, V_p, becomes more negative relative to the plasma space potential, fewer electrons have the energy to overcome the probe's repulsive force resulting in an exponential decrease of the electron density within the sheath. This behavior is described by the Boltzmann relation,

$$n_e(x) = n_{es} \exp\left(\frac{q_e \phi_s(x)}{k_B T_e}\right), \tag{3.2}$$

where n_{es} is the electron density at the outer edge of the sheath, *x* is the distance from the sheath's outer edge toward the probe, and $\phi_s(x)$ is the potential distribution within the sheath. The ion density, n_i, within the sheath also decreases even though ions experience an attractive force from the negatively biased probe. This behavior is due to the conservation of flux, which causes the density of ions in the sheath to decrease as the ions are accelerated through the potential drop within the sheath.

An exponential potential drop in the sheath region means that $n_i(x) > n_e(x)$ throughout the sheath according to Poisson's equation,

$$\frac{d^2\phi}{dx^2} = -\frac{q_e}{\varepsilon_0}[n_i(x) - n_e(x)]. \tag{3.3}$$

However, given that the ion density at the outer edge of the sheath, n_{is}, is approximately equal to n_{es} means that ions must enter the sheath with high enough velocity to satisfy the non-neutrality condition – this minimum limit is known as the Bohm velocity,

$$v_B = \sqrt{\frac{q_e T_e}{m_i}}, \tag{3.4}$$

where m_i is the mass of the ion. In a low-temperature plasma, the ion temperature, T_i, is much lower than the electron temperature, which means most ions have velocities lower than the Bohm velocity. Under these conditions, the sheath's electric field penetrates beyond the sheath's edge into the plasma to accelerate ions to their Bohm velocity – this region is known as the pre-sheath. The pre-sheath typically extends a distance on the order of the ion's mean free path with a potential drop (relative to V_s) defined by

$$V_{sh} = \frac{k_B T_e}{2q_e}, \tag{3.5}$$

as discussed by Allen *et al*.[56] A thorough review of the Bohm sheath criterion and the presheath is given by Riemann.[57] An illustration of the sheath and pre-sheath voltage potential profiles relative to the plasma space potential is shown in Fig. 3.1.

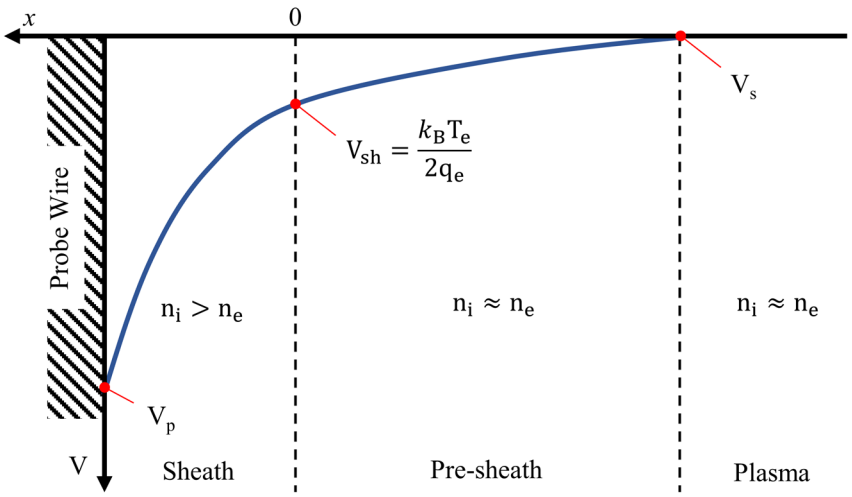

Figure 3.1: Diagram of a sheath and pre-sheath in contact with the surface of a probe wire. The vertical axis represents the voltage, V, relative to the plasma space potential. The horizontal axis represents distance, x, from the sheath's outer edge.

3.1.2 Probe Theory: Thin Sheath Approach

Triple probes collect ion and electron current through the sheaths that form around the probe wires; the sheath is considered thin when the radius of the probe (r_p) is much larger than the Debye length of the plasma. By measuring the current flowing through the biased probes and the potentials that exist between the probes one can calculate the electron temperature and density of the plasma. Analysis of the data recorded from the triple probe measurements require the following conditions to be valid.

1) The electron population in the plasma can be approximated by a Maxwellian distribution.
2) The mean free path of the electrons is much larger than the Debye length of the plasma and the radius of the probe wires.
3) The separation between the probe wires is larger than two times the thickness of the ion sheaths (including presheath) that surround the probe wires.

Assuming these conditions are met, the electron temperature can be calculated by

$$\frac{1-\exp\left(-\frac{q_e V_{d2}}{k_B T_e}\right)}{1-\exp\left(-\frac{q_e V_{d3}}{k_B T_e}\right)} = \frac{1}{2}, \tag{3.6}$$

as discussed by Chen and Sekiguchi.[50] When a relatively large voltage is applied between the biased probes, so that $q_e V_{d3} \gg k_B T_e$, the exponential component of the denominator goes to zero – this is mathematically represented by

$$\lim_{V_{d3}\to\infty} \exp\left(-\frac{q_e V_{d3}}{k_B T_e}\right) = 0. \tag{3.7}$$

Under this condition Eqn. 3.6 can be simplified to

$$T_e(\mathrm{eV}) = \frac{V_{d2}}{\ln 2}. \tag{3.8}$$

For the low-temperature plasmas generated in the AFRL's experimental setup, the 36 V from the four 9 V batteries connected in series was enough to make this approximation as the average electron temperature is just a few eV; this was also verified by solving Eqn. 3.6 numerically.

When the radius of the probe is much larger than the thickness of the ion sheath (a few Debye length thick), one can approximate the ion current density collected by the probe, J_i, to be equal to the ion current density at the outer edge of the sheath, J_{is}. Under this condition instantaneous values of the ion current density can be calculated by

$$J_i = \frac{I_p}{S_p\left[1-\exp\left(-\frac{q_e V_{d3}}{k_B T_e}+\frac{q_e V_{d2}}{k_B T_e}\right)\right]}, \tag{3.9}$$

where S_p is the surface area of the probe wires, and I_p is the current flowing through the externally biased probes. Using Eqn. 3.6 the denominator of Eqn. 3.9 can be simplified to

$$J_i = \frac{I_p}{S_p\left[\exp\left(\frac{q_e V_{d2}}{k_B T_e}\right)-1\right]}. \tag{3.10}$$

The Boltzmann relation and the conservation of flux equation can then be used to relate the ion current density to the electron density. Given that $n_{is} \approx n_{es}$ and $J_i \approx J_{is}$, the electron density can be calculated by

$$n_e = \frac{I_p \exp\left(\frac{1}{2}\right)\sqrt{m_i}}{S_p\left[\exp\left(\frac{q_e V_{d2}}{k_B T_e}\right) - 1\right] q_e \sqrt{k_B T_e}} . \tag{3.11}$$

In multispecies discharges, m_i can be approximated by the reduced mass of the atoms and molecules.[50], [54]

3.1.3 Probe Theory: Transitional and Thick Sheath Approach

There is a 10 to 20 percent error in electrostatic probe measurements due to the many assumptions (e.g., a Maxwellian EEDF) and approximations (e.g., the ion current) that are made during analysis.[20] As the sheath begins to deviate from the thin sheath condition (when $r_p \lesssim 100\lambda_D$), this error can increase by another 40% in triple probes according to Chen.[50], [54] The increase in error is attributed to differences in the ion current density collected by the probe wires. As a probe wire becomes more negative relative to the plasma potential, the ion sheath increases in size; thus, the current collection surface area also increases. The difference between the surface area of the ion sheath and the surface area of the probe wire can typically be ignored when $r_p \gg \lambda_D$, but when this condition is not met, the approximation $J_i \approx J_{is}$ can no longer be made and a correction factor must be introduced to reduce the error of the measurements.

There are two ways of estimating the correction factor: experimentally and numerically. The numerical approximation of the correction factor was used in this work, as discussed in Sec. 2.2.1. The dimensionless correction factor, η, introduced by Chen is dependent on the probe radius to Debye length ratio, ξ_e.[54] When $\xi_e \gg 1$, the effects of orbital motion are negligible so it can be assumed that all the ions that enter the sheath are collected by the probe; the sheath is known

as a transitional sheath when $1 \ll \xi_e \lesssim 100$. Under this assumption, the current reaching the sheath's edge, I_s, must be equal to the current reaching the probe, I_p. For cylindrical probes,

$$I_s = 0.61 S_p n_e q_e \xi_s \sqrt{\frac{k_B T_e}{m_i}}\,, \tag{3.12}$$

where ξ_s is the ratio of the radius of the sheath to the radius of the probe.[54] The current reaching the probe is space-charge-limited and can be expressed by the Child-Langmuir's equation,

$$I_p = \frac{2 L_p \left(V_p - V_{sh}\right)^{3/2}}{9 r_p F^2} \sqrt{\frac{2q_e}{m_i}}\,, \tag{3.13}$$

where L_p is the length of the probe, and F is a function of ξ_s; $F(\xi_s)$ was interpolated from tables of values provided by Langmuir.[54], [58] Normalizing the probe potential to the electron temperature, *y*, and letting $I_s = I_p$ results in

$$\left(y - \frac{1}{2}\right)^{3/2} = 0.97 \xi_e^2 F^2 \xi_s\,, \tag{3.14}$$

which relates the radius of the sheath to the probe potential through dimensionless parameters.[54]

The theoretical correction factor can be estimated by the gradient of the curve of ξ_s^2 as a function of *y* near the plasma floating potential normalized to the electron temperature, y_f. The normalized plasma floating potential is given by

$$y_f = \ln\left(\frac{0.65}{\xi_{sf}} \sqrt{\frac{m_i}{m_e}}\right), \tag{3.15}$$

where ξ_{sf} is the ratio of the radius of the sheath to the radius of the probe when the probe is at the plasma floating potential.[54] Using the gradient between $y_f - \frac{1}{2}$ and $y_f + \frac{1}{2}$, the correction factor can be estimated by

$$\eta(\xi_e) = \frac{\xi^2_{f+\frac{1}{2}} - \xi^2_{f-\frac{1}{2}}}{\xi^2_{sf}}, \tag{3.16}$$

where $\xi^2_{f-1/2}$ and $\xi^2_{f+1/2}$ are the values of ξ^2_s at $y_f - \frac{1}{2}$ and $y_f + \frac{1}{2}$, respectively.[54] It is important to note that the value of ξ^2_{sf} used in Eqn. 3.16 depends on ξ_e and can only be determined numerically. This means that for a given gas composition and ξ_e the values of y_f and ξ^2_{sf} can be approximated from the intersection of the curves of $\xi^2_s(y)$ and $\xi^2_{sf}(y_f)$ obtained from Eqns. 3.14 and 3.15, respectively; an example of these intersecting points for an Ar-N_2 (96% Ar, 4% N_2) plasma is shown in Fig. 3.2. Once y_f is determined, we can solve Eqn. 3.14 at the gradient boundaries to determine $\xi^2_{f-1/2}$ and $\xi^2_{f+1/2}$, and finally, calculate the theoretical value of η for a given ξ_e.

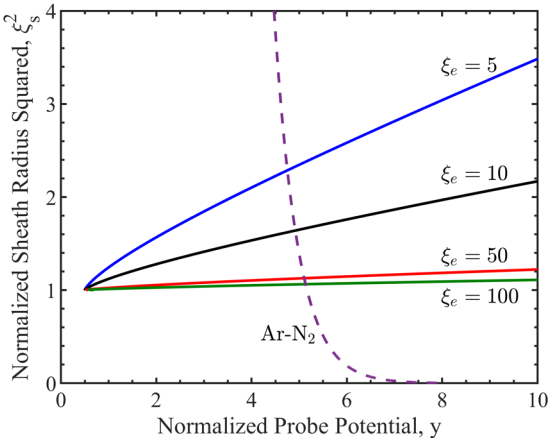

Figure 3.2: Theoretical curves (solid lines) of the square of the normalized sheath radius, ξ_s^2, as a function of the normalized probe potential under various ξ_e; these curves are obtained from Eqn. 3.14. The ξ_s^2 curve (dashed line) for Ar-N_2 (4% N_2) is obtained from Eqn. 3.15. The values of y_f and ξ_{sf}^2 for a given ξ_e are determined by the intersection of the curves.

When $\xi_e \lesssim 1$, the sheath is considered thick and all current collected by the probe is orbital motion limited. The current reaching the probe under this condition is given by Langmuir's orbital-motion theory as

$$I_i(V) = \frac{2}{\sqrt{\pi}} I_s(V_{sh})(1 + 2y)^{1/2}, \tag{3.17}$$

where $I_s(V_{sh})$ is the ion current collected at the sheath's outer edge, which can be obtained from Eqn. 3.12 when $\xi_s = 1$.[54] Theoretical values of η can be calculated in a similar way as for the $\xi_e \gg 1$ condition. The main difference is that η is now solely dependent on the gas composition of the plasma. The relation between η and the normalized plasma floating potential is given by

$$\eta = \frac{1}{2y_f}. \tag{3.18}$$

It is important to note that the relation for y_f will be different from the one defined by Eqn. 3.15 given that the current reaching the probe is governed by the orbital motion limited theory when $\xi_e \lesssim 1$. Taking Eqn. 3.17 into consideration, y_f can be derived in a similar way as Eqn. 3.15 resulting in the relation

$$y_f = \ln\left(\frac{0.73}{{y_f}^{1/2}}\sqrt{\frac{m_i}{m_e}}\right). \tag{3.19}$$

An exact solution for y_f can be obtained by

$$y_f = \frac{W(2A_0^2)}{2}, \tag{3.20}$$

where $A_0 \equiv 0.73\sqrt{m_i/m_e}$ and $W(2A_0^2)$ is the Lambert W-function. The theoretical value of η can then be calculated by plugging Eqn. 3.20 into Eqn. 3.18; this value is constant at a fixed gas composition when $\xi_e \lesssim 1$. From Chen's paper, it is not clear what the exact value of ξ_e is at which one needs to switch from Eqn. 3.16 to Eqn. 3.18 for calculations of the correction factor, so to determine this transition point the value of ξ_e at which Eqn. 3.16 and Eqn. 3.18 yield the same value of η was calculated.[54] An example of a typical $\eta(\xi_e)$ profile for an Ar-N_2 plasma is shown in Fig. 3.3.

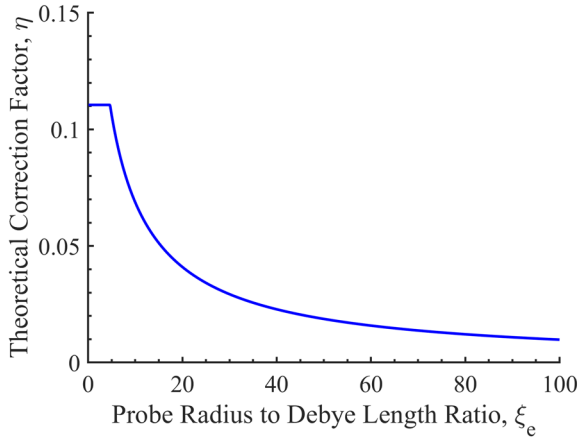

Figure 3.3: Theoretical correction factor, η, as a function of the ratio of the probe radius to the Debye length, ξ_e, for an Ar-N_2 (96% Ar, 4% N_2) plasma.

Calculating the theoretical correction factor can get complicated when working with inhomogeneous plasma as the probe can encounter different sheath conditions when making spatially resolved measurements. Furthermore, it is impossible to manually employ the intersection method discussed by Chen when making corrections to the millions of data points collected per plasma condition.[54] A MATLAB script was written to process the large amounts of data collected by the triple probe system to address this issue. Within the script, a function that calculates the theoretical correction factor for any gas composition and ξ_e combination was added; a copy of this function is provided in Appendix A.

Unfortunately, applying the correction factor to Eqn. 3.6 makes the equation impossible to solve analytically, so the electron temperature must be calculated numerically, which significantly increases the computational time of the MATLAB script. The corrected electron temperature is given by

$$\frac{1 - C(\eta, y_2, y_3)\exp(-y_2)}{1 - \exp(-y_3)} = \frac{1}{2}, \tag{3.21}$$

where

$$C(\eta, y_2, y_3) = \frac{1}{2}\left[(1-\eta y_2)^{1/2} + \sqrt{1+\eta(y_3-y_2)}\right], \tag{3.22}$$

$$y_2 = \frac{q_e V_{d2}}{k_B T_e}, \tag{3.23}$$

and

$$y_3 = \frac{q_e V_{d3}}{k_B T_e}, \tag{3.24}$$

as discussed by Chen.[54] Introducing the theoretical correction factor to Eqn. 3.11 makes the equation difficult to solve analytically, but not impossible. The corrected electron density is given with dimensionless parameters as

$$n_e = \frac{I_p \exp\left(\frac{1}{2}\right)\sqrt{m_i}\left[1-\eta\left(y_f-\frac{1}{2}\right)\right]^{1/2}}{S_p[\exp(y_2)-(1-\eta y_2)^{1/2}]q_e\sqrt{k_B T_e}}, \tag{3.25}$$

where y_f is calculated from

$$\exp(y_f) = 0.657\sqrt{\frac{m_i}{m_e}}\left[1-\eta\left(y_f-\frac{1}{2}\right)\right]^{1/2}, \tag{3.26}$$

as discussed by Chen.[54] Eqn. 3.26 is what makes the electron density difficult to solve analytically, but with the help of the Lambert W-function an exact solution for y_f can be calculated by

$$y_f = \frac{2+\eta-\eta W\left[2A_1^{-2}\eta^{-1}\exp\left(\frac{2}{\eta}+1\right)\right]}{2\eta}, \tag{3.27}$$

where $A_1 \equiv 0.657\sqrt{m_i/m_e}$ and $W\left[2A_1^{-2}\eta^{-1}\exp\left(\frac{2}{\eta}+1\right)\right]$ is the Lambert W-function of variable $2A_1^{-2}\eta^{-1}\exp\left(\frac{2}{\eta}+1\right)$. It is important to note that the corrections discussed in this section only help eliminate the error associated to operating outside the thin sheath conditions; this means that

after corrections, the measurements still have the 10 to 20 percent error inherent to electrostatic probes.[20], [50], [54]

3.2 Optical Emission Spectroscopy

Spectroscopy is a well-established diagnostic method that has been used for over two centuries. During its infancy, spectroscopy was mainly used to determine the wavelength of spectral lines produced by light sources such as the sun, and it was not until 1860 that a link between spectral lines and atoms was made by Kirchhoff and Bunsen.[59] In 1913, Bohr established a relation between spectra and the structure of the atom using Rutherford's atomic model to develop the theory of the hydrogen atom. However, the Rutherford-Bohr model became obsolete (does not produce accurate results for multi-electron systems) with the introduction of quantum mechanics and the discovery of quantum properties of subatomic particles, such as the electron spin. In 1964, Griem published the first monograph on plasma spectroscopy, which was followed by a review by Cooper and an introductory text by Marr.[60]–[63] Over the last five decades, many models have been developed to study the plasma parameters from spectral measurements. In this investigation, models developed by Simek and Biloui *et al.* were used to measure the gas temperature.[64]–[66] In addition, an argon-based collisional radiative model (CRM) based on a CRM for use in xenon plasmas developed by Dressel *et al.* to determine the electron temperature of the plasma is under development.[67] The physics necessary to understand these models will be discussed in this section.

3.2.1 Atomic Structure and Notation

Describing the structure of an atom involves treating electrons as particles that exhibit wave-like behavior (first proposed by Louis de Broglie). The shape of the wave that describes an electron system is known as the wave function, ψ, and its mathematical description is given by the

Schrödinger equation. Electrons within an atom can be modeled by the time-independent Schrödinger's equation,

$$\left[\frac{-\hbar^2}{2m}\frac{\partial^2}{\partial x^2} + V(x)\right]\psi(x) = \mathrm{E}_e\psi(x)\,, \tag{3.28}$$

where $\hbar$ is the reduced Planck constant, V(x) is the potential experienced by the electron, $\psi(x)$ is the time-independent wave function, and E_e is the energy of the electron. Solving the Schrödinger equation yields multiple wave functions as solutions, each solution corresponding to an allowed state. While interpretations of the meaning of the wave functions are still being debated within the scientific community, most agree that the probability of finding an electron in a specific volume of space within the atom can be described by the square of the wave function, $|\psi|^2$. This means that electrons can only exist in regions where $|\psi|^2 > 0$; note that regions where constructive interference occur indicate the regions where the electron is more likely to be found. The exact location of an electron cannot be determined for a given state due to the Heisenberg uncertainty principle, so a region in which the electron can be found 95% of the time can be defined from solutions to the Schrödinger's equation; these regions are known as atomic orbitals or sub-shells.

Visualizing atomic orbitals requires the introduction of four discrete numbers (called quantum numbers): the principal quantum number, the angular momentum quantum number, the magnetic quantum number, and the spin quantum number. The principal quantum number, n, indicates the main energy level or shell of the electron with an integer (n = 1, 2, 3, …). As the principal quantum number increases in value, the lower the average binding energy of the electrons in the shell. The angular momentum quantum number, l, provides information about the shape of the atomic orbital and is represented by an integer dependent on the principal quantum number (l = 0, 1, …, n-1); these integers are usually represented by the letters s, p, d, f, and g for l = 0, 1, 2, 3, and 4, respectively. For example, the s orbital (l = 0) is spherical, while the p orbital (l = 1)

is dumbbell-shaped; a diagram of the s and p orbitals is shown in Fig. 3.4. The magnetic quantum number, m_l, describe the orientation (azimuthal component) of the orbital and is represented by an integer value dependent on the angular momentum quantum number (m_l = -l, …, l). This means each atomic orbital can exist in more than one orientation (except the s orbital since it is spherically symmetrical) relative to the nucleus. The spin quantum number, m_s, indicates the magnetic state of the electron, which is represented by a half-integer ($m_s = \pm 1/2$). This means that each atomic orbital is limited to two electrons since the Pauli exclusion principle limits one electron per quantum state.

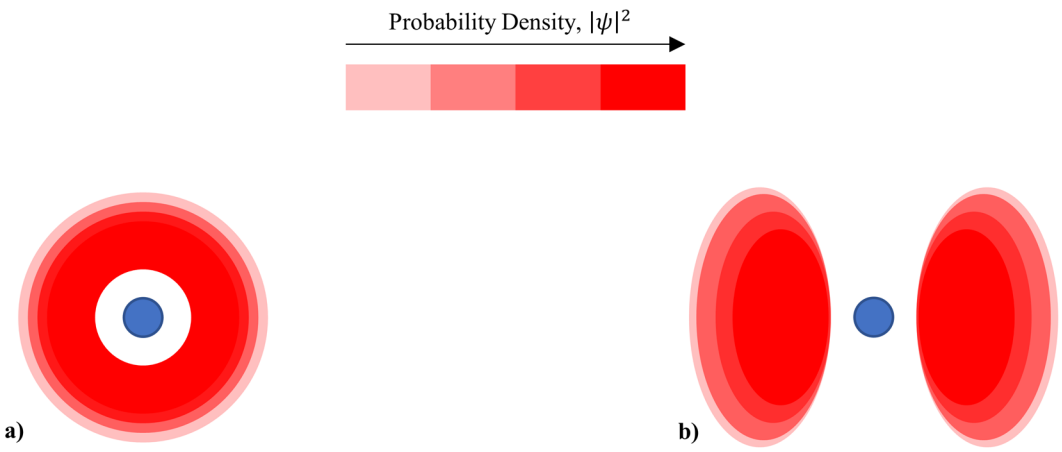

Figure 3.4: Diagram of the **a)** s orbital and **b)** p orbital. The nucleus of the atom is represented by the blue circle and the probability density, $|\psi|^2$, is represented by the shaded red regions. Note that the s orbital in three-dimensional space would be represented by a sphere enclosing the nucleus.

In the absence of external influences, individual states are populated with electrons so as to minimize the total energy of the electrons. This means electrons must first fill the lowest energy level available before moving to a higher one as described by the Aufbau principle. Electrons in the outermost shell first seek empty orbitals (to minimize repulsion) before pairing up with an electron of opposite spin as described by Hund's rules. This natural arrangement of electrons within the atom is referred to as the ground state configuration and can be represented by the principal and angular momentum quantum numbers of each subshell (nl). For example, the

electron configuration of a nitrogen atom in its ground state is $1s^2 2s^2 2p^3$, where the superscript indicates the number of electrons in the subshell; the number of electrons in a subshell is limited to $2(2l+1)$. While this notation is usually used to describe the ground state configuration of an atom, it can also be used to describe excited states.

The electron configuration of light atoms ($Z \lesssim 40$) is usually extended to include the values of the allowed total orbital and spin angular momentum quantum numbers, L and S, respectively.[68] The L and S quantum numbers are obtained from the sum of the l and m_s values of all valence electrons, respectively. The nomenclature for the total angular momentum quantum number is L = 0, 1, 2, 3, 4, … = S, P, D, F, G, …, which is analogous to that of l. The notation for the extended part of the electron configuration containing information of the L and S quantum numbers is called the LS term and is given by $^{(2S+1)}\mathrm{L}$. One can further expand the LS term to include the total angular momentum quantum number, J, which is the sum of the total orbital and spin angular momentum (J = L + S). This scheme of adding the total orbital and spin angular momentum to obtain the total angular momentum is called LS-coupling or Russell-Saunders coupling and its described by the term symbol $^{(2S+1)}\mathrm{L_J}$. An argon atom in its ground state can be described by the Russell-Saunders notation as $1s^2 2s^2 2p^6 3s^2 3p^6 (^1S_0)$.

Often the term symbol includes a term on the upper right-hand side that describes the parity, P, of the state. The term symbol that includes the parity of the state is of the form $^{(2S+1)}\mathrm{L_J^P}$, where P is written as "o" if the parity is odd and omitted if it is even. All wave functions describing the stationary states of an atom have definite parity, where the parity is even if $\psi(x) = \psi(-x)$ and odd if $\psi(-x) = -\psi(x)$. The parity can also be determined from the electron configuration by adding the l value of each electron (j) in the atom as described by

$$\mathrm{P} = (-1)^{\sum_j l_j}. \tag{3.29}$$

The parity is even when P = 1 and odd when P = -1. Note that only odd orbitals (l = 1, 3, …) contribute to the total parity as the sum of even orbitals will always result in even integers. Furthermore, all filled orbitals result in even integers after summation, so it is reasonable to perform the summation only over the electrons in unfilled odd orbitals.

3.2.2 Atomic Processes

When two particles collide, the collision can be described as elastic or inelastic with elastic collisions being the most common type of collision in low-temperature plasmas. While elastic collisions contribute to the kinetic energy of atoms (or ions)[3], the interactions do not result in the emission of photons (no change in atom's internal energy), which are essential for optical emission spectroscopy. For this reason, the focus of this section will be on inelastic collisions which are responsible for most of the atomic processes that take place in our plasma. Atomic processes that occur as a result of inelastic collisions can be separated into two categories: bound-bound and bound-free processes.

Bound-bound processes occur when a collision results in a bound electron transitioning between bound states, such in electron impact excitation and de-excitation. In electron impact excitation, a free electron transfers some of its energy to a bound electron of an atom during the collision causing the bound electron to transition to a higher energy state. This process can be represented by

$$\mathrm{M}^{\mathrm{Y}} + \mathrm{e}^{-*} \longrightarrow \mathrm{M}^{\mathrm{Y}*} + \mathrm{e}^{-}, \tag{3.30}$$

where e^- represents a free electron, M represents an atom, Y is the charge state of the atom, and the * symbol indicates that the atom or electron has extra energy. For example, a ground-state nitrogen atom getting excited to one of its first resonance states can be represented by

[3] In this section, assume the atomic processes described for atoms also apply to ions.

$$N + e^{-*} \longrightarrow N^{*} + e^{-}, \tag{3.31}$$

or as

$$1s^2 2s^2 2p^3\left({}^4S^o_{3/2}\right) + e(\varepsilon_i) \longrightarrow 1s^2 2s 2p^3 3s\left({}^4P^o_{1/2}\right) + e(\varepsilon_j), \tag{3.32}$$

to include the transition information, where ε_i and ε_j are the initial and final energy of the free electron, respectively – a diagram of this atomic process is shown in Fig. 3.5. Note that the difference between ε_i and ε_j represent the kinetic energy the free electron lost during the collision, and the potential energy gained by the bound electron since total energy is conserved the collision.

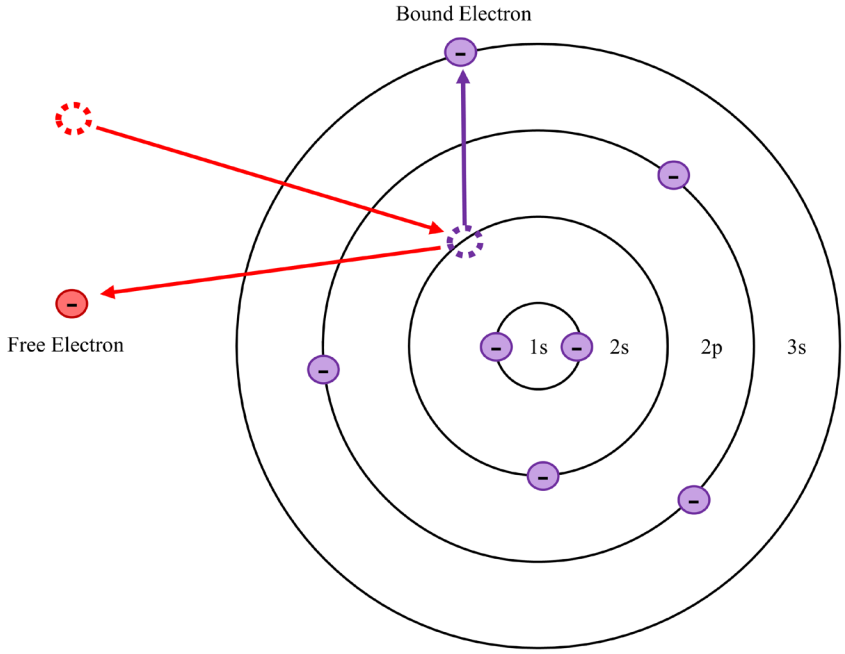

Figure 3.5: Electron impact excitation of a ground-state nitrogen atom. The red lines represent the free electron colliding with a bound electron originally in the 2s subshell, while the purple line represents the bound electron transitioning to a higher energy level (3s subshell).

Atoms can also be excited by absorbing a photon; however, the energy of the photon must be equal to the energy needed for the transition for it to be absorbed. In photoexcitation, the electric and magnetic fields of the photon are responsible for the excitation of the bound electron with the strongest excitation coming from the electric field component. The reaction can be written as

$$M^Y + h\nu \longrightarrow M^{Y*}, \tag{3.33}$$

where h is Planck's constant, and ν is the photon's frequency. Without an external source of photons, the probability of an atom getting excited by a photon is low in optically thin plasmas. In low-temperature plasmas, the main source of photons are spontaneous transitions from excited and molecular states.

During a spontaneous emission, excess energy from a bound electron is released as a photon via electric dipole radiation. The energy of the photon is determined by the difference in energy between the initial and final bound states of the electron. The bound states an excited electron is most likely to transition to (known as allowed transitions) can be predicted by a set of selection rules. For a multi-electron atom, the selection rules impose the following conditions based on the quantum numbers[4] of the excited state:[69], [70]

- $\Delta J = 0, \pm 1$ ($J = 0 \leftrightarrow 0$ is a forbidden transition)
- $\Delta M_J = 0, \pm 1$
- Parity changes ($P = -1 \leftrightarrow 1$)
- When $\Delta S = 0$ in LS-coupling, $\Delta L = 0, \pm 1$ ($L = 0 \leftrightarrow 0$ is a forbidden transition)

When the selection rules are not met, the excited atom can still lower its total energy through forbidden transitions, such as electric quadrupole and magnetic dipole transitions; however, these occur at much lower rates than allowed transitions. Excited atoms in this state are said to be in a metastable state, which have relatively long lifetimes compared to excited atoms that can lose their energy through allowed transitions. For example, argon in the metastable state

[4] M_J is the magnetic angular momentum quantum number, which is related to the total angular momentum by the inequality $-J \leq M_J \leq J$. M_J only becomes relevant in the presence of external static magnetic field, $\vec{B}_{ext}$, capable of splitting the spectral lines due to the Zeeman effect. The Zeeman effect depends on the strength of the external field and only becomes significant outside the weak-field limit ($\vec{B}_{ext} \ll \vec{B}_{int}$), where $\vec{B}_{int}$ is the internal magnetic field of the atom.[70] M_J is introduced solely to provide a complete set of rules for allowed transitions in multi-electron atoms.

$1s^2 2s^2 2p^6 3s^2 3p^5 4s(^3P_0^o)$ has a lifetime of approximately 40 seconds, while its excited states that can decay through spontaneous emission have lifetimes on the order of 10^{-8} to 10^{-6} seconds.[71] The long lifetimes of the metastable states allow metastable atoms to contribute to the kinetics of other chemical reactions in the plasma and lose energy through collisional relaxation processes, such as electron impact de-excitation.

Electron impact de-excitation is an atomic process similar to electron impact excitation with the main difference being the direction in which energy is transferred between the particles as represented by the reaction

$$M^{Y*} + e^- \longrightarrow M^Y + e^{-*}. \tag{3.34}$$

In electron impact de-excitation, the excited bound electron decays into a lower energy level without emitting a photon by transferring its excess energy to the free electron during the collision. For electron impact de-excitation processes to be relevant in the depopulation of excited states, their reaction rates must be large enough to compete with those of spontaneous emission, which usually is not the case in low density plasmas. However, electron impact de-excitation reactions can play an important role in the depopulation of metastable states as the excited atom cannot quickly decay to a lower energy state via allowed transitions. This also means other atomic processes, such as electron impact excitation and ionization, can contribute to the depopulation of metastable states as the energy required to transition the bound electron to a higher energy state or even remove it from the atom is much less than when the atom is in its ground state.

Electron impact ionization is one of the many atomic processes that result in an electron moving between bound and free states. In electron impact ionization no photon is emitted as a result of the collision, but a bound electron is released from the atom in the process instead. This atomic process can be described by the reaction

$$M^{Y} + e^{-*} \longrightarrow M^{Y+1} + e^{-} + e^{-}. \quad (3.35)$$

For an atom to lose a bound electron during a collision with a free electron, the free electron must transfer enough energy to the bound electron to overcome its binding energy or ionization potential. In low-temperature plasmas, only a small percent of the electron population has enough energy to remove electrons from atoms in their ground state, which results in low ionization fractions. Atoms can also reach higher charge states through photoionization, but the probability of a photon removing an electron from an atom is low compared to electron impact ionization in optically thin plasmas when there is no external source of photons. The photoionization process can be described by the reaction

$$M^{Y} + h\nu \longrightarrow M^{Y+1} + e^{-}. \quad (3.36)$$

The reverse process of an atom losing an electron is an electron recombining with the atom. Three-body recombination is the reverse process of electron impact ionization where two free electrons collide in the vicinity of an ion resulting in one electron gaining energy and the other getting captured by the ion. This process is usually ignored at low electron densities because the probability of two free electrons colliding in the vicinity of an ion is very low; however, this process scales up with electron density and can become the dominant recombination mechanism at higher electron densities (over approximately 10^{16} cm^{-3}). Electrons can also recombine with atoms through radiative recombination, which is the inverse process of photoionization as described by the reaction

$$M^{Y+1} + e^{-} \longrightarrow M^{Y} + h\nu. \quad (3.37)$$

The free electron in the photoionization process can be captured into any of the bound states resulting in a photon of energy equivalent to the kinetic energy lost by the free electron which is dependent on the binding energy of energy level the electron gets trapped in. Unlike spontaneous

emission, the photon emitted in this process results in a continuous spectrum (known as radiative recombination continuum) because the initial energies of free electrons are not quantized. The transition rate of this process is usually only significant at very low temperatures (less than a few tenths of an eV), but there are cases where it can be the dominant process.

Dielectronic recombination is a two-step recombination process that begins with a free electron getting captured by an ion while transferring energy to a bound electron through a resonant process called dielectronic capture. The free electron can be captured into any of the available bound states, which increases the chances of the free electron having the right amount of energy for the process. The dielectronic capture process results in an unstable atomic state that can either re-emit the captured electron (a process known as autoionization) or radiatively decay into a lower energy state via the emission of a photon. The latter is known as dielectronic recombination and can be described by the two-step reaction

$$M^{Y+1} + e^{-} \leftrightarrow M^{Y**} \longrightarrow M^{Y} + h\nu. \tag{3.38}$$

Dielectronic recombination is typically the dominant recombination mechanism in laboratory plasmas even though it is a two-step process. A diagram of the dielectronic recombination two-step process is shown in Fig. 3.6.

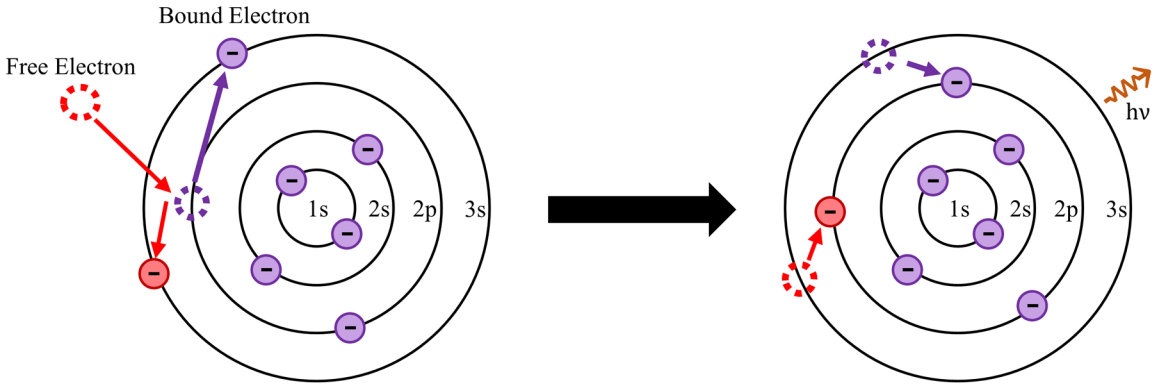

Figure 3.6: Dielectronic recombination process for a nitrogen ion. The first step illustrates the dielectronic capture of a free electron (red) by the ion. The second step in the process consists of the excited electrons decaying to lower energy levels and emitting a photon per transition taken.

One way to get some insight into the energy requirements of an atom's bound states is through an energy diagram. From an energy level diagram, one can get an idea of the approximate energy needed for electron transitions within the bound states of an atom and the energy required to completely remove an electron from the atom (ionization). An energy level diagram example of the argon atom is shown in Fig. 3.7. Note that the energy diagram in Fig. 3.7 is meant to only provide some insight on the relative energies of the bound states of an excited argon atom ($3p^5nl$ configuration); energy values can be found in the National Institute of Standards and Technology (NIST) data bank.[72] Furthermore, sometimes not all energy states can be illustrated accurately in a diagram as the energy of energy states within the same subshell sometimes only vary by a very small amount (hundredths of a volt). For example, the 4p subshell has ten possible energy states, but only six are illustrated in Fig. 3.7 since some states, such as the $^1P_1$(-2.477 V) and $^3P_0$(-2.487 V) states have similar potential energies.[68]

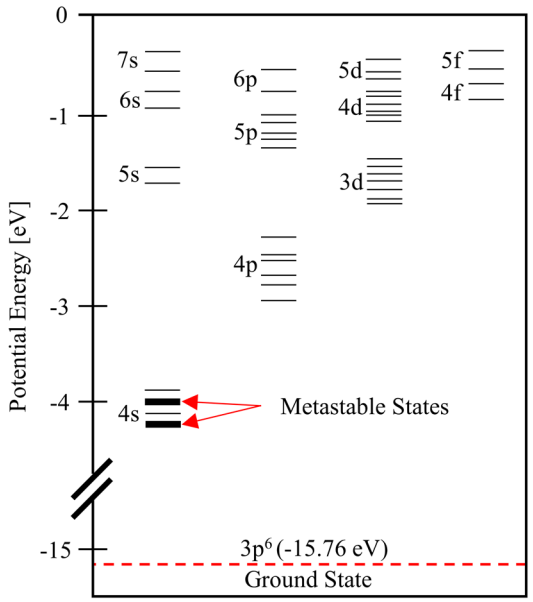

Figure 3.7: Energy level diagram for the $3p^5nl$ configuration of an argon atom.[68]

3.2.3 Molecular Spectra and Notation

Molecular processes are more complex than atomic processes as molecules have additional degrees of freedom (vibrational and rotational) to which free electrons can lose their energy. The focus of this section will on homonuclear diatomic molecules as the molecular spectra of excited N_2 is used to determine the temperature of the gas in our experiments. The spectroscopic term notation used to describe the state of diatomic molecules is similar to that of atoms where the total orbital angular momentum and total electron spin angular momentum quantum numbers are defined in the term symbol. The total orbital angular momentum of a diatomic molecule is defined along the internuclear axis and is denoted by Λ = 0, 1, 2, and 3, which correspond to Σ, Π, Δ, and Φ, respectively. The total electron spin angular momentum is represented by the quantum number S and appears in the multiplicity (2S+1) of the term symbol in the form ${}^{(2S+1)}\Lambda$. For diatomic molecules, the total angular momentum quantum number, Ω, is usually included as a subscript in the term symbol to describe electronic sub-states when $\Lambda \neq 0$.[69] Here the total angular momentum is the sum of the total orbital angular momentum and total electron spin angular momentum along the internuclear axis (denoted by the quantum number Σ). Note that the quantum number Σ is different from the Σ state defined by $\Lambda = 0$. Furthermore, the quantum number Σ is dependent on the total electron spin angular momentum ($-S \leq \Sigma \leq S$) and is only defined when $\Lambda \neq 0$.

The term symbol also includes information about the symmetry of the electronic wave function in the form of the superscripts and subscripts. In the superscript, "+" and "–" are used to indicate if the wave function is symmetric or antisymmetric with respect to any plane including the internuclear axis. The subscript is only included when describing homonuclear molecules, such as N_2, and it describes the wave functions symmetry with respect to the interchange of nuclei;

"g" is used if it is symmetric and "u" if antisymmetric.[71] Molecules in their ground state are identified by an X before the term symbol and by capital letters A, B, C, and so on to represent a series of excited states having the same multiplicity as the ground state. Lowercase letters a, b, c, and so on are used for excited states with different multiplicity than the ground state.[71]

Like excited atoms, molecules in excited states can also decay to lower energy states by emitting a photon via electric dipole transitions (allowed transitions). These too have a set of selection rules governed by the quantum numbers of the excited state:[68], [71]

- $\Delta\Lambda = 0, \pm 1$
- $\Delta S = 0$
- $\Sigma^+ \rightarrow \Sigma^+$ or $\Sigma^- \rightarrow \Sigma^-$ (in transitions between Σ states)
- $g \rightarrow u$ or $u \rightarrow g$ (in homonuclear molecules)

Allowed transitions for excited homonuclear diatomic molecules require a change in the electronic state, which means vibrational and rotational transitions within the same electronic state are not allowed by the selection rules (forbidden transitions). Consequently, homonuclear diatomic molecules do not produce a pure vibrational or rotational spectrum.

When an excited homonuclear diatomic molecule decays to a lower electronic state, photons are emitted over broad wavelength regions (known as spectral bands or rovibrational bands) as there are no restrictions to changes in the vibrational state during the electronic transition; the energy of the photon accounts for changes in the electronic, vibrational, and rotational states.[73] Molecular bands consist of many individual emission lines, resulting from changes in the vibrational, rotational, and electronic states of the molecules. These emission lines are usually too close together for the resolution of the average spectrometer to detect them as individual lines. Instead, the emission lines are observed as a merged continuous spectrum with a sharp drop in

intensity at one end and a gradual decrease in intensity towards the other end. The peak leading to the sharp drop in intensity is called the band head and is used to identify the spectral band within a band system. A band system consists of all the rovibrational bands associated with a specific electronic state transition. For example, bands produced from $B^3\Pi_g$ to $A^3\Sigma_u^+$ transitions in N_2 are part of the first positive system of nitrogen, where the name "first positive" refers to being the first excited state of a neutral molecule that can radiatively decay to a lower energy state; a band system is referred as "negative" if the molecule is not neutral.

Identifying the rovibrational bands in a band system requires knowledge of the energy levels within the molecule. The electronic energy of diatomic molecules can be described by the Morse potential, which is dependent on the distance between the two nuclei. Within the potential well of an electronic state, there is a series of vibrational levels. The energy of a vibrational level (E_υ) can be described by the harmonic oscillator model with the first anharmonic correction,

$$E_\upsilon = h\nu_e\left(\upsilon + \frac{1}{2}\right) - x_e h\nu_e\left(\upsilon + \frac{1}{2}\right)^2, \tag{3.39}$$

where ν_e is the natural vibrational frequency of the molecule, υ is the vibrational quantum number, and x_e is the first anharmonicity constant.[69], [73] The anharmonic correction causes the spacing between the vibration levels to decrease as their energy approaches the dissociation energy (D_e) of the molecule. Note that the actual energy required for dissociation of the molecule (D_0) is less than the dissociation energy since the ground state of a molecule has some internal energy from the lowest vibrational level. A diagram of the Morse potential curve is shown in Fig. 3.8.

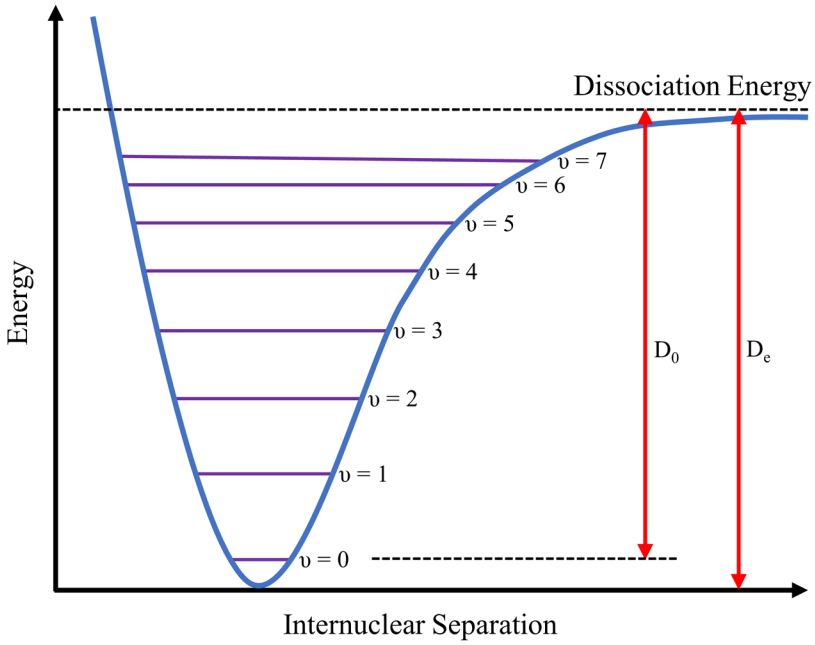

Figure 3.8: Morse potential diagram for diatomic molecules.

Rovibrational bands within a band system are identified by the change in the vibrational level during an allowed transition. Electronic transitions resulting in similar changes in the vibrational level ($\Delta\upsilon = \upsilon' - \upsilon''$) appear in the spectrum as a series of bands (called progressions) whose separation increases at a slow rate; note that the first prime ($'$) and second prime ($''$) denote the upper and lower electronic states, respectively.[73] Each band head within a progression represents a change in the υ' and υ'', but not in the $\Delta\upsilon$. When $\Delta\upsilon$ changes within a band system, a new progression forms in a different part of the spectrum determined by the wavelength of the emitted photons. This results in a band system extending over a wide range of wavelengths in the electromagnetic spectrum. For example, the first positive system of N_2 extends over the 478 nm to 2531 nm wavelength range.[74]

Vibrational levels have their own set of rotational levels, which are responsible for the wavelength range of rovibrational bands. The energy of the rotational levels can be obtained by solving the Schrödinger equation for a rigid rotor and adding a correction for centrifugal distortion. The resulting rotational energy (E_J) equation is given by

$$E_{\mathcal{J}} = \frac{h^2 \mathcal{J}(\mathcal{J}+1)}{8\pi^2 \mu r_e} - D_{\mathcal{J}} \mathcal{J}^2 (\mathcal{J}+1)^2, \tag{3.40}$$

where $\mathcal{J}$ is the rotational quantum number, μ is the reduced mass of the molecule, r_e is the internuclear distance, and $D_{\mathcal{J}}$ is the centrifugal distortion constant.[69], [73] When excited molecules radiatively decay to a lower energy state, the emission lines can be separated by branches based on the change in the rotational level: the P-branch ($\Delta\mathcal{J} = -1$), Q-branch ($\Delta\mathcal{J} = 0$), and R-branch ($\Delta\mathcal{J} = 1$) are the three most common branches. These branches can be used to identify the location of sub-band heads (peaks) within a rovibrational band; the turning point of a Fortrat parabola indicates the location of such peaks.[73] A diagram of the rotational levels within an electronic state is shown in Fig. 3.9. Note that the spacing between the rotational levels increases as their energy increases due to the centrifugal distortion.

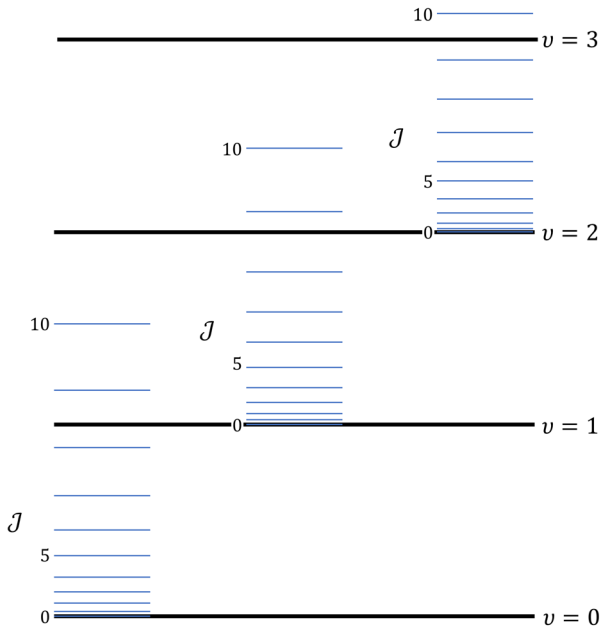

Figure 3.9: First few rotational and vibrational levels of an electronic state.[73]

3.2.4 Spectral Line and Band Identification

In plasma spectroscopy, it is important to identify which elements are present in the plasma as it can help detect the presence of contaminants and determine the spectral range of interest.

Argon is the main gas used in our experiments, so the plasma spectroscopy system was designed to collect photons emitted in the optical and NIR range by excited argon atoms. Some of the gas mixtures studied also included small amounts of nitrogen (up to 10% of the gas concentration), which allowed the gas temperature to be approximated from its rovibrational bands emitted in the optical range. Spectral measurements of plasma generated from various gas mixtures of argon, nitrogen, and oxygen were made in the 690 nm to 860 nm wavelength range for this investigation.[5] Spectral measurements confirmed the presence of eighteen strong excited argon emission lines (Ar I) in all experiments. In plasma containing nitrogen, the 2-0 band progression of the first positive system of nitrogen was observed. Also, two emission peaks, each containing three excited oxygen emission lines (O I), were observed in the measured spectral range when oxygen was added to the plasma. Sample spectral measurements of different gas mixtures are shown in Fig. 3.10-3.13.

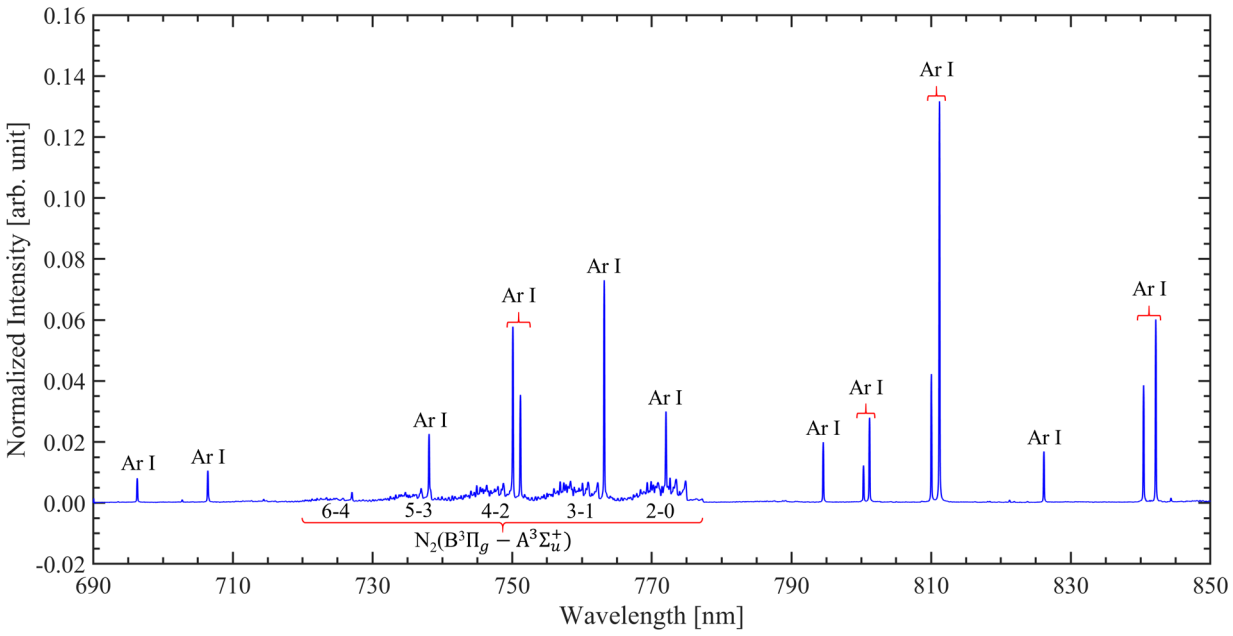

Figure 3.10: Spectrum of an Ar-N_2 (4% N_2) plasma generated at the focus of a 7.5 kW microwave beam at 200 mTorr.

[5] There is an Ar I emission line at 852.1 nm, but since it was not used in our collisional radiative model, only spectra between 690 nm and 850 nm was analyzed.

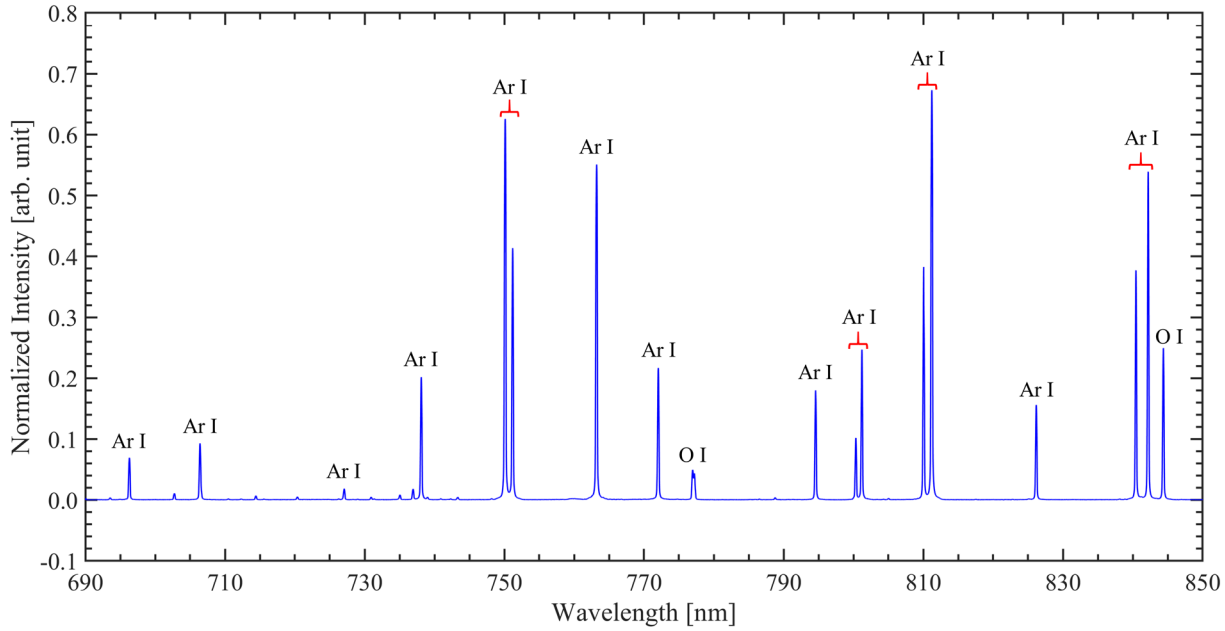

Figure 3.11: Spectrum of an Ar-O_2 (4% O_2) plasma generated at the focus of a 7.5 kW microwave beam at 200 mTorr.

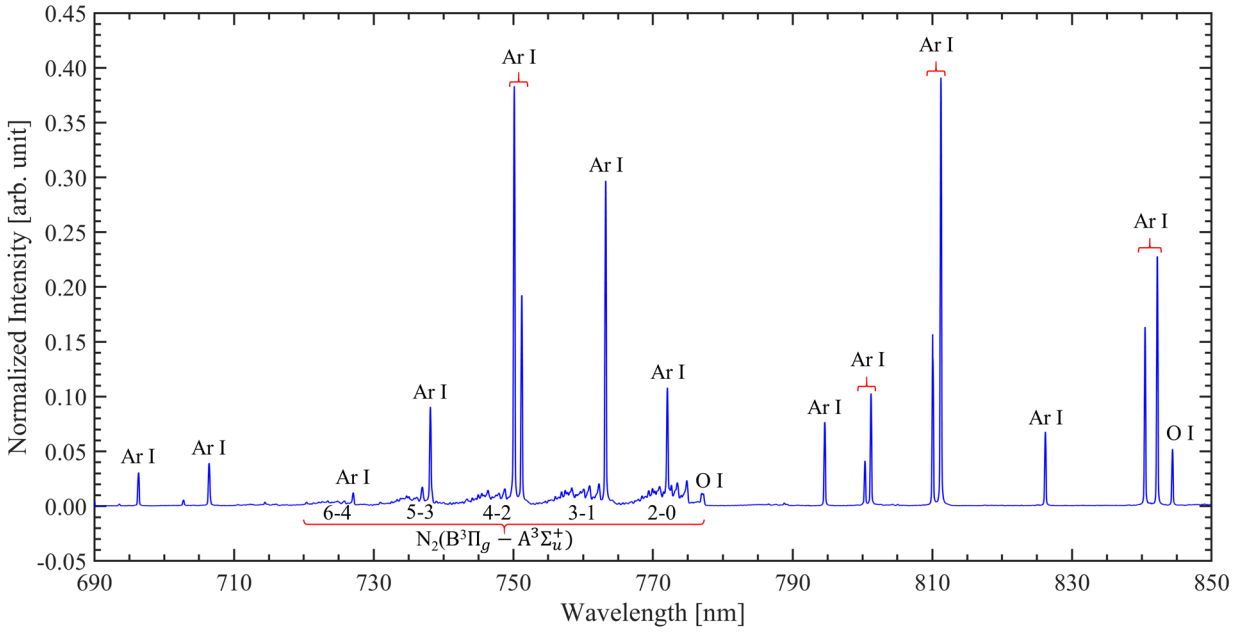

Figure 3.12: Spectrum of an Ar- N_2-O_2 (4% N_2, 4% O_2) plasma generated at the focus of a 7.5 kW microwave beam at 200 mTorr.

3.2.5 Spectral Line Broadening

The laws of quantum mechanics describe the atom as having discrete energy levels, so one would expect photons emitted from the decay of an excited atom into a lower energy state would all have the same energy for a given allowed transition. However, this is not the case because

according to the uncertainty relation there is an uncertainty in the energy measurement (ΔE) of a quantum state when also measuring its lifetime; this is described by the equation,

$$\Delta \mathrm{E}\Delta t \geq \frac{\hbar}{2}\ , \tag{3.41}$$

where Δt is the uncertainty in the lifetime measurement. This phenomenon is observed in the natural broadening of emission lines. Other broadening mechanisms include Doppler broadening, pressure broadening, Stark broadening, self-absorption broadening, and the Zeeman effect; however, most of these are only encountered under specific conditions or are not the dominant broadening mechanism in low electron density, low temperature plasmas.[55], [75] In addition to the condition-dependent broadening mechanisms, instrument broadening also must be taken into consideration when analyzing spectral measurements.

Line broadening affects intensity measurements as photons associated with a specific radiative decay transition are collected over a wider range of wavelengths, which means the intensity is not just the maximum value of the emission line as it would be if all photons had the same exact energy. This means photons collected in the nearby wavelengths (usually within a few angstroms of the center wavelength) must also be considered when calculating the intensity of the emission line. Broadened emission lines can typically be described by a Gaussian, Lorentzian, or Voigt profile, so often one of these profiles is fitted to the emission line for intensity calculations; the full width at half maximum (FWHM) of the fitted function is usually used to set the range over which to sum the intensities of the line shape. The FWHM of a Gaussian fit was used for intensity calculations in this investigation. An example of a Gaussian profile fitted to an Ar I emission line is shown in Fig. 3.13.

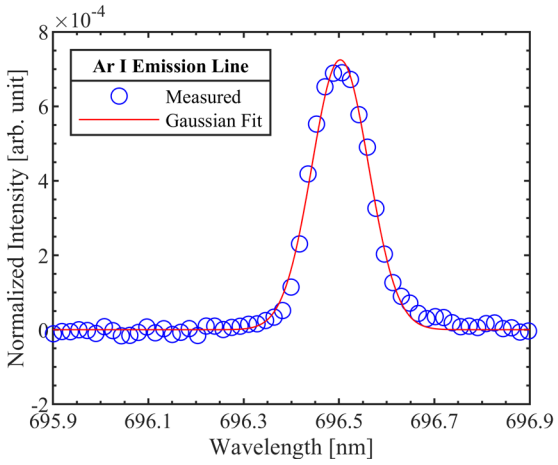

Figure 3.13: Gaussian profile fitted to Ar I emission line (696.5 nm). Data is from Ar-N_2 (4% N_2) plasma generated at the focus of a 7.5 kW microwave beam at 200 mTorr.

3.2.6 Gas Temperature: Biloiu's Model

There are various methods for approximating the neutral gas temperature (T_g) from the molecular spectra of nitrogen; depending on the plasma conditions, spectra from the first negative ($B^2\Sigma_u^+ \rightarrow X^2\Sigma_g^+$), first positive ($B^3\Pi_g \rightarrow A^3\Sigma_u^+$), or second positive ($C^3\Pi_u \rightarrow B^3\Pi_g$) systems are typically used in the models. The first negative and second positive systems have rovibrational bands in the 268 nm to 546 nm and 286 nm to 587 nm wavelength range, respectively; these ranges are outside the optimal spectral range of our spectroscopy system.[74] Furthermore, the excited states of these band systems have relatively short radiative lifetimes (approximately 40-60 ns) compared to the mean neutral collision time range (0.6-1.3 μs) anticipated when operating in the 100 mTorr to 200 mTorr background gas pressure (P_g) range. [74], [76] The mean gas-kinetic collision time of N_2 molecules is given by

$$\bar{t}_c = \frac{17.7\sqrt{T_g}}{P_g\left[1 + 2.14\exp\left(-6T_g \times 10^{-4}\right)\right]}, \tag{3.42}$$

where the collision time is in nanoseconds, the pressure in Torr, and the gas temperature in Kelvin (as cited by Biloiu).[66] When the lifetime of the radiative process is shorter than the rotation-translation relaxation time, it is unlikely that the rotational distributions achieve thermodynamic

equilibrium with the bulk gas.[77] For these reasons, it was determined that the first negative and second positive systems of nitrogen were not good systems for the operational conditions encountered in the AFRL's experimental setup.

The first positive system of nitrogen was used instead as the lifetime of the $N_2(B^3\Pi_u)$ state (approximately 4-14 μs for v' = 0-12) is longer than its mean collision time.[76], [78]–[83] Assuming that the $N_2(B^3\Pi_u)$ state's rotational distribution thermalizes within 2-3 collisions, the measured rotational temperature should be a good approximation of the translational temperature of the neutral gas.[66] Another advantage of using the first positive system is that the 2-0 rovibrational band is within the spectral range originally set for measurements of the Ar I emission lines, so there is no need to have a separate spectroscopy setup for measuring the molecular spectra. Other advantages of the first positive system over the other two band systems include strong emission intensity under most plasma conditions and minimal perturbations by neighboring states.[66], [79] An energy diagram of the three band systems of nitrogen is shown in Fig. 3.14 to help visualize the radiative decay channels of these band systems.

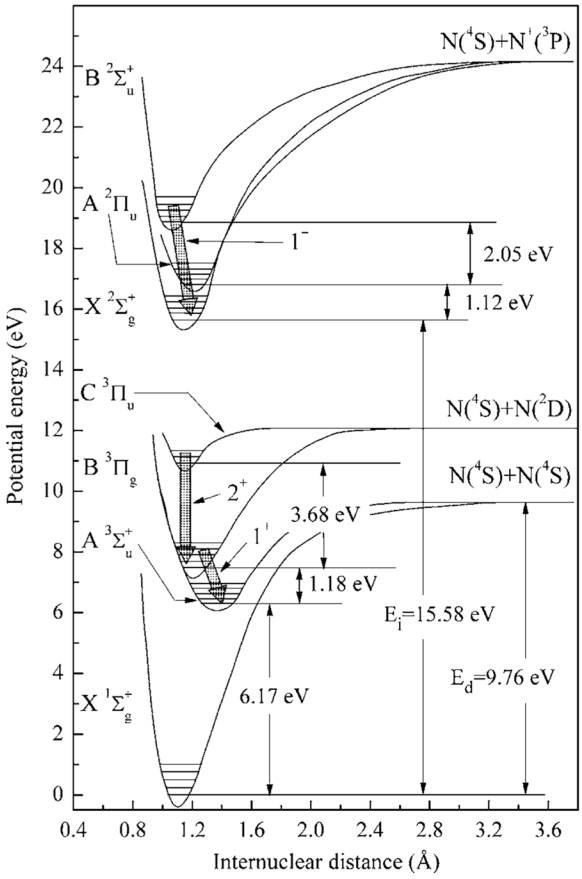

Figure 3.14: Energy diagram of different nitrogen states. The radiative decay channels of the first negative, first positive, and second positive systems are denoted by shaded arrows. Reprinted from C. Biloiu *et al*., J. Appl. Phys. **101**, 073303 (2007), with the permission of AIP Publishing.

The main disadvantage of the first positive system is that it has a complex structure resulting in a lack of interest in the band system for gas temperature approximations; only four models for the first positive system were found in literature.[64]–[66], [78], [84] Out of the four models found in literature only the Biloiu and Simek models work within the tested operating conditions. Biloiu *et al.* were generous enough to provide the scientific community with a copy of their fitting code along with the line positions and intensities used to generate the synthetic spectrum, so it was decided to implement their readily available model into the analysis of the nitrogen rovibrational bands observed in our experiments.[66]

The Biloiu model calculates the rotational temperature by fitting numerically generated spectra to experimental measurements.[66] The line positions implemented in this model were calculated and experimentally verified by Effantin *et al.*[85] Intensities of individual rotational lines were calculated by

$$\mathrm{I}^{\mathrm{n'\upsilon'J'}}_{\mathrm{n''\upsilon''J''}} = \mathrm{N}_{\mathrm{n'\upsilon'J'}} A^{n'\upsilon'J'}_{n''\upsilon''J''} \frac{\mathrm{h}c}{\lambda} , \tag{3.43}$$

where $\mathrm{N}_{\mathrm{n'\upsilon'J'}}$ is the population of the emitting level, $A^{n'\upsilon'J'}_{n''\upsilon''J''}$ is the Einstein transition probability, and λ is the wavelength of the emitted radiation.[66] The model requires the user to input two instrument dependent parameters to correct the generated spectrum for instrumental broadening. Instrumental broadening is approximated by fitting a pseudo-Voigt function to an Ar I emission line in the vicinity of the rovibrational band of interest since the instrument function varies as a function of wavelength for a fixed slit width. The pseudo-Voigt function is given by

$$\mathrm{f}(p,w) = p\frac{\sqrt{4\ln 2}}{w\sqrt{\pi}}\exp\left[-\frac{4\ln 2}{w^2}(\lambda-\lambda_0)^2\right] + (1-p)\frac{2w}{\pi[w^2+4(\lambda-\lambda_0)^2]} , \tag{3.44}$$

where p and $1-p$ are the relative magnitudes of the Gaussian and Lorentzian functions contributions, respectively, w is the FWHM of the line, and λ_0 is the central wavelength of the line shape.[66] Parameters p and w determined from the best fit of the pseudo-Voigt function are the instrument dependent parameters the code provided by Biloiu *et al*. requires the user to define.[66] In our case, fitting to the 794.8 nm Ar I line resulted in 0.653 and 0.127 nm for values of p and w, respectively. The fitted pseudo-Voigt function is shown in Fig. 3.15.

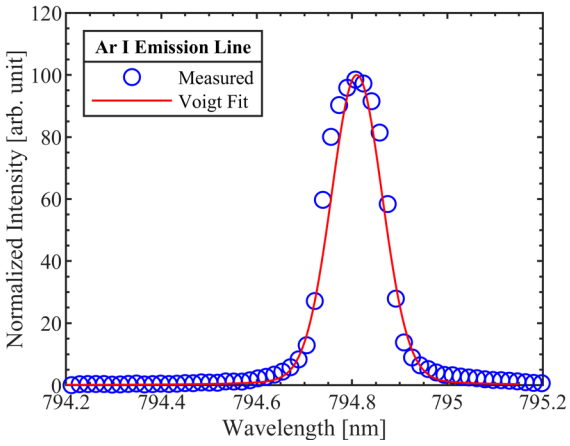

Figure 3.15: Pseudo-Voigt function fitted to Ar I emission line (794.8 nm). Data is from Ar-N_2 (4% N_2) plasma generated at the focus of a 7.5 kW microwave beam at 200 mTorr.

The first thing that was noticed when using the code provided by Biloiu *et al*. was that the Ar I emission line in the middle of the 2-0 band was unacceptably degrading the accuracy of the fitting algorithm. Initial attempts to remove contributions of the Ar I line to the rovibrational band resulted in a loss of peak features between the sub-band heads corresponding to the turning points of the R_{33} and P_{33} branches; the referenced band region is shown in Fig. 3.16. The initial correction method implemented significantly improved the model's nonlinear chi-squared value given by,

$$\chi^2(T_r) = \frac{\sum_{k=1}^{Z_d}[I_k^r - I_k^s(T_r)]^2}{Z_d(Z_d - 1)}\ , \tag{3.45}$$

where Z_d is the number of points in the recorded rovibrational band, I_k^r is the normalized and corrected measured intensity, and I_k^s is the intensity of the simulated spectrum.[66] However, when analyzing plasma generated at minimum microwave beam power conditions (minimum input power required to sustain the discharge), there were times when the calculated rotational temperature would be below room temperature. This brought into question the accuracy of the correction method, so alternative methods were investigated for the removal of Ar I intensity contributions to the band, while minimizing losses of the band features.

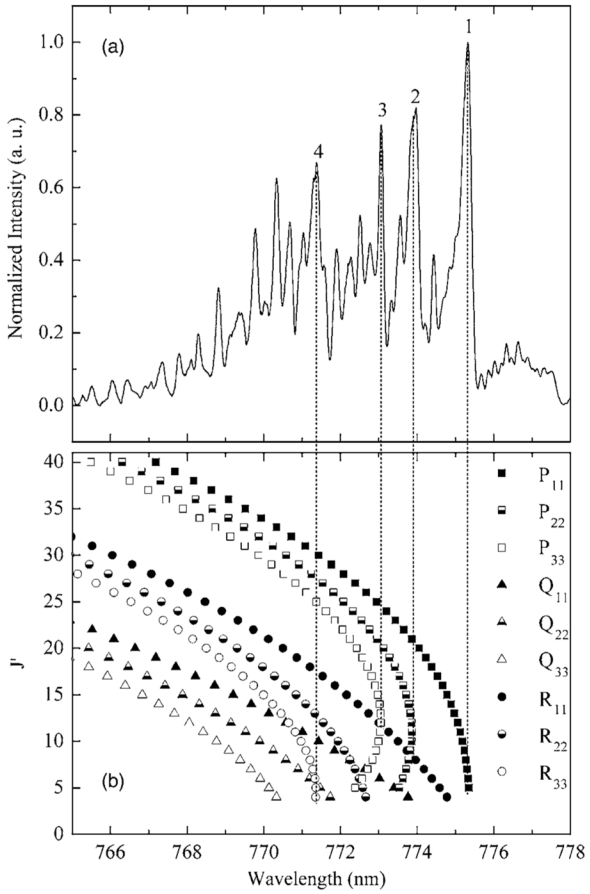

Figure 3.16: Spectrum of the 2-0 rovibrational band of the first positive system of nitrogen recorded by Biloiu *et al*. **(a)** Sub-band heads denoted by numbers 1-4 correspond to the **(b)** turning points of the P_{11}, P_{22}, P_{33}, and R_{33} branches. Reprinted from C. Biloiu *et al*., J. Appl. Phys. **101**, 073303 (2007), with the permission of AIP Publishing.

The code provided by Biloiu *et al*. allows the user to change the parameters used for the initial guess of the fitting function; the user can define the rotational temperature, background noise level, and wavelength shift for the initial guess and view the corresponding spectra of the initial guess.[66] Using this feature, one can use the third and fourth sub-band heads (peaks 3 and 4 shown in Fig. 3.16) as references for fitting simulated spectra (between the two sub-band heads) from initial guesses of the temperature. The simulated spectrum can then be used to replace the measured spectrum that is in the vicinity of the Ar I emission line before fitting a synthetic spectrum to the entire 2-0 rovibrational band. Note that the Ar I emission line consists of two Ar I lines (772.38 nm and 772.42 nm) that are observed as one line by our spectroscopy system, so

one has to be cautious when determining how much of the measured spectrum to replace with synthetic spectrum; measured spectrum within 0.5 nm of the central wavelength of the Ar I doublet was replaced in this case, as shown in Fig. 3.17. This correction method resulted in significantly lower χ^2 values, and most important, realistic temperatures overall Ar-N_2 plasma tested conditions. Modifications made to the code provided by Biloiu's *et al*. can be found in Appendix B; these include removal of the Ar I emission contributions to the 2-0 band and calculation of the rotational temperature's 95% confidence interval.

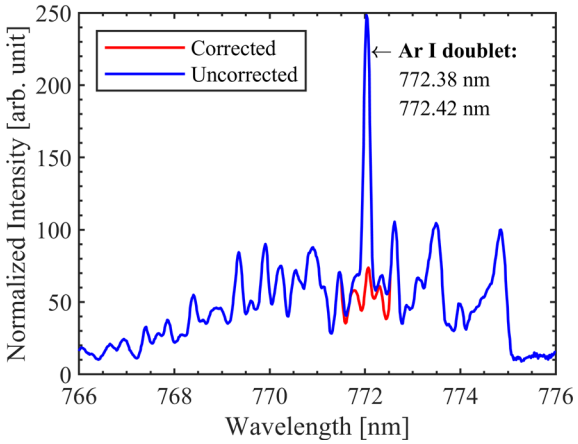

Figure 3.17: Uncorrected spectrum of the 2-0 band of the first positive system of nitrogen is compared to spectrum corrected for Ar I emission contributions using synthetic spectrum from Biloiu's model.[66]

3.2.7 Gas Temperature: Simek's Model

Simek's model[6] was implemented in this investigation to assess the accuracy of the correction method used with Biloiu's model. Unlike Biloiu's model, Simek's model only uses the intensity ratios of the sub-band heads to estimate the rotational temperature, which means corrections for the contributions of Ar I emissions are not necessary. The temperature estimation method developed by Simek and Bendictis rely on the fact that the relative population of the $^3\Pi_\Omega$

[6] Simek's model was originally developed to work with the 3-0 band of the first positive system of nitrogen, but later it was extended to the 0-0, 1-0, and 2-0 bands. The original work was published in a peer-reviewed journal, but the extension of the model to the other bands was only released as a research report for the Institute of Plasma Physics Czechoslovak Academy of Science, which makes it difficult to find when doing a literature search.[64], [65]

sub-states in the $N_2(B^3\Pi_u)$ state is dependent on the rotational temperature.[65] Similar to the Biloiu model, the population of a single rotational level is calculated assuming Hund's case (a):

$$N_{n\upsilon J} = N(\upsilon)\frac{2\Phi(2S+1)(2J+1)\exp\left\{-\frac{hc}{k_B T_r}[T_{el} + \ _{vib}(\upsilon) + A_\upsilon \Lambda\Sigma + F(J)]\right\}}{Q_{el}Q_{vib}Q_{rot}\sum_{-S}^{S}\left[-A_\upsilon \Lambda\Sigma\frac{hc}{k_B T_r}\right]}, \quad (3.46)$$

where T_{el}, $F(J)$, $_{vib}(\upsilon)$, Q_{el}, Q_{vib}, and Q_{rot} are electronic, rotational, and vibrational spectral terms and partition functions, respectively, $N(\upsilon)$ is the total population of vibrational level υ, A_υ is the spin-orbit constant, and Φ is an alternation factor dependent on the nuclear spin and parity of the rotational level.[86] The intensity of a single rotational line is then calculated by

$$I_{J'J''} = \frac{64\pi^4 \nu_{J'J''}^4 q_{\upsilon'\upsilon''}|R_e|^2 S_{J'J''}}{3c^3(4\pi\epsilon_0)(2J'+1)} N_{n'\upsilon'J'}, \quad (3.47)$$

where $\nu_{J'J''}$ is the frequency of the emitted radiation, $S_{J'J''}$ is the Hönl-London factor for the considered transition, $q_{\upsilon'\upsilon''}$ is the Franck-Condon factor, and R_e is the electronic-vibrational transition moment.[87]

A convolution of the numerically calculated intensities with a triangular instrument function is performed to account for instrumental broadening in their synthetic data; tables of coefficients that can return their simulated data and the temperature associated with it are provided for different spectral bandwidths.[64] Note that Simek and Benedictis define *W* as the slit width of the instrument early in the papers, but the equations and tables needed for the temperature calculations give *W* in angstroms which is several orders of magnitudes smaller than the typical slit width (tens to hundreds of micrometers).[64], [65] It is clear that *W* should be defined as the spectral bandwidth given that the figures and some of the tables in the papers associate *W* with the spectral bandwidth or bandpass.[64], [65] With that said, one can calculate the temperature using

the intensities of the peaks, I_1, I_2, and I_3 associated with the turning points of the P_{11}, P_{22}, and R_{33} branches, respectively.

Temperature calculations can be made using two different peak intensity ratios:[64], [65]

$$R_{21} = \frac{I_2}{I_1}, \tag{3.48a}$$

and

$$R_{31} = \frac{I_3}{I_1}. \tag{3.48b}$$

Using these ratios, the temperature can be calculated by

$$\mathrm{T}_{21} = \prod_{i=0}^{3} \exp\left(\sum_{j=0}^{4} x_{ij} W^{(j)} R_{21}^{(j)}\right), \tag{3.49a}$$

and

$$\mathrm{T}_{31} = \prod_{i=0}^{3} \exp\left(\sum_{j=0}^{4} y_{ij} W^{(j)} R_{31}^{(j)}\right), \tag{3.49b}$$

where x_{ij} and y_{ij} are model coefficients given in tables by Simek.[64] The spectral bandwidth of the spectroscopy system used for our measurements is 1.27 Å in the vicinity of the 2-0 rovibrational band; this value is the same as the *w* parameter calculated for the Biloiu's model. The tables provided by Simek do not provide x_{ij} and y_{ij} values in the range of our spectral bandwidth, but the tables containing the least-square polynomial coefficients $a_i(W)$ and $b_i(W)$ do have data in this range. The least-square polynomial coefficients are given by

$$a_i(W) = \sum_{j=0}^{4} x_{ij} W^{(j)}, \tag{3.50a}$$

and

$$b_i(W) = \sum_{j=0}^{4} y_{ij} W^{(j)}, \tag{3.50b}$$

which can be substituted into Eqns. 3.49a and 3.49b to calculate the temperature.[64] Temperatures calculated from both peak intensity ratios yielded values within a few Kelvin from each other, so the temperatures were averaged before comparing models. For all tested Ar-N_2 plasma conditions, Simek's and Biloiu's models yield temperatures within the error range of each other, giving us confidence in the accuracy of the correction method implemented for the removal of Ar I emissions from the 2-0 rovibrational band. Note that the error bar in Simek's model is set by the 25 K step temperature resolution used for the generation of their synthetic data.[64], [65] A temperature comparison of the models is shown in Fig. 3.18.

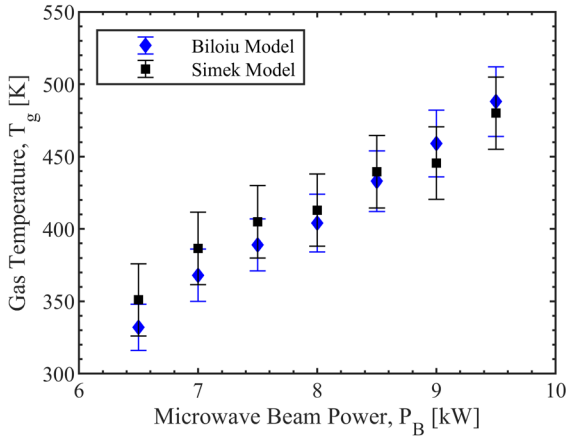

Figure 3.18: Gas temperature calculated using Biloiu's and Simek's models are compared as a function of input microwave beam power for an Ar-N_2 plasma containing 6% N_2 at 200 mTorr. Note that the models measure the rotational temperature, but the gas temperature can be approximated by the rotational temperature under the tested conditions.

3.2.8 Collisional Radiative Model

The electron temperature of the plasma can be approximated from intensity ratios of the Ar I emission lines. Initial attempts to measure the electron temperature of plasma generated in the AFRL's experimental setup were done using the corona model, which is a common method to deduce population equilibrium in low electron density, low temperature plasmas.[2] However, the

corona model used did not take into consideration excitations out of argon metastable states, which can reduce the accuracy of the model.[2] Considering several of the Ar I emission lines observed in the optical range are from radiative decays into metastable states, it is likely for them to contribute to the population of higher energy states.

In a collaboration with the Space Vehicles Directorate of the AFRL, a CRM for Ar plasma based on a CRM for Xe plasma developed by Dressler *et al*. has been under development.[67] Before going into the details of the CRM, it is important to note that many CRMs use Paschen notation to describe excited states. Given that the Paschen notation can be confusing, a brief explanation of the notation and a table relating the Paschen notation to the LS notation of argon states considered in our CRM will be provided. Paschen notation is commonly used when describing the excited states of Ne, Ar, Kr, and Xe. Paschen notation takes the form of $n'l_s$, where l is the orbital quantum number of the excited electron, n' is a number that attempts to describe the energy level of the excited electron as if it was in a hydrogen atom, and s indicates the energy level of the sub-state in decreasing order (e.g., the sub-state indicated by $s = 10$ is at a lower energy level than one indicated by $s = 9$). For the most part, determining the value of n' is the most confusing concept of the Paschen notation as it's related to l by

$$l = n' - 1, n' - 2, \ldots, 0 \tag{3.51}$$

which causes the starting value of n' to change as the orbital quantum number changes; for a given orbital quantum number, n' increases as the energy level of the excited electron increases. Argon excited states considered in our CRM are listed in Table 3.1 with their LS and Paschen notations.

Table 3.1: Excited state of argon in LS and Paschen notation.

LS Notation	Paschen Notation
$3s^2 3p^5 4p(^1S_0)$	$2p_1$
$3s^2 3p^5 4p(^3P_1)$	$2p_2$
$3s^2 3p^5 4p(^3P_2)$	$2p_3$
$3s^2 3p^5 4p(^1P_1)$	$2p_4$
$3s^2 3p^5 4p(^3P_0)$	$2p_5$
$3s^2 3p^5 4p(^1D_2)$	$2p_6$
$3s^2 3p^5 4p(^3D_1)$	$2p_7$
$3s^2 3p^5 4p(^3D_2)$	$2p_8$
$3s^2 3p^5 4p(^3D_3)$	$2p_9$
$3s^2 3p^5 4p(^3S_1)$	$2p_{10}$
$3s^2 3p^5 4s(^1P_1)$	$1s_2$
$3s^2 3p^5 4s(^3P_0)$	$1s_3$
$3s^2 3p^5 4s(^3P_1)$	$1s_4$
$3s^2 3p^5 4s(^3P_2)$	$1s_5$

The CRM used in this investigation, focuses on optical and NIR emission from the $2p_i$ to $1s_j$ levels, similar to the corona model implemented by Hoff *et al*. for preliminary electron temperature measurements of the plasma generated in the experimental setup.[2] The main difference between the models is that electron collisions with the $1s_3$ and $1s_5$ metastable states are included in the CRM. Transitions from the $1s_3$ and $1s_5$ states to most of the $2p_i$ states are electric dipole allowed, while transitions from the metastable states to $2s_j$ and $3d_k$ states are not.[88] This is important since it means that metastable states contribute to the population of the $2p_i$ states. Furthermore, the contributions to the population of $2p_i$ states from metastable states can be significant since it takes less energy to excite an atom from an excited state than to excite an atom from its ground state. This can be seen from the tables of rate coefficients provided by Zhu and Pu where the transitions from metastable states to $2p_i$ states have higher rate coefficients than

transitions from ground state to $2p_i$ states.[89] An example of the rate coefficients for transitions into the $2p_2$ state via electron impact excitation is shown in Fig. 3.19.

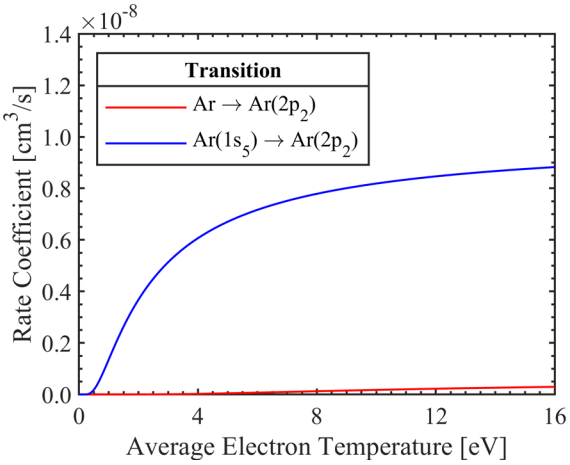

Figure 3.19: Rate coefficients as a function of the average electron temperature for transitions into the $2p_2$ state via electron impact excitation. Rate coefficients are based on the equations from Zhu and Pu.[89]

In the CRM, the $2p_i$ states are populated by electron impact excitation of the ground state, and the $1s_3$ and $1s_5$ metastable states; these reactions are listed in Table 3.2 (reactions 1-12) and Table 3.3 (reactions 1-10). Ion contributions are ignored since their kinetic energy is expected to be too low to contribute to the population of those states. Depopulation of the $2p_i$ states is assumed to be only through radiative decay to lower energy states as spontaneous emissions occur at much faster timescales than de-excitation via electron impacts. Metastable states are populated from electron impact excitation of ground state atoms, and radiative decay of the $2p_i$ states; collision-based reactions that contribute to the population of metastable states are listed in Table 3.3 (reactions 11-12). Our CRM currently depopulates the metastable states via electron impact excitation into the $1s_2$, $1s_4$, $2p_i$ and 3p states, and electron impact ionization; these reactions are listed in Table 3.2 (reactions 13-18). Atom-collision population transfer processes, such as

$$\mathrm{Ar} + \mathrm{Ar}(1s) \leftrightarrow \mathrm{Ar} + \mathrm{Ar}(2p_9)\,, \tag{3.52}$$

are not considered in the depopulation of metastable states as the rate coefficients of such processes at low gas temperatures are three to four orders of magnitude lower than those of electron

impact excitation processes. Other depopulation processes that can affect metastable states include diffusion (affects low electron density plasmas) and de-excitation via collision with non-argon molecules (e.g. nitrogen and oxygen); these processes will be added to future iterations of the CRM for improved accuracy of the model.[88], [90]

Table 3.2: Electron impact excitation and ionization of metastable atoms. Rate coefficient equations are from Zhu and Pu.[89]

	Reaction	Rate Coefficient [cm^3/s]
1	$e + Ar(1s_3) \leftrightarrow e + Ar(2p_2)$	$2.0\times10^{-7}\exp(-2/T_e)$
2	$e + Ar(1s_5) \leftrightarrow e + Ar(2p_2)$	$1.0\times10^{-8}\exp(-2/T_e)$
3	$e + Ar(1s_5) \leftrightarrow e + Ar(2p_3)$	$2.0\times10^{-8}\exp(-2/T_e)$
4	$e + Ar(1s_3) \leftrightarrow e + Ar(2p_4)$	$5.0\times10^{-8}\exp(-2/T_e)$
5	$e + Ar(1s_5) \leftrightarrow e + Ar(2p_4)$	$1.0\times10^{-8}\exp(-2/T_e)$
6	$e + Ar(1s_5) \leftrightarrow e + Ar(2p_6)$	$2.0\times10^{-7}\exp(-2/T_e)$
7	$e + Ar(1s_3) \leftrightarrow e + Ar(2p_7)$	$8.0\times10^{-8}\exp(-2/T_e)$
8	$e + Ar(1s_5) \leftrightarrow e + Ar(2p_7)$	$2.0\times10^{-8}\exp(-2/T_e)$
9	$e + Ar(1s_5) \leftrightarrow e + Ar(2p_8)$	$1.0\times10^{-7}\exp(-2/T_e)$
10	$e + Ar(1s_5) \leftrightarrow e + Ar(2p_9)$	$6.0\times10^{-7}\exp(-2/T_e)$
11	$e + Ar(1s_3) \leftrightarrow e + Ar(2p_{10})$	$1.5\times10^{-7}\exp(-2/T_e)$
12	$e + Ar(1s_5) \leftrightarrow e + Ar(2p_{10})$	$3.0\times10^{-7}\exp(-2/T_e)$
13	$e + Ar(1s_3) \leftrightarrow e + Ar(1s_2)$	$1.0\times10^{-7}T_e^{-0.6}$
14	$e + Ar(1s_3) \leftrightarrow e + Ar(1s_4)$	$2.0\times10^{-8}T_e^{-0.6}$
15	$e + Ar(1s_5) \leftrightarrow e + Ar(1s_2)$	$2.0\times10^{-8}T_e^{-0.6}$
16	$e + Ar(1s_5) \leftrightarrow e + Ar(1s_4)$	$1.0\times10^{-7}T_e^{-0.6}$
17	$e + Ar(1s) \leftrightarrow e + Ar(3p)$	$5.0\times10^{-8}\exp(-3/T_e)$
18	$e + Ar(1s) \leftrightarrow e + e + Ar^+$	$2.0\times10^{-7}\exp(-6.2/T_e)$

Table 3.3: Electron impact excitation of ground state atoms. Rate coefficient equations are from Zhu and Pu.[89]

	Reaction	Rate Coefficient [cm^3/s]
1	$e + Ar \leftrightarrow e + Ar(2p_1)$	$2.2\times10^{-9}\exp(-13.9/T_e)$
2	$e + Ar \leftrightarrow e + Ar(2p_2)$	$7.0\times10^{-10}\exp(-13.8/T_e)$
3	$e + Ar \leftrightarrow e + Ar(2p_3)$	$1.3\times10^{-9}\exp(-13.7/T_e)$
4	$e + Ar \leftrightarrow e + Ar(2p_4)$	$1.0\times10^{-9}\exp(-14.0/T_e)$
5	$e + Ar \leftrightarrow e + Ar(2p_5)$	$1.0\times10^{-9}\exp(-13.6/T_e)$
6	$e + Ar \leftrightarrow e + Ar(2p_6)$	$1.5\times10^{-9}\exp(-13.5/T_e)$
7	$e + Ar \leftrightarrow e + Ar(2p_7)$	$1.1\times10^{-9}\exp(-13.9/T_e)$
8	$e + Ar \leftrightarrow e + Ar(2p_8)$	$2.2\times10^{-9}\exp(-13.6/T_e)$
9	$e + Ar \leftrightarrow e + Ar(2p_9)$	$1.9\times10^{-9}\exp(-13.5/T_e)$
10	$e + Ar \leftrightarrow e + Ar(2p_{10})$	$2.0\times10^{-9}\exp(-13.0/T_e)$
11	$e + Ar \leftrightarrow e + Ar(1s_3)$	$2.7\times10^{-9}\exp(-11.9/T_e)$
12	$e + Ar \leftrightarrow e + Ar(1s_5)$	$5.5\times10^{-10}\exp(-12.2/T_e)$

The plasma radiation intensity per unit volume for a specific emission line at wavelength, λ, can be approximated by

$$J_\lambda = \frac{hc}{4\pi\lambda} n_0 n_e R_b^\lambda \left(k_{e0}^\lambda + \frac{n_{s3}}{n_0} k_{es3}^\lambda + \frac{n_{s5}}{n_0} k_{es5}^\lambda \right), \tag{3.53}$$

where n_0, n_{s3}, and n_{s5}, are the neutral, $1s_3$ metastable, and $1s_5$ metastable atom number densities, respectively, R_b^λ is the branching ratio corresponding to the emission line, and k_{e0}^λ, k_{es3}^λ, and k_{es5}^λ are the rate coefficients for electron impact excitations into the $2p_i$ state associated with the emission line from the ground, $1s_3$, and $1s_5$ states, respectively.[91] The steady-state metastable fraction can be calculated by

$$\frac{n_m}{n_0} = \frac{k_{0m} + \sum_q (k_{e0}^q)}{\sum_r (R_{b,s}^r k_{2pm}^r) + \sum_k (k_{dm}^k) + k_{ion}}, \tag{3.54}$$

where n_m is the metastable atom number density, k_{0m} is the rate coefficient for electron impact excitations into the metastable state from the ground state, k_{e0} is the rate coefficient for electron impact excitation of ground state atoms into $2p_i$ states that radiative decay into the metastable state,

k_{2pm} is the rate coefficient for electron impact excitation of the metastable state into $2p_i$ states, $R_{b,s}$ is the branching ratio corresponding to the radiative decay of the $2p_i$ state to the $1s_j$ state that is optically coupled to the ground state, k_{dm} is the metastable excitation rate coefficient to states outside the $2p_i$ states (e.g., the $1s_2$ state), and k_{ion} is the electron impact ionization rate coefficient for the metastable atom. The branching ratios for the radiative decay of the $2p_i$ states into the $1s_j$ states were obtained from Tsurubuchi *et al*. and are listed in Table 3.4.[92]

Table 3.4: Radiative decay of $2p_i$ states into $1s_j$ states with their corresponding branching ratios and emission wavelengths. Information on the table was adapted from Zhu and Pu, and Tsurubuchi *et al*.[89], [92]

	Reaction	Branching Ratio	Wavelength [nm]
1	$Ar(2p_2) \rightarrow Ar(1s_5) + h\nu$	0.181	696.5
2	$Ar(2p_3) \rightarrow Ar(1s_5) + h\nu$	0.110	706.7
3	$Ar(2p_2) \rightarrow Ar(1s_4) + h\nu$	0.052	727.3
4	$Ar(2p_3) \rightarrow Ar(1s_4) + h\nu$	0.245	738.4
5	$Ar(2p_1) \rightarrow Ar(1s_2) + h\nu$	0.995	750.4
6	$Ar(2p_5) \rightarrow Ar(1s_4) + h\nu$	1.000	751.5
7	$Ar(2p_6) \rightarrow Ar(1s_5) + h\nu$	0.712	763.5
8	$Ar(2p_2) \rightarrow Ar(1s_3) + h\nu$	0.332	772.4
9	$Ar(2p_7) \rightarrow Ar(1s_5) + h\nu$	0.154	772.4
10	$Ar(2p_4) \rightarrow Ar(1s_3) + h\nu$	0.561	794.8
11	$Ar(2p_6) \rightarrow Ar(1s_4) + h\nu$	0.142	800.6
12	$Ar(2p_8) \rightarrow Ar(1s_5) + h\nu$	0.288	801.5
13	$Ar(2p_7) \rightarrow Ar(1s_4) + h\nu$	0.743	810.4
14	$Ar(2p_9) \rightarrow Ar(1s_5) + h\nu$	1.000	811.5
15	$Ar(2p_2) \rightarrow Ar(1s_2) + h\nu$	0.434	826.5
16	$Ar(2p_3) \rightarrow Ar(1s_2) + h\nu$	0.645	840.8
17	$Ar(2p_8) \rightarrow Ar(1s_4) + h\nu$	0.667	842.5
18	$Ar(2p_4) \rightarrow Ar(1s_2) + h\nu$	0.419	852.1

Eighteen Ar I emission lines in the 690 nm to 860 nm spectral range were observed in all tested conditions; the Ar I lines observed are listed in Table 3.4. However, many of the emission lines were unusable for electron temperature calculations. Eight Ar I emission lines overlap with

the 2-0 rovibrational bands of nitrogen approximately located in the 720 nm to 780 nm wavelength range. Attempts to calculate the electron temperature from the intensity line ratio of two of the remaining ten emission lines were unsuccessful due to the ratios being sensitive over only a narrow range of temperatures or being non-monotonic as a function of temperature; an example of a non-monotonic line ratio is shown in Fig. 3.20. While the accuracy of the temperature approximation typically increases the more emission lines one includes, two-line approximations are useful when trying to map the electron temperature of the plasma since the time of the spectral measurements can significantly decrease if the two lines are in the vicinity of each other. Note that depending the how far apart the emission lines are from each other, a spectrometer with the ability to scan wavelength can be needed.

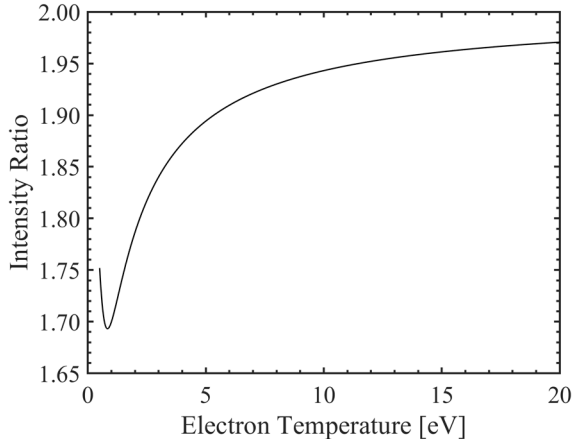

Figure 3.20: Intensity line ratio of the 801.5 nm and 800.6 nm emission lines.

A minimum of four lines had to be used to counter the non-monotonic behavior of certain line ratios. While testing for the temperature sensitivity of different line ratios, it was noticed that every time the 810.4 nm and 811.5 nm lines were included, the temperature approximated by the minimization of the chi-square fit could not be determined; it is unclear what causes the CRM to output the highest temperature of the simulated data whenever these two lines are included in the temperature approximation. The relative chi-square was calculated by

$$\chi^2 = \frac{1}{n_l}\sum_{i=1}^{n_l}\frac{\left(\mathrm{I_i^{exp}} - \mathrm{I_i^{CRM}}\right)^2}{\left(\mathrm{I_i^{exp}}\right)^2}, \tag{3.55}$$

where n_l is the number of emission lines, and $\mathrm{I_i^{exp}}$ and $\mathrm{I_i^{CRM}}$ are the normalized experimental and simulated line intensities. The combination of lines that produced the lowest chi-square values were the 696.5 nm, 706.7 nm, 801.5 nm, and 842.5 nm, most of which are from transitions into the $1s_5$ metastable state.

Chapter IV

Properties of Stable and Quasi-Stable Discharges

4.1 Plasma Stability

Three types of plasma discharges have been observed in the experimental setup: unstable, quasi-stable, and stable discharges.[2], [93] The stability of the plasma is sensitive to changes in the background gas pressure, gas flow rate, gas composition, and power of the microwave beam, with changes in the gas composition having the most impact on its stability. Unstable plasma discharges are the least common of the three discharges as they have only been observed in plasmas containing approximately 99% or more argon by concentration. The unstable mode is difficult to study directly as the lifetime of the discharge can vary from a few seconds to a little over a minute for a given set of conditions; currently there are no plans to study this type of discharge in the future. Quasi-stable discharges are not stable, but their dynamic behavior is repeatable over extended periods of times (hours) making them relatively easier to study compared to unstable discharges. Furthermore, studies completed for this work indicate that the discharge could be obtained in any gas mixture of argon, nitrogen, and oxygen whenever there is enough power available in the microwave beam to push the electron density of the plasma close to its critical density. This type of discharge is of interest because it can be sustained far removed from the chamber walls resulting in minimal plasma-wall and beam-wall interactions.

4.2 Quasi-Stable Discharges

Argon is the main gas used to generate plasma in the experimental setup as it is relatively easy to sustain a discharge in the microwave beam compared to molecular gases, such as nitrogen. When flowing only argon into the chamber, it is difficult to obtain a stable discharge. Instead, the shape, position, and brightness of the plasma oscillates in time as it was described by Hoff *et al*. after observations of the quasi-stable discharge through a video camera; images captured of the discharge are shown in Fig. 4.1.[2] It was not until after fast frame rate cameras were installed that it was observed that what was perceived as flickering of the plasma were actually ionization fronts propagating upstream in the microwave beam (towards the microwave source) at 10s of cycles per second; images captured by the fast frame rate camera are shown in Fig. 4.2.

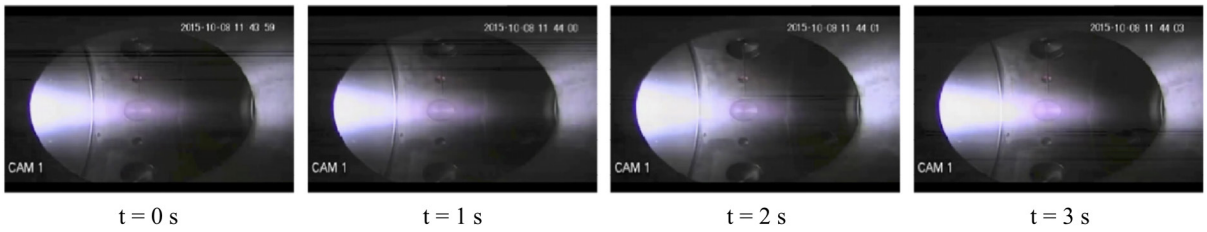

Figure 4.1: A single cycle of a quasi-stable discharge observed through a video camera. Approximately 45 cm of the discharge length was observed. Reprinted from B. W. Hoff *et al*., *Rev. Sci. Instrum*. **87**, 033507 (2016), with the permission of AIP Publishing.

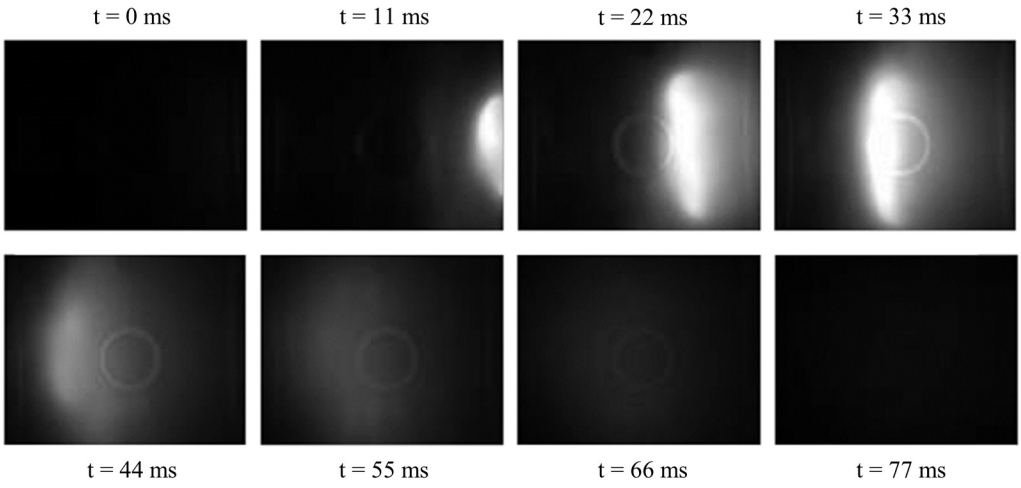

Figure 4.2: Quasi-stable discharge observed through a fast frame rate camera. Ionization fronts are approximately 10 cm wide with a 10-15 cm radius; size changes as the ionization front propagates upstream of the focus towards the microwave source.

The ionization fronts are generated when the plasma frequency (ω_p) is approximately equal to the frequency of the microwave beam (ω). When this happens, the plasma starts behaving more like a conductor than a dielectric resulting in an increase in the reflected component of the microwave beam. Reflection of the microwave beam increases as the dielectric permittivity of the plasma

$$\epsilon_\omega = 1 - \frac{\omega_p^2}{\omega^2 + \mathrm{i}\omega\nu_c} \tag{4.1}$$

approaches to zero; here ω is the angular frequency of the microwaves, ν_c is the electron-neutral collision frequency, and ω_p is the plasma frequency, which can be approximated by

$$\omega_p \cong \omega_{pe} = \sqrt{\frac{q_e^2 n_e}{m_e \varepsilon_0}}, \tag{4.2}$$

where ω_{pe} is the electron plasma frequency. The electron density corresponding to the condition in which the electromagnetic wave can no longer propagate through the plasma is known as the critical density and is given by

$$\mathrm{n_c} = \frac{\mathrm{m_e}\varepsilon_0(\omega^2 + {\nu_c}^2)}{\mathrm{q_e^2}} \ ; \tag{4.3}$$

the critical density of plasma generated in the experimental setup is approximately 2.7×10^{17} $\mathrm{m^{-3}}$. Constructive interference between the incident and reflected waves create regions of increased intensity near the leading edge of the plasma causing ionization of the gas in the vicinity. The electron density of this new plasma formation region quickly increases up to the critical density causing the microwaves to reflect off the plasma again and creating a new region of high intensity further upstream the microwave beam. This process repeats several times until the intensity is no longer strong enough to sustain the discharge at which point the plasma decays allowing the beam to reach the focus, heat residual electrons, and repeat the process. This cyclic process of ionization

fronts propagating upstream of the microwave beam's geometric focus (in vacuum) is referred to as a quasi-stable discharge.

It is important to note that the instability responsible for the rapid increase in the electron density is still unclear; thermal instabilities are currently being considered as the source of the rapid increase in electron density.[71], [94], [95] It is possible that the quasi-stable discharge is caused by a multi-step process, where an instability (like a thermal instability) first results in a rapid increase in the electron density until it is near the critical density, at which point ionization fronts start propagating due formation of high field regions upstream of the discharge (towards the microwave source). Thermal instabilities are said to occur when an initial disturbance in the neutral density or gas temperature leads to an increase in electron temperature, which causes an increase in the electron density, which results in a further drop of the neutral density and increase in the gas temperature, and cycle repeats resulting in a rapid increase of the electron density. The cycle for discharges containing molecular gases is well described by Nighan; a diagram of the thermal instability cycle presented by Nighan is shown in Fig. 3.3.[95] Further, studies are needed to determine the instability responsible for the rapid increase in the electron density.

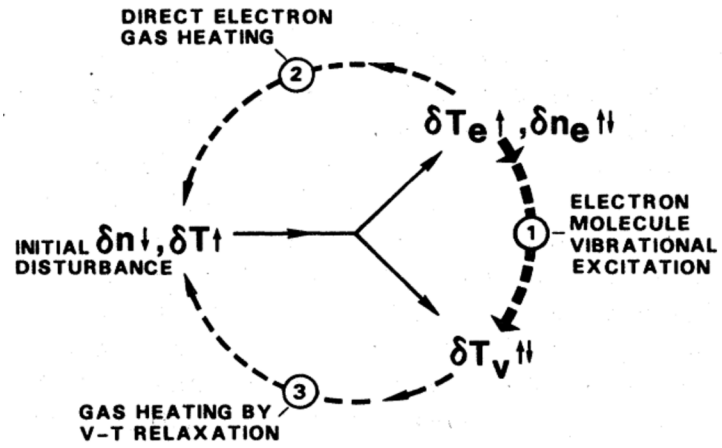

Figure 4.3: Thermal instability in discharges containing molecular gases.[95]

An interesting feature of the quasi-stable discharge is that the ionization fronts follow a propagation pattern (similar propagation paths and duration) for 10s to 10s of thousands of cycles before locking into a different propagation pattern. The repeatability of the cycles can be observed in the signals of the transmitted and reflected power of a quasi-stable discharge; the almost identical (typically less than 5% variation) signals of the transmitted microwave power of several ionization fronts are shown in Fig. 4.4. It is important to note the sharp drop in the transmitted microwave power over the cycle of an ionization front indicates the plasma becomes more reflective over a short period of time. This significant drop in transmitted power is consistent with the plasma density approaching the critical density.

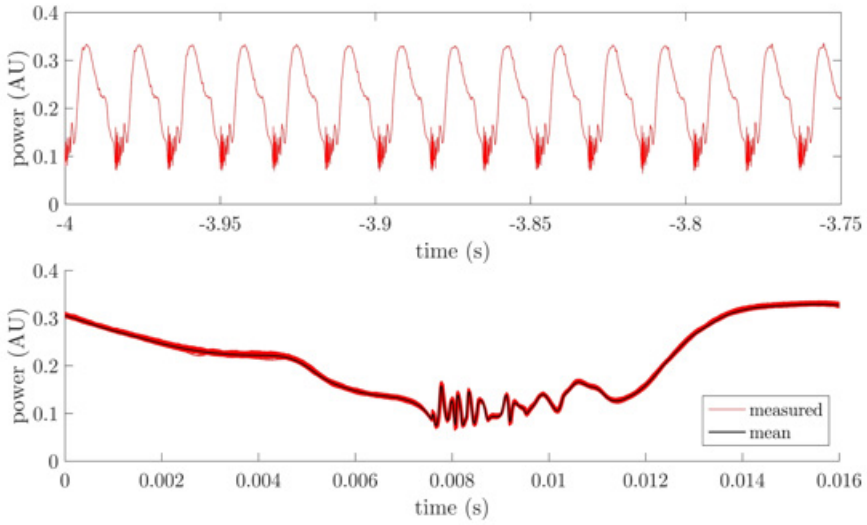

Figure 4.4: Transmitted microwave power recorded **a)** over 15 ionization cycles and **b)** 980 consecutive cycles (overlaid) of a quasi-stable discharge.[96]

Electron temperature and density measurements are difficult to make in a quasi-stable discharge as the ionization front moves too fast (100-300 m/s) for the translation stage that hold the plasma diagnostic systems to keep up with; the velocity of the ionization fronts was estimated via Doppler velocimetry measurements conducted by Reid.[96] However, stationary triple probes can provide some insight into the electron temperature and density of the quasi-stable discharge by making measurements of the ionization front as it passes through the probe. Given that the

measured transmitted and reflected power are almost identical from one cycle to the next, one would expect the electron density and temperature of the plasma measured by a stationary probe to be almost identical over every cycle too. This was confirmed through triple probe measurements of an Ar-N_2 (1% N_2) quasi-stable discharge generated in a 4.5 kW microwave beam at 200 mTorr; the measured electron temperature and density are shown in Fig. 4.5. It is important to note that corrections for operating in the transitional sheath regime were not made to the electron temperature and density measurements shown in Fig. 4.5 as the MATLAB code written for correcting triple probe measurements made outside the thin sheath regime is currently not optimized for quasi-stable discharges. A combination of long run times and loss of features (e.g., the peaks in the electron temperature and density) makes the code[7] inadequate for analyzing quasi-stable discharges; however, uncorrected data provides some insight into the periodicity of quasi-stable discharges and order of magnitude of the plasma parameters.

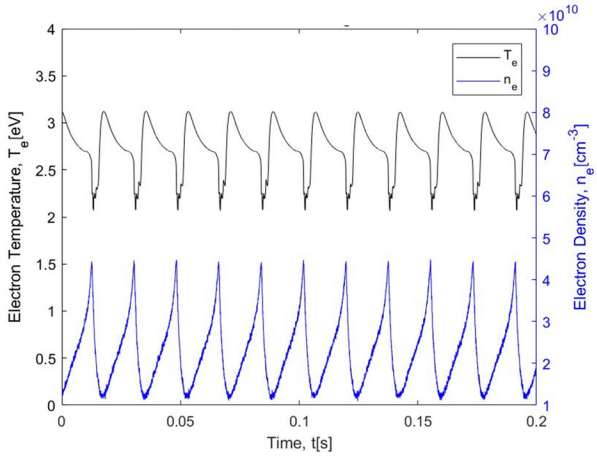

Figure 4.5: Electron temperature and density of a quasi-stable discharge measured by a triple Langmuir probe. Ar-N_2 (1% N_2) was generated with a 4.5 kW microwave beam at 200 mTorr.

[7] To improve the processing time of the code, the correction factor is only solved every time the probe radius to Debye length ratio changes by more than 0.1. This ratio changes gradually in stable discharges, while in quasi-stable discharges the change is abrupt resulting in the number of times the correction factor has to be calculated by the code and in a distortion of the measured plasma parameter profiles (looks like a step function).

A current challenge with electron temperature and density measurements of quasi-stable discharges is that it is unclear where the measurements were made relative to the ionization front. This issue will be addressed in future research efforts by synchronizing probe and optical emission spectroscopy measurements with images captured by the fast frame rate cameras. Another challenge with quasi-stable discharges is measuring the evolution of the electron temperature and density in the ionization front as it propagates. Stationary probes work well in quasi-stable discharges, but as soon as the probe is moved, the amount of time a cycle of a propagating ionization front (including decay and formation of the discharge) takes changes; this effect is shown in Fig. 4.6. Note that the probe location in Fig. 4.6 was calculated from the constant velocity (0.265 cm/s) of the stage and the time change measured by the DAQ; this means the duration of an ionization front cycle can be determined from the distance traveled by the probe in one cycle. For example, the first ionization front in Fig. 4.6 has a lifetime of approximately 63 ms, while the second to last ionization front lasts approximately 94 ms. This change in the duration of the ionization front cycles indicates the properties of the quasi-stable discharge are affected by changes in the probe location; noticeable changes are usually observed after the probe has traveled a little over 1.5 cm.

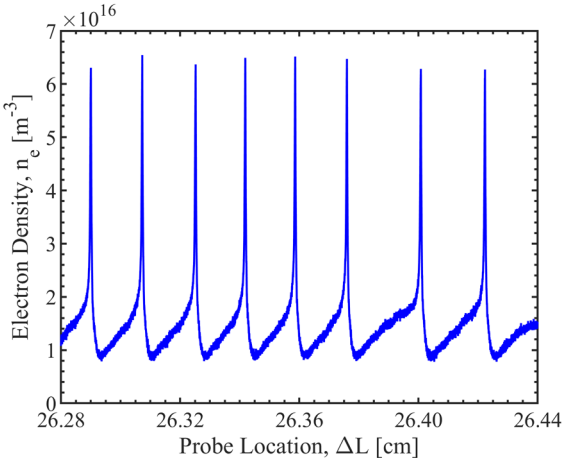

Figure 4.6: Electron density of a quasi-stable discharge measured by a moving (0.265 cm/s) triple probe. The Ar-N_2 (4% N_2) quasi-stable discharge was generated by an 8.0 kW microwave beam at 150 mTorr. The probe location is given with respect to the beam's geometric focus, where positive values are upstream in the microwave beam towards the microwave source.

One of the effects the triple probe has on the quasi-stable discharge is increase reflection of the microwaves. How much of the incident microwaves gets reflected by the wires depends on the surface area of the wires that is exposed to the microwave beam and the beam's intensity. As the probe moves away from the beam's geometric focus the surface area of the probe wires immersed in the beam increases, which should decrease the amount of reflected power given that the total power of the beam is distributed over a larger cross section. However, this would occasionally cause stable discharges to go quasi-stable, which indicates the probe is perturbing the beam and plasma in other ways that remain unclear. A moving probe usually causes stable discharges to transition to quasi-stable when the electron density of the discharge is in the order 10^{16} m^{-3}. The antenna effect is currently under consideration as a possible cause to the disturbances observed as the local field enhancement (in between the probe wires in this case) produced by the effect could be high enough to induce the instability. An example of a test where the probe caused a stable discharge to become quasi-stable is shown in Fig. 4.7; the relative direction the probe was traveling during the transition is shown in Fig. 4.8.

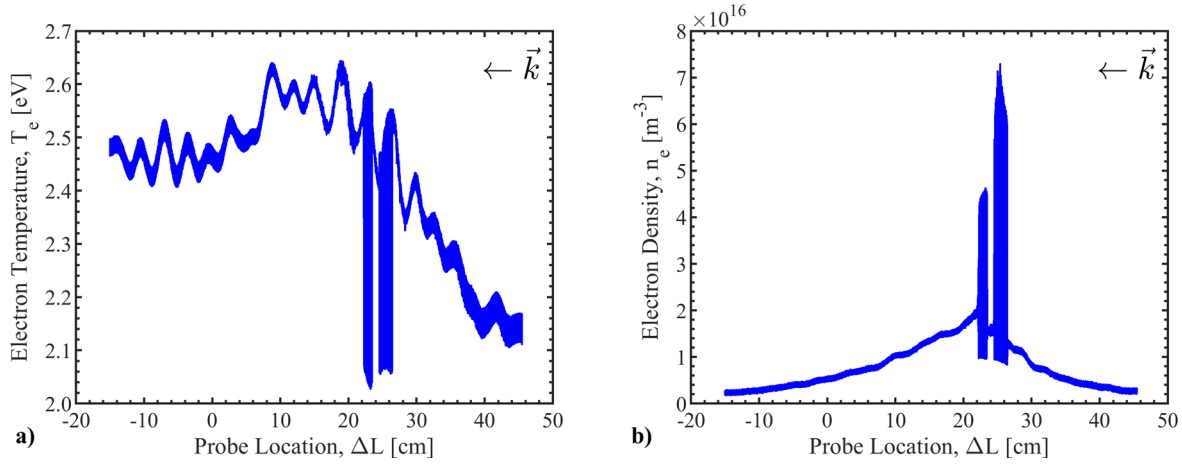

Figure 4.7: Electron **a)** temperature and **b)** density profiles of a stable Ar-N_2 (4% N_2) discharge becoming quasi-stable due to probe perturbations. Plasma was generated in an 8.0 kW microwave beam at 150 mTorr. Here the probe location is given with respect to the beam's geometric focus (ΔL = 0 cm), where positive values are upstream in the microwave beam towards the microwave source, and $\vec{k}$ is the microwave propagation vector. The regions with the spikes in the electron density and sharp drops in the electron temperature indicate the locations in which the stable discharge transitioned into the quasi-stable mode.

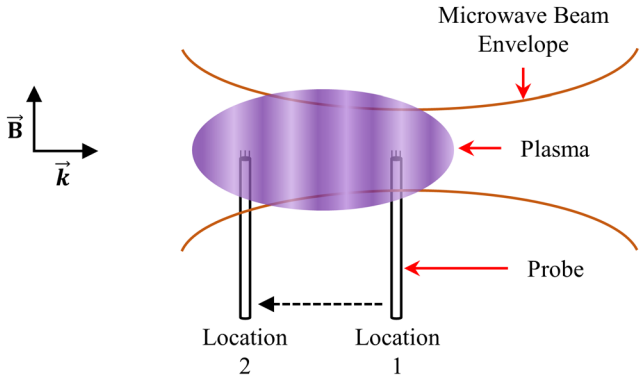

Figure 4.8: Probe moving upstream of the geometric focus. Note that more of probe's surface area is within the beam in "Location 2" than in "Location 1" resulting in a larger interaction cross section between the beam and the probe. $\vec{B}$ is the direction of the magnetic component of the electromagnetic waves.

Other factors that affect quasi-stable discharges include the flow rate of the gas, and the power of the microwave beam. Studies conducted where the gas pressure, microwave beam power, and gas composition were kept constant showed that approximately 150 sccm is needed to sustain discharges in the experimental setup, and that gas flow rates must be kept under 400 sccm for the turbo pump to function properly. For gas compositions containing 99% or more argon by concentration at fixed background gas pressure and microwave beam power, the quasi-stable discharge would go unstable when the gas flow rate went below 300 sccm. This behavior was observed at background gas pressures in the range of 150 mTorr to 200 mTorr. It is important to

note that Hoff *et al*. observed "pure" argon discharges at 200 sccm because the ECR plasma source that seeds electrons into the main chamber was kept on through the duration of their experiments effectively increasing the population of charged particles in the discharge; this effect was observed during studies conducted on the effect changes in the gas flow rated had on the discharges.[2] All experiments conducted for this investigation kept the ECR plasma source off after achieving gas breakdown in the main chamber.

Varying the power of the microwave beam in a quasi-stable discharge affects the frequency of the ionization fronts and the distance traveled by the fronts. A series of tests were conducted in which the power of the beam was varied while the gas pressure, flow rate, and composition were kept constant; the gas composition was kept at 99% Ar and 1% N_2 as quasi-stable discharges are dominant at this composition. The frequency of the oscillations in the discharge were measured with a stationary triple probe. Results showed no clear correlation between the power of the beam and the frequency of the oscillations in the discharge. However, live feed from the fast frame rate cameras showed that the distance traveled by the ionization front increased as the power of beam increased. This relation was true until the ionization front reached the borosilicate window at which point the discharge attached to the window. As the power of the beam was decreased to the lower limits in which the pure argon discharge could be sustained, the quasi-stable discharge transitioned into an unstable discharge before decaying; in argon discharges containing molecular gases, decreasing the beam power in a quasi-stable discharge results in a transition to a stable discharge.

4.3 Stable Discharges

Stable discharges are the most common type of discharges observed in the experimental setup when molecular gases, such as nitrogen and oxygen, are introduced into the argon plasma. The few times stable discharges have been observed in "pure" argon plasma could be attributed to the presence of contaminants, such as air and trapped water vapor, in the chamber. It is well known that adding molecular gases into a rare gas plasma, significantly changes the characteristics of the discharge due to more recombination channels becoming available and the introduction of vibrational states and the production of negative ions (in oxygen admixtures).[68], [71], [73], [90], [97], [98] The addition of recombination channels helps balance the ionization rate resulting in a decrease in the electron density; keeping the electron density below the critical density (approximately 2.7×10^{17} m^{-3}) allows stable discharges to be generated in the experimental. The EEDF of the discharge is effected by the vibrational states of the molecules as they have relatively large excitation cross sections at low electron energies resulting in decrease in the average electron energy of the electron population; this reduction in the average electron energy means there are less electrons in the discharge with enough energy to ionize the gas mixture resulting in a decrease of the ionization rate.

In this investigation, stable discharges were generated from different gas mixtures of argon, nitrogen, and oxygen. The total gas flow rate was kept constant in all the studies conducted with stable discharges to reduce the number of variables in the experiments; the flow rate was kept at 350 sccm based on the limits found in the studies of quasi-stable discharges. The gas pressure was varied from 100 mTorr to 200 mTorr for Ar-N_2 gas mixtures, but for plasmas containing oxygen the lower limit had to be increased to 150 mTorr due to difficulties with sustaining the discharge at the available power. The output power of the klystron amplifier was kept below its maximum

rated power of 10 kW. The concentration of molecular gases was increased in increments of 2% until the discharge could no longer be sustained. It is important to note that gas mixtures containing over 6% nitrogen (over 12% oxygen for Ar-O_2 plasmas) require more power than what is available to breakdown. For this reason, all experiments started with a plasma containing 2% of the molecular gas being studied before increasing its content. The microwave beam power was decreased in decrements of 0.5 kW starting from 9.5 kW in all experiments to keep observations and measurements consistent; the upper and lower limits of stable discharges were evaluated every 0.5 kW.

4.3.1 Ar-N_2 Gas Mixtures

Studies of Ar-N_2 stable discharges were conducted at three different gas pressures: 100 mTorr, 150 mTorr, and 200 mTorr. Experiments at 200 mTorr were able to support a wider range of gas compositions in which the concentration of nitrogen ranged from 2% to 10%. At 2% nitrogen, a quasi-stable discharge formed at breakdown, but the discharge was stabilized as the microwave beam power was reduced. The beam power at which the discharge stabilized was different for experiments conducted with the triple probe in comparison with experiments conducted with the collection optics; the discharge stabilized at approximately 4.0 kW and 6.5 kW for triple probe and optical emission spectroscopy experiments, respectively. This difference in the beam power could be attributed to the interactions between the microwave beam and the triple probe that have been found to induce instabilities in stable discharges.

Triple probe experiments have also been found to affect the lower power limit of stable discharges. For example, in Ar-N_2 (6% N_2) plasma generated with a 6.0 kW microwave beam at 200 mTorr, the probe extinguished the discharge as the probe traveled through the leading end of the plasma; it is unclear if power reflected by the probe is enough to deprive the plasma from the

power needed to sustain the discharge. The effects of having a probe in the microwave beam were most extensively when the discharge was quasi-stable at maximum beam power; this could be because more power is being reflected by the probe wires and possibly other local field enhancements mechanisms, such as the antenna effect, caused by the probe. As the power of the microwave beam was increased, the plasma gradually moved upstream of the beam's geometric focus while remaining stable. This meant that the probe also had to go further upstream towards the microwave source during the probe measurements resulting in the stable discharge transitioning to its quasi-stable mode, as explained in Sect. 4.1.1.

In general, the plasma exhibited similar stability behaviors under all tested gas pressures. As the concentration of nitrogen was increased, the minimum beam power required to sustain the Ar-N_2 discharge increased. This could be attributed to an increase in the available vibrational levels quenching the energy of the electrons resulting in a drop in the ionization rate; as the ionization rate falls, electron losses take over until the discharge completely decays. An increase in the maximum beam power at which a stable Ar-N_2 plasma could be sustained was also observed as the concentration of nitrogen increased. In this case, the higher concentrations of nitrogen increase the channels to which electrons can be lost, which help balance the increases in the ionization rate that come with an increase in power.

When the gas pressure was decreased, the minimum power required to sustain the discharge increased across all gas compositions. When gas pressure decreases at a constant volume and temperature, the neutral density also decreases resulting in a decrease in the electron-neutral collision frequency. Having less interactions between electrons and neutrals means the production of free electrons will also experience a decrease. To increase the ionization rate and balance the losses, an increase in the power of the microwave beam was required; total absorbed

power by the discharge increases with an increase in the input power. At 100 mTorr the power required to sustain the discharge increased to the point that gas mixtures containing over 2% nitrogen could not be sustained. For this reason, experiments conducted after the Ar-N_2 triple probe studies were carried out over a 150 mTorr to 200 mTorr range; 175 mTorr was added to the test gas pressure conditions for comparison purposes. The range of the microwave beam power for which Ar-N_2 stable discharges were obtained are provided in Tables 4.1 and 4.2. A diagram of the state of the discharge under various gas pressures, gas compositions, and beam power combinations is shown in Fig. 4.9. Note that the 100 mTorr condition is not shown in the diagram given that discharge could not be sustained for nitrogen concentrations above 2%; the power required to sustain discharges containing higher concentrations of nitrogen was more than what was available in the setup.

Table 4.1: Microwave beam power range in which Ar-N_2 stable discharges generated for triple probe experiments can be obtained for multiple gas pressures and concentrations of N_2.

N_2 [%]	200 mTorr		150 mTorr		100 mTorr	
	Min [kW]	Max [kW]	Min [kW]	Max [kW]	Min [kW]	Max [kW]
2	4.0	4.0	5.0	7.0	8.0	9.5
4	5.5	6.5	7.0	9.0	—	—
6	6.5	9.0	8.0	9.5	—	—
8	7.5	9.5	9.0	9.5	—	—
10	8.5	9.5	—	—	—	—

Table 4.2: Microwave beam power range in which Ar-N_2 stable discharges generated for optical emission spectroscopy experiments can be obtained for multiple gas pressures and concentrations of N_2.

N_2 [%]	200 mTorr		150 mTorr		100 mTorr	
	Min [kW]	Max [kW]	Min [kW]	Max [kW]	Min [kW]	Max [kW]
2	4.0	6.5	5.0	9.0	7.5	9.5
4	5.5	7.5	6.5	9.0	—	—
6	6.0	9.5	8.0	9.5	—	—
8	7.5	9.5	9.0	9.5	—	—
10	8.5	9.5	—	—	—	—

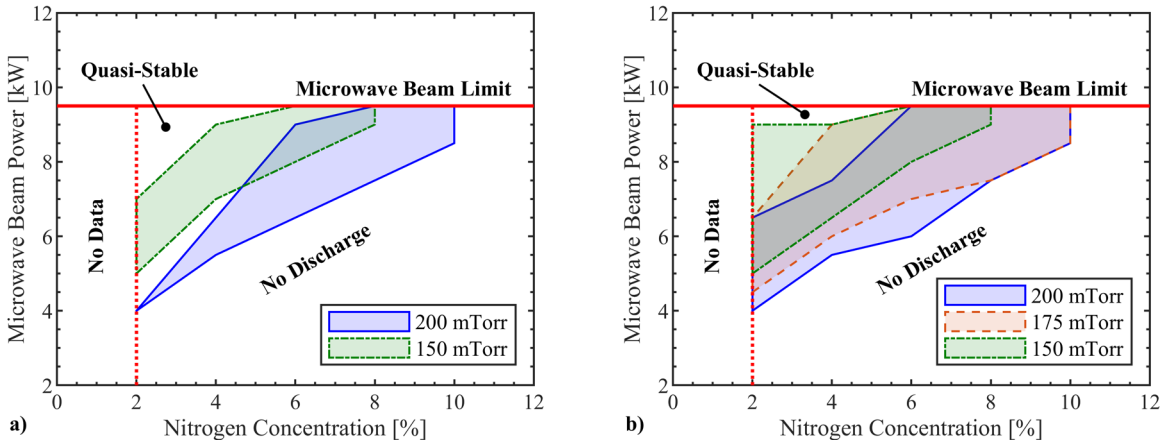

Figure 4.9: Stability of Ar-N_2 plasma discharges under various operating conditions for **a)** triple probe and **b)** optical emission spectroscopy experiments. The shaded regions represent the combination of parameters (beam power, nitrogen concentration, and gas pressure) that yield stable discharges. Regions above and below the boundary line of the stable discharge region yield quasi-stable discharges and no discharges, respectively. Note that there is insufficient or no data to determine stability boundaries for nitrogen concentrations below 2%. The microwave beam limit was set by the operating limits of the power supply.

4.3.2 Ar-O_2 Gas Mixtures

When oxygen was added to the argon plasma instead of nitrogen, the plasma generated appeared dimmer, longer, and centered closer to the beam's geometric focus than Ar-N_2 discharges. The range of the beam power and molecular gas concentration at which stable discharges were obtained also increased significantly; the amount of oxygen that could be added to the gas mixture before the discharge was no longer sustainable was approximately twice that of nitrogen. This can be attributed to oxygen having a much smaller effective cross-section than nitrogen for electron impact excitation from the ground state to its vibrational states.[98] The cross section for vibrational excitation of the oxygen from its ground state peaks at electron energies of approximately 10 eV; electrons with such energy would have enough energy to dissociate oxygen ($D_0(O_2)$ = 5.1 eV).[99]–[102] Furthermore, even at its peak cross section, oxygen's vibrational excitation cross section is approximately an order of magnitude smaller than that of nitrogen.[103]–[105]

Negative molecular oxygen ions do have relatively large vibrational excitation cross sections at low electron energies; however, a series of reactions must first occur before those vibrational level become available. Electrons must first collide and dissociate O_2 to produce O and O^-, which are needed to produce O_2^-. A few reactions that can produce O and O^- include:

$$e + O_2 \longrightarrow O^- + O\,, \tag{4.4}$$

$$e + O_2^* \longrightarrow O^- + O\,, \tag{4.5}$$

$$e + O_2(\upsilon = 1) \longrightarrow O^- + O\,. \tag{4.6}$$

The dissociative electron attachment cross sections are in the order of 10^{-19} cm^2 to 10^{-18} cm^2 for electron energies in range of 5 eV to 9 eV.[101], [106] These are one to two orders of magnitude smaller than the vibrational excitation cross sections of O_2 in most of that energy range; however, the low dissociation energy increases the chances of dissociating any molecular oxygen state (ground state, electronically excited states, and vibrationally excited states). When O_2^- finally forms, it is likely that most of it ends up dissociating before getting vibrationally excited by a low energy electron given its dissociation energy is approximately 4.07 eV.[107] Dissociative electron attachment and vibrational excitation cross sections of $O_2(^3\Sigma_g^-)$ were digitized and are shown in Fig. 4.10. The vibrational excitation cross sections of $N_2(^1\Sigma_g^+)$ and $O_2^-(^2\Pi_g)$ were also digitized and are shown in Fig. 4.11.

The expected low concentrations of O_2^- was confirmed by *GlobalKin*, a zero-dimensional plasma kinetics model, simulations of Ar-O_2 and Ar-N_2-O_2 discharges where the model predicted concentration of O_2^- several orders (about four) of magnitude smaller than concentrations of O^- in the discharge. Furthermore, simulations also predicted lower concentrations (one to two orders of magnitude) of vibrationally excited O_2 in Ar-O_2 discharges than concentrations of vibrationally excited N_2 in Ar-N_2 discharges simulated under similar conditions (gas pressure, concentration of

the molecular gas, flow rate, and total absorbed power). This significant difference in the concentrations of vibrationally excited nitrogen and oxygen was also observed in simulations of Ar-N_2-O_2 discharges containing the same nitrogen and oxygen concentrations. More details on the *GlobalKin* simulations and the input parameters used in this investigation are provided in Sect. 5.3.

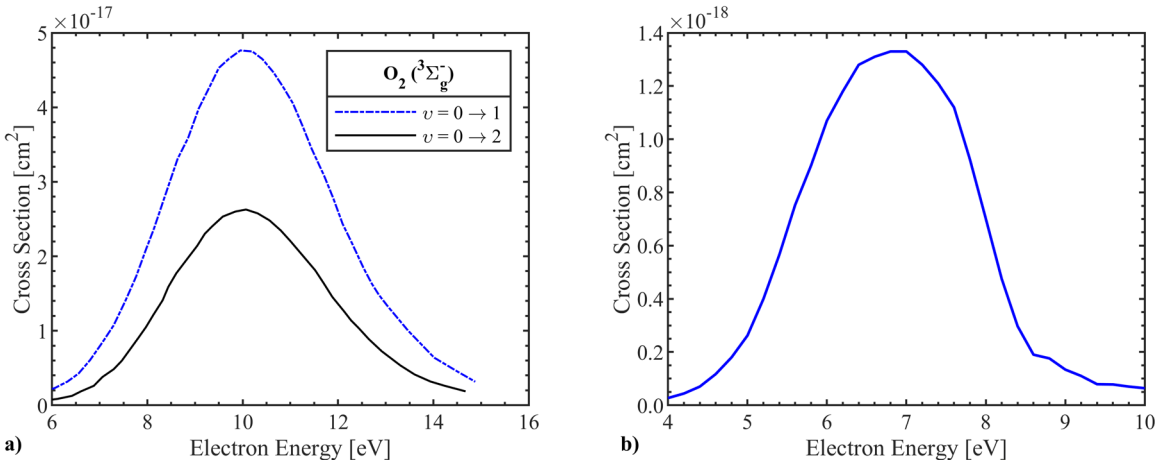

Figure 4.10: Cross sections for **a)** vibrational excitation and **b)** dissociative electron attachment of $O_2(^3\Sigma_g^-)$ via electron impact collisions. Vibrational excitation cross sections were digitized from Laporta *et al.*[99] Electron attachment cross sections were digitized from data provided by Asundi *et al.*[106]

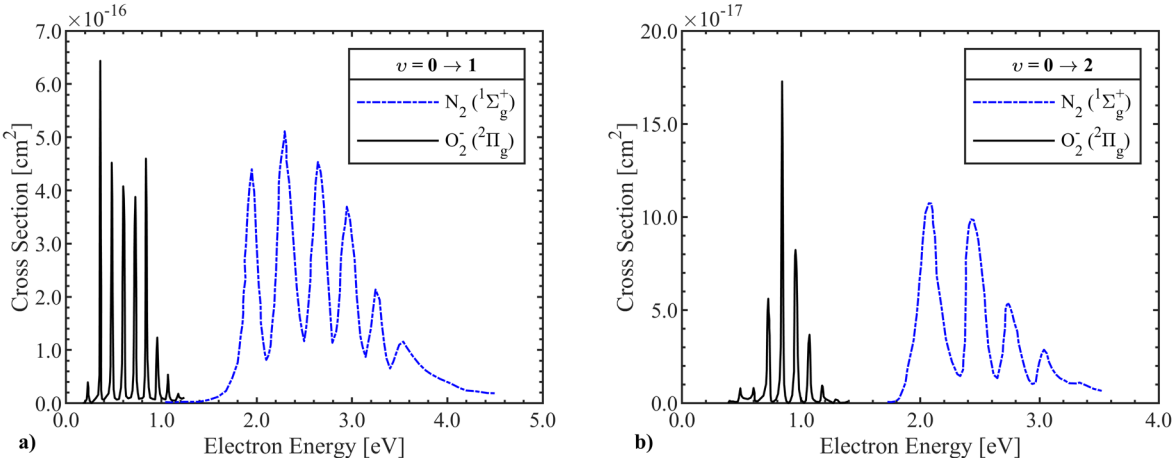

Figure 4.11: Vibrational excitation cross sections for $N_2(^1\Sigma_g^+,\ \upsilon = 0)$ and $O_2^-(^2\Pi_g, \upsilon = 0)$ transitioning into their **a)** $\upsilon = 1$ and **b)** $\upsilon = 2$ vibrational states via electron impact collisions. Cross sections for $N_2(^1\Sigma_g^+,\ \upsilon = 1)$ and $N_2(^1\Sigma_g^+,\ \upsilon = 2)$ were obtained from Itikawa and Schulz, respectively.[103], [104] Cross sections for $O_2^-(^2\Pi_g, \upsilon = 1)$ and $O_2^-(^2\Pi_g, \upsilon = 2)$ were obtained from Laporta.[99]

The other noticeable difference between the Ar-N_2 and Ar-O_2 stable discharges was that Ar-O_2 discharges appeared to be dimmer in the fast frame rate cameras than Ar-N_2 discharges. This can be attributed to the fact that oxygen is an electronegative gas that tends to capture electrons via dissociative electron attachment and direct electron attachment. This results in a decrease in the electron density, which means there are less electrons to electronically excite the atoms and molecules emitting the photons in the visible spectrum; changes in the plasma parameters as a result of changes in the gas composition are discussed in Chapter V.

Another possible factor that could be contributing to the dimmer discharge when compared to Ar-N_2 discharges is the lack of allowed electronic transitions in the visible spectrum from excited molecular oxygen; the strongest emissions come from the Schumman-Runge system ($B^3\Sigma_u^- \rightarrow X^3\Sigma_g^-$) that emits in the 175 nm to 535 nm wavelength range.[107] The first negative system of O_2^+ ($b^4\Sigma_g^- \rightarrow a^4\Pi_{ui}$) also emits in the visible spectrum (499-853 nm), but none of its bands were observed in the optical emission spectroscopy measurements; the only sign of oxygen in the spectra came from excited atomic oxygen. Images captured with the fast frame rate camera (15 ms exposure) of Ar-N_2 and Ar-O_2 stable discharges generated by a 9.5 kW microwave beam at 200 mTorr are shown in Fig. 4.12. The fast frame rate camera used to capture the images has a quantum efficiency above 10% for wavelengths in the 380 nm to 800 nm range.

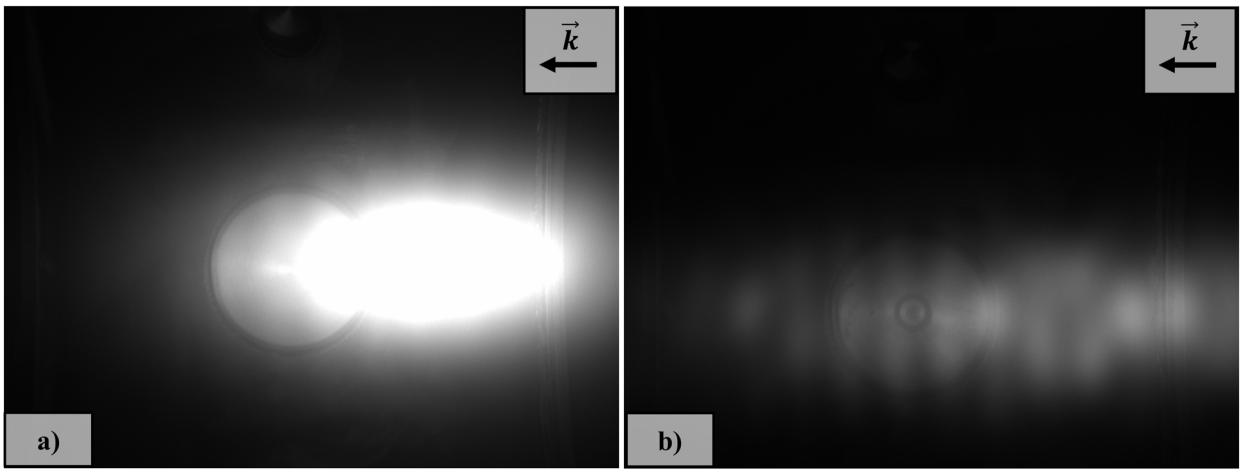

Figure 4.12: Images of **a)** Ar-N_2 and **b)** Ar-O_2 discharges captured by a fast frame rate camera (15 ms exposure). The discharges were generated with a 9.5 kW microwave beam at 200 mTorr and were approximately 45-60 cm in length and 20-30 cm in diameter. The gain was kept the same for both images.

The dimness of the Ar-O_2 discharge is also noticeable at the lower limits of the beam power required to sustain the discharge, where the plasma can become so dim that is difficult to see with the fast frame rate camera without increasing the exposure time or the gain. As the concentration of oxygen increases, the brightness of the discharge decreases at the lowest sustainable beam; this decrease in brightness can be seen in the images shown in Fig. 4.13. This behavior was also observed in Ar-N_2 discharges, but with the main difference being that Ar-N_2 discharges are brighter at the minimum sustainable beam power. For comparison purposes, images captured of Ar-N_2 discharges generated at minimum microwave beam powers are shown in Fig. 4.14; the images were captured using the same exposure time and gain as the images in Fig. 4.13.

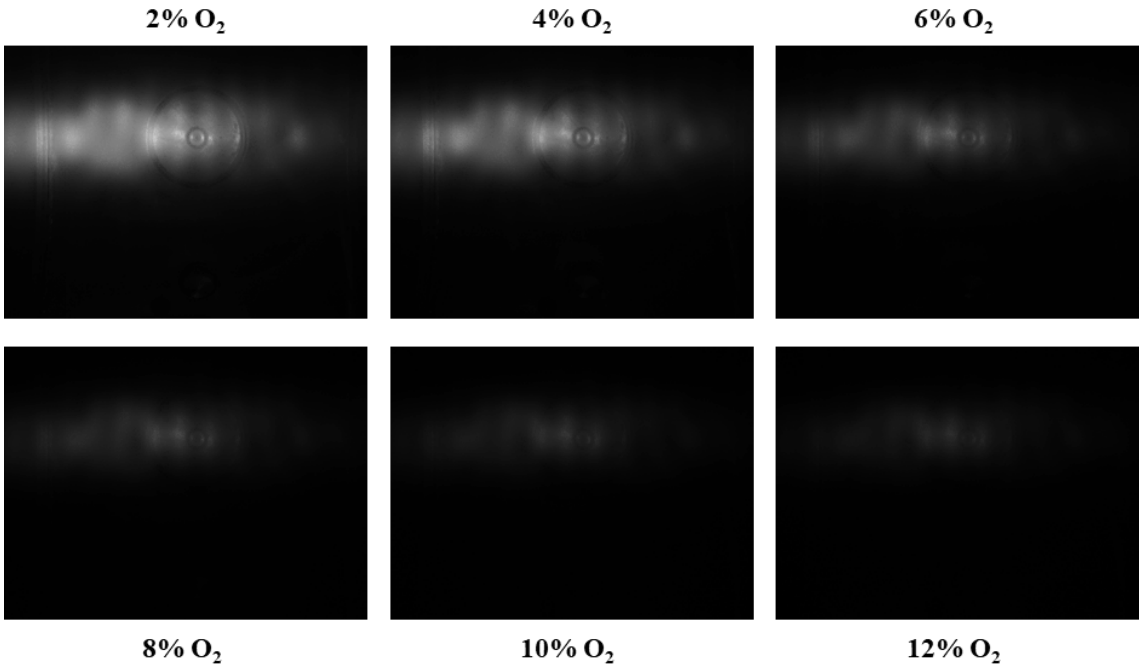

Figure 4.13: Images of Ar-O_2 discharges captured by a fast frame rate camera (15 ms exposure time). The discharges were generated at the minimum beam power required to sustain the discharge for various concentrations of oxygen at 150 mTorr and were approximately 45-60 cm in length and 20-30 cm in diameter.

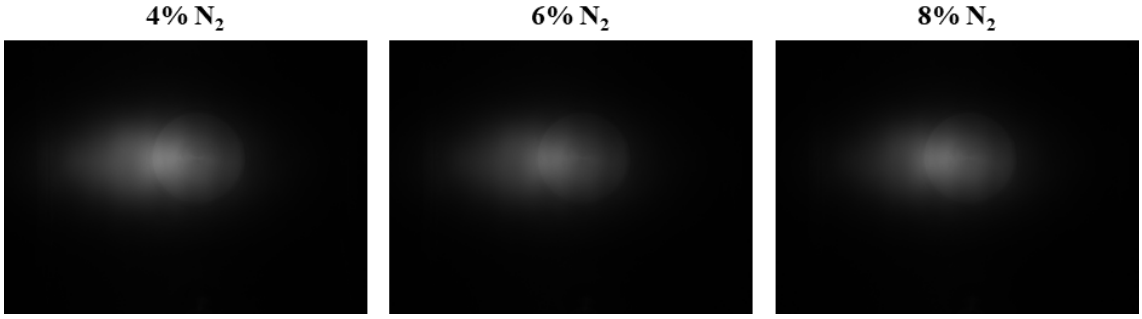

Figure 4.14: Images of Ar-N_2 discharges captured by a fast frame rate camera (15 ms exposure time). The discharges were generated at the minimum beam power required to sustain the discharge for various concentrations of nitrogen at 150 mTorr and were approximately 45 in length and 25 cm in diameter.

The parameter (beam power and molecular gas concentration) ranges for which stable discharges were obtained in Ar-O_2 gas mixtures was larger than that of Ar-N_2 gas mixtures. The molecular gas concentration that could be added to the argon discharge before becoming unsustainable at the available beam power increased from 10% when using nitrogen to 22% when using oxygen. This difference is likely due to the differences in electron-impact vibrational excitation cross sections between the molecular nitrogen and oxygen where nitrogen's vibrational

levels quenches the energy of the electrons significantly more than oxygen's vibrational levels. There increase in range of power of the microwave beam was mostly noticeable at the lower concentrations of added oxygen, where the beam power could be maxed out or closed to (for 2% O_2) without inducing the quasi-stable discharge. This could be due an increase in the vibrational temperature due to electrons transferring energy to nitrogen's vibrational levels and as the power of the beam increases the electron density also increases leading to more electrons dumping energy to the vibrational levels. Note that the electron density of Ar-N_2 discharges measured by the probe were on the order of 10^{16} m^{-3}, which was far from approaching the critical density of approximately 2.7×10^{17} m^{-3}. This suggests that some sort of instability could be causing the electron density to quickly rise (in less than a 500 W input power increase) leading the stable discharge to transition into its quasi-stable mode. This rapid rise in electron density could occur if there was a disturbance in the vibrational temperature that feeds on an increase in the electron density and gas temperature according to Nighan and his description of thermal instabilities; this feedback process is shown in Fig. 4.3.[95]

As in Ar-N_2 discharges, the triple probe affects the range of the beam power and oxygen concentration at which stable discharges can be obtained. These differences in the parameter boundaries can be seen from the results listed in Table 4.3 and Table 4.4. A diagram of the stability state of the Ar-O_2 discharge under various gas pressures, oxygen concentrations, and beam power combinations is shown in Fig. 4.15.

Table 4.3: Microwave beam power range in which Ar-O_2 stable discharges generated for triple probe experiments can be obtained for multiple gas pressures and concentrations of O_2.

O_2 [%]	200 mTorr		175 mTorr		150 mTorr	
	Min [kW]	Max [kW]	Min [kW]	Max [kW]	Min [kW]	Max [kW]
2	7.5	9.5	7.5	9.5	8.0	9.5
4	8.0	9.5	8.5	9.5	9.5	9.5
6	8.5	9.5	9.0	9.5	—	—
8	8.5	9.5	9.0	9.5	—	—
10	9.0	9.5	9.5	9.5	—	—
12	9.0	9.5	9.5	9.5	—	—
14	9.5	9.5	—	—	—	—
16	9.5	9.5	—	—	—	—

Table 4.4: Microwave beam power range in which Ar-O_2 stable discharges generated for optical emission spectroscopy experiments can be obtained for multiple gas pressures and concentrations of O_2.

O_2 [%]	200 mTorr		175 mTorr		150 mTorr	
	Min [kW]	Max [kW]	Min [kW]	Max [kW]	Min [kW]	Max [kW]
2	4.5	8.0	5.0	8.0	5.5	9.0
4	5.5	9.5	6.0	9.0	7.0	9.5
6	7.0	9.5	7.0	9.5	7.5	9.5
8	7.0	9.5	7.0	9.5	8.0	9.5
10	7.5	9.5	7.5	9.5	8.5	9.5
12	8.0	9.5	8.0	9.5	9.0	9.5
14	8.5	9.5	8.0	9.5	9.5	9.5
16	9.0	9.5	9.0	9.5	—	—
18	9.0	9.5	9.5	9.5	—	—
20	9.5	9.5	9.5	9.5	—	—
22	9.5	9.5	—	—	—	—

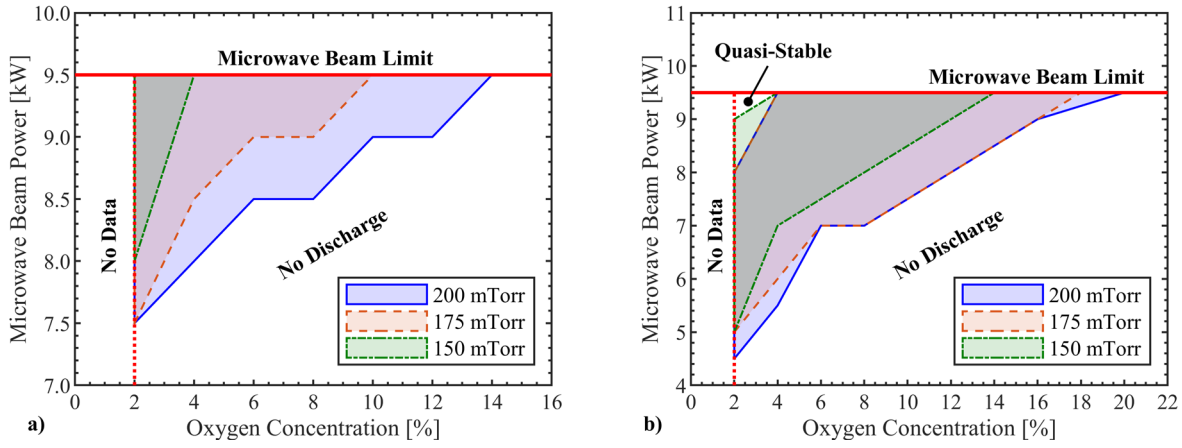

Figure 4.15: Stability of Ar-O_2 plasma discharges under various operating conditions for **a)** triple probe and **b)** optical emission spectroscopy experiments. The shaded regions represent the combination of parameters (beam power, nitrogen concentration, and gas pressure) that yield stable discharges. Regions above and below the boundary line of the stable discharge region yield quasi-

stable discharges and no discharges, respectively. Note that there is insufficient or no data to determine stability boundaries for oxygen concentrations below 2%. The microwave beam limit was set by the operating limits of the power supply.

4.3.3 Ar-N_2-O_2 Gas Mixtures

When all three gases are mixed, the structure of the discharge looks similar to that of an Ar-O_2 discharge but significantly brighter due to the rovibrational bands of nitrogen. The presence of nitrogen in the gas mixture appeared to dominate the reactions in the discharge given that the discharge was unsustainable when the gas mixture had more than a 12% molecular gas concentration. This value is closer to the maximum molecular gas concentration tested in Ar-N_2 discharges than Ar-O_2 discharges. Furthermore, more oxygen than nitrogen could be added to gas mixture before the discharge could no longer be sustained at 9.5 kW. When the concentration of nitrogen was kept at 2%, up to 10% oxygen could be added to the discharge before it became unsustainable. On the other hand, when the concentration of oxygen was kept at 2%, only 6% nitrogen could be added to the discharge before it decayed. The gas mixtures of Ar-N_2-O_2 tested for this investigation are listed in Tables 4.5 and 4.6.

Table 4.5: Microwave beam power range in which Ar-N_2-O_2 stable discharges generated for triple probe experiments can be obtained for multiple gas pressures and concentrations of N_2 and O_2.

N_2 [%]	O_2 [%]	200 mTorr		175 mTorr		150 mTorr	
		Min [kW]	Max [kW]	Min [kW]	Max [kW]	Min [kW]	Max [kW]
2	2	6.5	9.5	7.0	9.5	8.0	9.5
2	4	7.5	9.5	8.0	9.5	9.0	9.5
2	6	8.5	9.5	9.0	9.5	—	—
2	8	8.5	9.5	—	—	—	—
2	10	9.0	9.5	—	—	—	—
4	2	7.5	9.5	8.0	9.5	9.0	9.5
4	4	8.5	9.5	9.0	9.5	—	—
4	6	9.0	9.5	—	—	—	—
6	2	8.5	9.5	9.5	9.5	—	—

Table 4.6: Microwave beam power range in which Ar-N_2-O_2 stable discharges generated for optical emission spectroscopy experiments can be obtained for multiple gas pressures and concentrations of N_2 and O_2.

N_2 [%]	O_2 [%]	200 mTorr		175 mTorr		150 mTorr	
		Min [kW]	Max [kW]	Min [kW]	Max [kW]	Min [kW]	Max [kW]
2	2	5.5	9.5	6.0	9.5	7.0	9.5
2	4	6.5	9.5	7.0	9.5	7.5	9.5
2	6	7.5	9.5	8.0	9.5	8.5	9.5
2	8	8.0	9.5	8.5	9.5	—	—
2	10	8.0	9.5	—	—	—	—
4	2	6.0	9.5	7.0	9.5	8.0	9.5
4	4	7.5	9.5	8.0	9.5	—	—
4	6	8.0	9.5	8.5	9.5	—	—
6	2	7.0	9.5	8.0	9.5	—	—
6	4	8.0	9.5	—	—	—	—

In general, discharges produced with a mix of all three gases followed the same trends as the Ar-N_2 and Ar-O_2 discharges. As the concentration of argon in the gas mixture was replaced with molecular gases, the more power that was needed to sustain the discharge. Gas pressure also affects the power requirements to sustain stable discharges. As the gas pressure decreases, diffusion increases which means the electron temperature must increase for the ionization rate to keep up with the losses of the discharge; to increase the electron temperature, the discharge must absorb more power which means the beam power must also increase. The effects of triple probe perturbations on discharges were also observed in the lower limits of the beam power needed to sustain the discharge. The operational conditions for which stable discharges can be obtained in Ar-N_2-O_2 gas mixtures are shown in Figs. 4.16 and 4.17. Note that diagrams are for gas mixtures where the concentration of nitrogen is kept constant at 2% and 4% in Figs. 4.16 and 4.17, respectively.

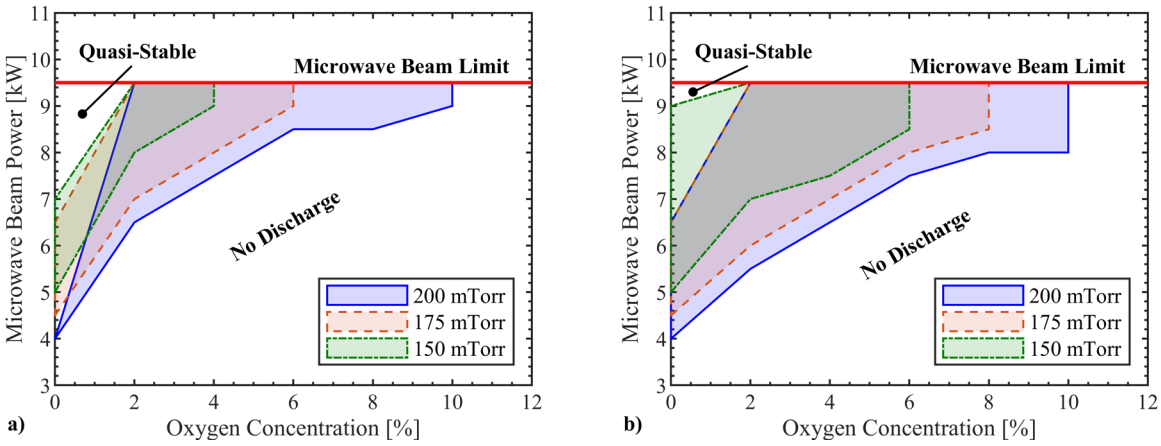

Figure 4.16: Stability of Ar-N_2-O_2 plasma discharges under various operating conditions for **a)** triple probe and **b)** optical emission spectroscopy experiments. Here the concentration of nitrogen was kept at 2%. The shaded regions represent the combination of parameters (beam power, nitrogen concentration, and gas pressure) that yield stable discharges. Regions above and below the boundary line of the stable discharge region yield quasi-stable discharges and no discharges, respectively. The microwave beam limit was set by the operating limits of the power supply.

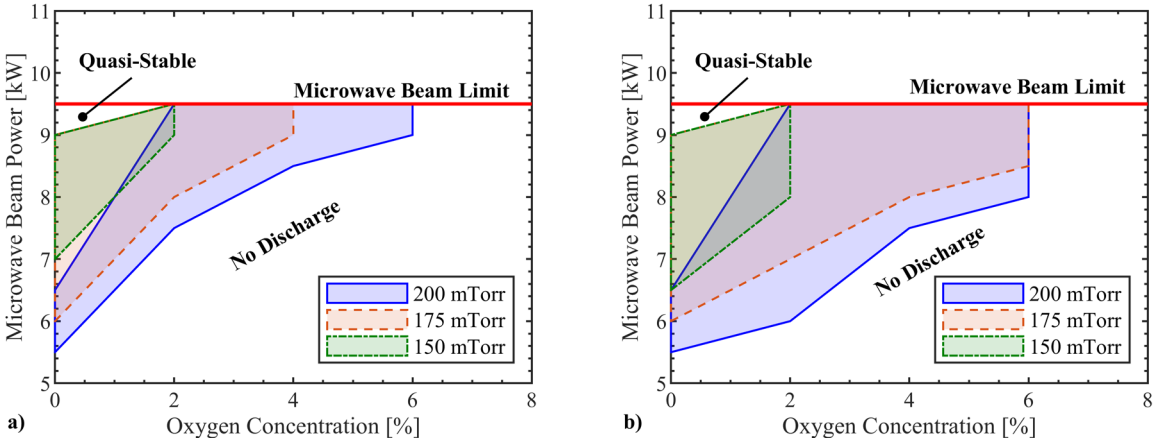

Figure 4.17: Stability of Ar-N_2-O_2 plasma discharges under various operating conditions for **a)** triple probe and **b)** optical emission spectroscopy experiments. Here the concentration of nitrogen was kept at 4%. The shaded regions represent the combination of parameters (beam power, nitrogen concentration, and gas pressure) that yield stable discharges. Regions above and below the boundary line of the stable discharge region yield quasi-stable discharges and no discharges, respectively. The microwave beam limit was set by the operating limits of the power supply.

4.4 Closing Comments

Stability of the discharges generated in the AFRL's experimental setup proved to be controllable by adjustments to the gas composition, power of the microwave beam, and gas flow rate. Unstable discharges were only observed in pure argon discharges and could be transitioned into quasi-stable discharges by increasing the flow rate of the gas or increasing the power of the

microwave beam. Studies on the quasi-stable discharges found that the temporal oscillations in brightness and size reported by Hoff *et al*. to describe the quasi-stable discharges was actually periodic ionization fronts propagation upstream towards the microwave source at 10s of Hertz. The ionization fronts observed in quasi-stable discharges were similar to those reported in the literature of pulse microwave discharges, with the main difference being the periodicity of the ionization fronts that came with using a CW microwave source.

Towards the beginning of this investigation it was thought that the quasi-stable discharges were just a result gradually reaching the critical density (approximately 2.7×10^{17} m^{-3}); however, it was later realized that the electron density measured at the last condition before the discharge would go quasi-stable was about an order of magnitude away from the critical density. This meant that the electron density was increasing rapidly near its transition from stable to quasi-stable. For example, the average increase in the peak electron density of a Ar-N_2 (4% N_2) discharge was approximately 25% for every 500 W the power of the beam was increased, so assuming the critical density was reached right before the discharge went quasi-stable would mean the electron density has to increase by approximately 2500% in less than a 500 W increase in beam power. While it is unclear what is causing this rapid increase in the electron density, thermal instabilities are currently being considered as a possible source of the instability.[71], [94], [95]

Quasi-stable discharges in this investigation were transitioned to stable discharge by increasing the concentration of the molecular gas, decreasing the power of the microwave beam, or decreasing the gas pressure. Three different gas mixtures were tested with all showing similar stability trends as the control parameters were varied; stability zones were established for most of the operational conditions that could produce discharges in the AFRL's experimental setup. In general, discharges became more difficult to sustain at max power as gas pressure decreased and

concentration of the molecular gas increased. It was also determined that nitrogen quenched the discharges significantly faster than oxygen; only 10% nitrogen (compared to 22% oxygen) could be added the gas mixture before the discharge could no longer be sustained in the 9.5 kW beam at 200 mTorr. The main differences in the behavior observed between Ar-N_2 and Ar-O_2 discharges could be attributed the properties of each of the molecular gases; nitrogen easily quenched the energy of electrons through its vibrational states, while oxygen would capture the electrons through dissociative electron attachment and direct electron attachment.

Chapter V

Characterization of Striated Microwave Discharges

5.1 Striations

Striations have been observed in plasmas since the mid-18th century, with Abria first reporting on the alternating bright and dark regions of DC glow discharges.[108] While striations have been studied extensively in DC and RF discharges, they are still not well understood due to their diverse behavior and properties.[108]–[125] In general, striations consist of periodic spatial modulations of the electron density and temperature that often are attributed to ionization instabilities. However, the operational conditions (e.g. gas pressure and input power) for which these instabilities are triggered vary significantly between gases, plasma sources, and discharge vessel geometry. Such variations observed in rare gases, with variation in chamber geometry are discussed by Kolobov, and Ghomi *et al*., respectively.[114], [118] While the majority of the studies on striations have been performed in experimental setups where the discharge is bounded by electrodes or the chamber walls, striations have also been observed in free space discharges.[113], [126], [127] One of the characteristics that free space discharges have in common with surface bounded discharges was that the periodic spatial modulation of the electron density and temperature were out of phase; when the electron density increased, the electron temperature decreased.[113], [114], [117]

5.1.1 Striated Microwave Discharges

Striated microwave discharges generated at the AFRL's experimental setup exhibited similar behavior and characteristics as those reported in literature. In the reported DC and RF glow discharges, the striation pattern usually remained unchanged through the length of the discharge tube for a given set of conditions, while in the AFRL's experimental setup up to three different striation patterns have been observed simultaneously along the length of the discharge. A bright round pattern (pattern #1) has been observed towards the leading end of the discharge, which then transitions into a striped pattern (pattern #2). A third pattern (pattern #3) begins to develop towards the trailing end of the discharge that resembles a combination of patterns 1 and 2. It is unclear what causes the striation pattern to change through the length of the microwave discharge, but recent simulations conducted by Reid suggest that the angles (relative to the axis of the discharge) in which the microwave beam interacts with the leading end of the plasma might affect the appearance of the striation pattern near the leading end of the plasma; experiments to study the origins of the different striation patterns in more detail are planned for the future.[128] Images of an RF glow discharge and a microwave discharge (AFRL's setup) are shown in Fig. 5.1 to illustrate the difference in complexity of the observed striation patterns.

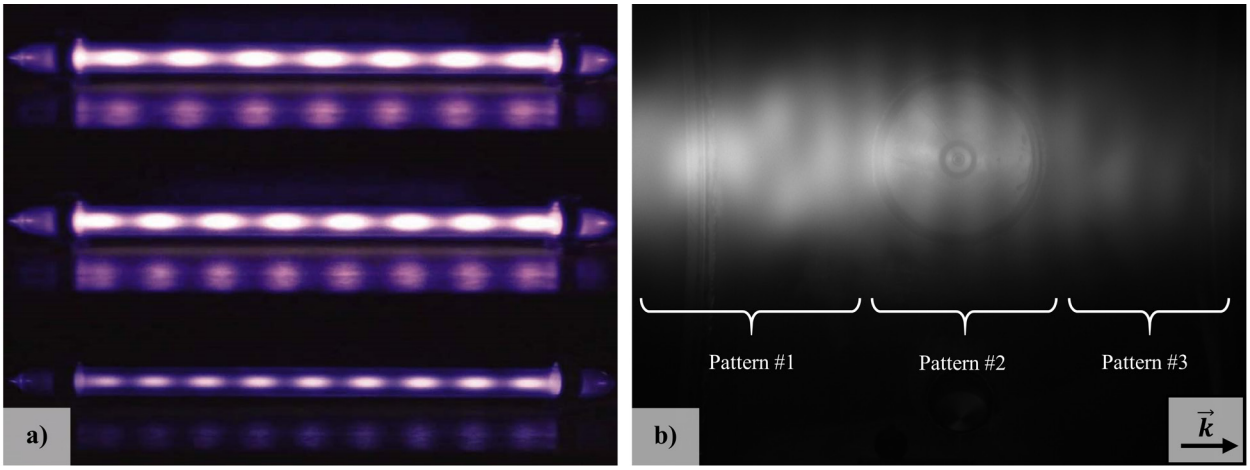

Figure 5.1: Images of an **a)** RF glow discharge (Mulders *et al*. setup) and a **b)** discharge generated at the focus of a microwave beam (AFRL's setup). The frequency of the RF discharges were (top to bottom) 70, 29, and 6 MHz resulting in 8, 9, and 10 total visible striations contained in a 30 cm long by 2.5 cm diameter discharge vessel .[115] The microwave discharge shows three different patterns for Ar-O_2 (4% O_2) plasma generated by a 9.5 kW microwave beam at 200 mTorr. The discharge was approximately 60 cm in length and 25 cm in diameter.

While the striation patterns observed in the AFRL's setup could be perceived as more complex than those commonly observed in DC and RF discharges, they exhibit similar trends as those of DC and RF discharges. For example, the separation between striations is approximately constant throughout the discharge, including through the different patterns. Processing the images of the striated discharges to display them as a colormap of the relative intensity captured by the cameras makes it easier to observe the striations and helps identify the regions emitting more light. Note that brighter regions suggest that there is a higher concentration of electrons that can electronically excite atoms and molecules in those regions resulting in an increase of photons emitted in the visible spectrum; an increase in electron temperature could also be contributing to brighter regions due to an increase in excitation rate. A colormap of an Ar-O_2 (2% O_2) discharge generated with a 6.5 kW microwave beam at 200 mTorr is shown in Fig. 5.2.

Taking the average intensity emitted over every column of pixels in the image captured provides insight into the distance in between striations by using a known distance as reference for converting pixels into distances. In this case an alumina tubing that had an outer diameter of 6.35

mm was used as reference for the frame resulting in a conversion of approximately 0.668 mm per pixel. Using this method, the average separation measured between striations (from center to center) was 50 pixels which converts to approximately 3.34 cm; this distance is a little over half a wavelength of the microwave beam providing some insight into the possible mechanism responsible for the formation of striations in the discharge. The average distance between striations measured from an image of the discharge is shown in Fig. 5.2. This process was repeated for discharges generated under different conditions (gas pressure, beam power, and gas compositions) and the results were almost identical to within 1 pixel or approximately 0.668 mm.

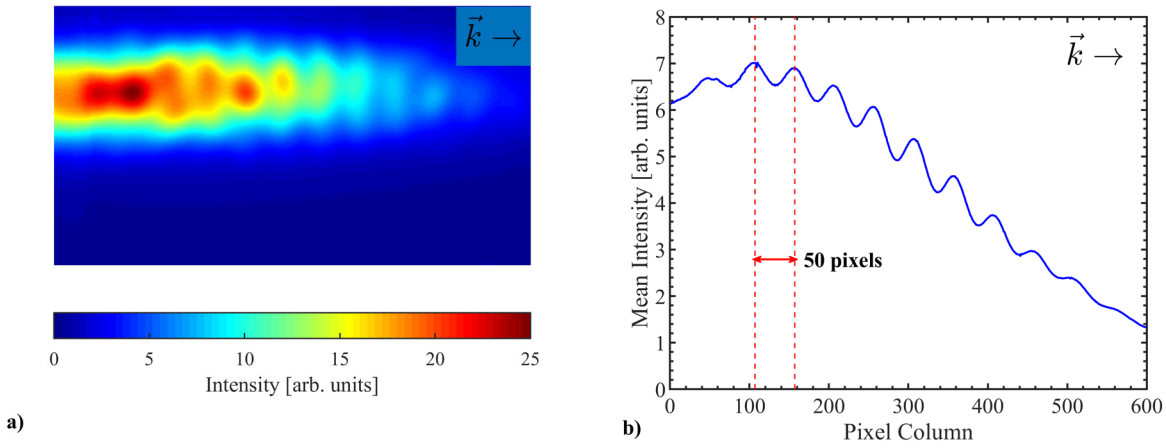

Figure 5.2: a) Colormap of the intensity of striations observed in an Ar-O_2 (2% O_2) discharge generated by a 6.5 kW microwave beam at 200 mTorr. **b)** The mean of the intensities in each column of pixels show the periodic spatial modulation of the intensity of the discharge associated with striations. On average the measured distance between striations is approximately 3.34 cm; each pixel represents approximately 0.668 mm in this camera frame.

Periodic spatial oscillations of the electron density and temperature were also observed in the experiments conducted with triple probes at the AFRL; these periodic spatial oscillations are shown in Fig. 5.3. While the spacing between striations was relatively constant when measured through images of the discharge, the same could not be said when the spacing between spatial oscillations of the electron temperature and density was measured. For most of the tested conditions the separation between local maximums of the electron temperature and density ranged from approximately 3.2 cm to 4.1 cm. This significant range in the spacing between local

maximums could be a result of the triple probe measurements taken along the path of three different striations patterns; the path of triple probe is shown in Fig. 5.4. In general, the spacing between the local maximums increases near the edges of the discharge and remains constant near the center of the discharge. This behavior seems to agree with what the triple probe would see as it traveled through the three different striations patterns assuming a correlation between the bright regions and the electron density as reported in literature; note that as the probe transitions from pattern #1 to pattern #2, the probe would see longer dark and bright regions.[114], [117], [120] While the exact source of the striation patterns observed remains unclear, results analyzed to date suggest standing waves within the discharge might be responsible for the striations.

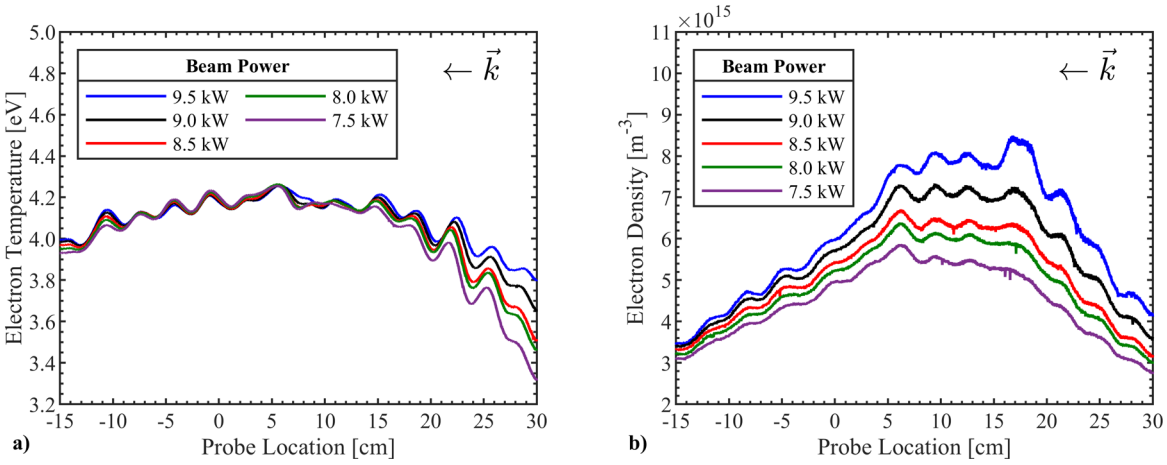

Figure 5.3: Spatially resolved electron **a)** temperature and **b)** density measurements of stable Ar-O_2 (2% O_2) plasma generated at 200 mTorr with various input microwave beam powers. The probe location is relative to the beam's geometric focus (in vacuum).

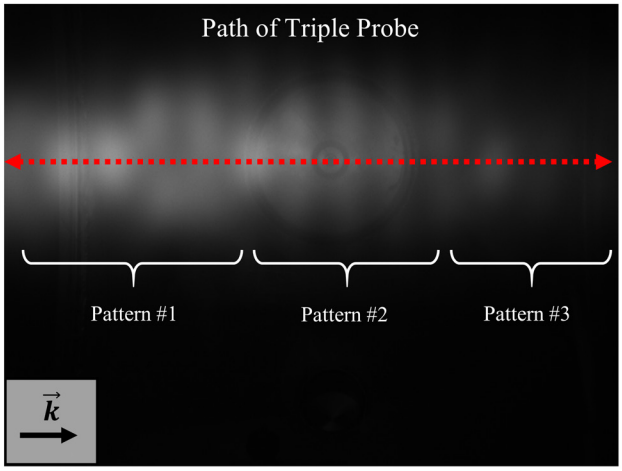

Figure 5.4: Approximate path traveled by the triple probe (dotted red line).

Studies that measured the electron temperature and density of striations patterns reported observing an anticorrelation of the electron temperature and density attributed to disturbances on the electron density caused by local heating of the gas.[113], [114], [126], [129] A similar anticorrelation behavior was observed in the triple probe measurements of the microwave discharges generated at the AFRL. However, this behavior was only evident in the center region of the discharge (pattern #2); sample measurements of the electron temperature and density in this region is shown in Fig. 5.5. It is unclear why the anticorrelation is only evident in a specific region of the discharge, but this behavior could also be associated with the change in the striation pattern as the probe travels through the discharge. It can be seen from Fig. 5.4 that the width of the bright and dark regions along the path of the triple probe increases as the probe transitions from the center region of the discharge (pattern #2) to the leading end of the discharge (pattern #1). These transition regions will be studied in more detail in the future after the translation stage is upgraded for multi-axis capabilities.

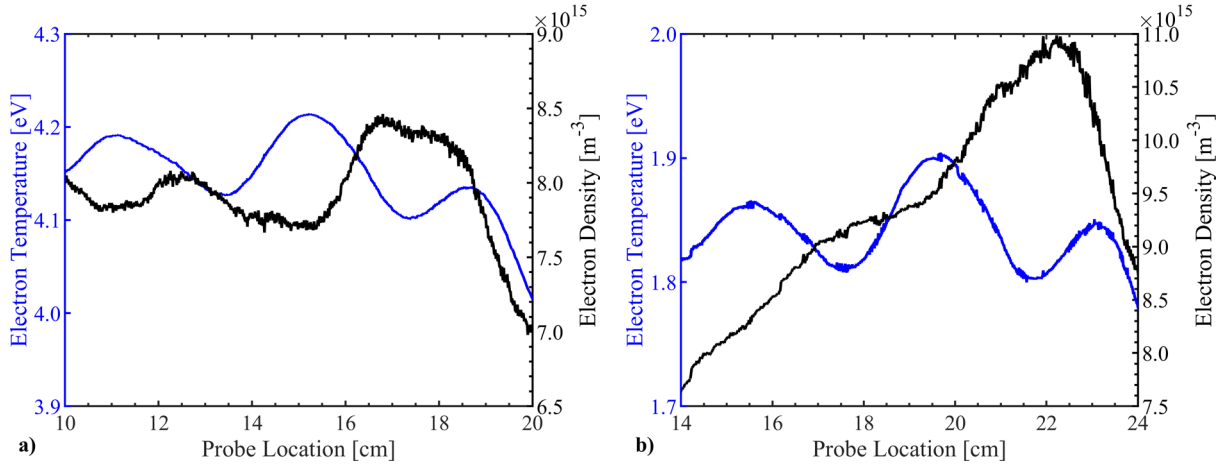

Figure 5.5: Anticorrelation of the electron temperature and density in **a)** Ar-O_2 (2% O_2) and **b)** Ar-N_2 (4% N_2) microwave discharges. Tripe probe measurements shown were made within the region corresponding to where pattern #2 was observed. The probe location is relative to the microwave beam's geometric focus in vacuum conditions.

5.2 Experimental Measurements of the Plasma Parameters

Invasive and non-invasive plasma diagnostic methods were used to characterize the striated stable discharges generated at the AFRL; a triple probe system was used for measurements of the electron temperature and density, and an optical emission spectroscopy system was used for measurements of the electron temperature and gas temperature. Studies of Ar-N_2 discharges were conducted at gas pressures ranging from 100 mTorr to 200 mTorr for concentrations of nitrogen ranging from 2% to 10%. For Ar-O_2 and Ar-N_2-O_2 discharges the tested gas pressures ranged from 150 mTorr to 200 mTorr; reasons for this reduction in the gas pressure range is discussed in Sect. 4.3. In Ar-O_2 discharges the concentration of oxygen ranged from 2% to 22%, while in Ar-N_2-O_2 discharges the oxygen content was limited to 10% before the discharge could no longer be sustained; the concentration of nitrogen was limited to 6% in Ar-N_2-O_2 as discussed in Sect. 4.3. The ranges of microwave beam powers for each tested gas pressure and composition combination can be found in Sect. 4.3.

The total flow rate of the gas mixtures was kept at 350 sccm for all tested conditions and discharges were given a minimum of five minutes to reach steady state before making

measurements. This minimum stabilization time was determined from monitoring the signal of the triple probe as 7 sccm of nitrogen (2% by concentration) were added to the gas mixture of a pure argon discharge; the steady state of the plasma was defined as the point where the voltage potential between the reference and positive wires of the probe changed by less than 0.05 V in a minute. While the stabilization times are shorter (approximately two minutes) for plasmas already containing 2% of a molecular gas, five minutes stabilization times were used for all tested conditions to ensure steady state was reached before measurements were made and for consistency of the experimental procedure. All measurements made with the triple probe use the geometric focus of the microwave beam in vacuum conditions as a reference point for the location of the probe, and all optical emission spectroscopy measurements were made near the center of the discharge; the relative location of the experimental measurements for both diagnostic methods used in this investigation are shown in Fig. 5.6.

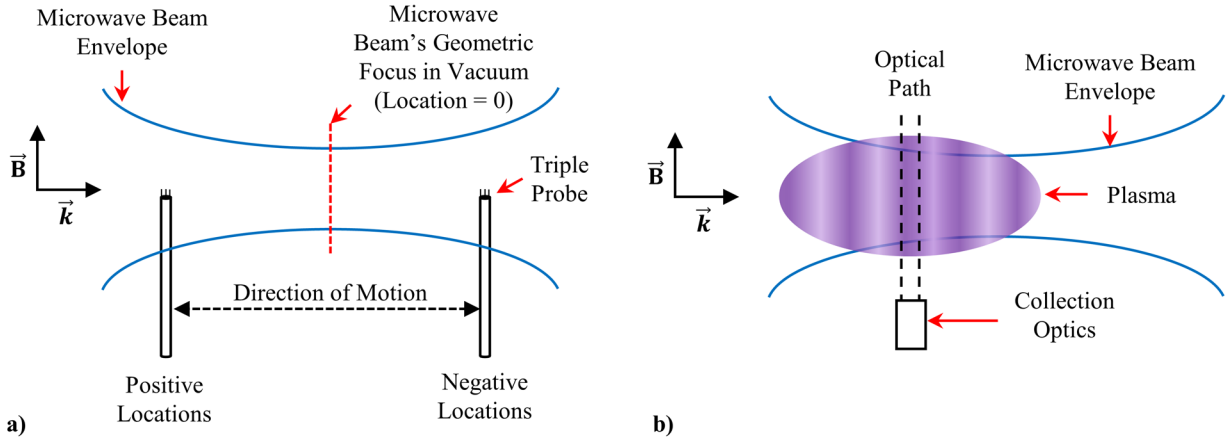

Figure 5.6: References for experimental measurement plots. **a)** The triple probe location used the microwave beam's geometric focus in vacuum conditions (dotted red line) as a reference point (location = 0). The path of the probe is along the microwave propagation vector, $\vec{k}$, with positive and negative values of the probe location indicating regions upstream and downstream of the beam's geometric focus, respectively. **b)** All optical emission spectroscopy measurements reported in this investigation were made near the center of the discharge

5.2.1 Effects of Changes in Microwave Beam Power

Triple probe measurements of the electron temperature and density of Ar-N_2 discharges showed similar trends in all tested pressures (100 mTorr, 150 mTorr, and 200 mTorr). When the microwave beam power was increased at a fixed gas pressure and composition, a slight increase in the electron temperature and a noticeable increase in the electron density were measured. The increase in the electron temperature was expected as the stronger the electric field the more energy free electrons can transfer to the plasma via collisions; the electric field of the microwave beam is proportional to the square root of the beam power. As the gas temperature increases, the neutral gas density decreases (at constant gas pressure), which would also contribute to the increase in electron temperature. However, as the electron temperature increases the diffusion rate also increases, causing an expansion of the discharge volume that helps balance the energy gains; assuming the diffusion mechanism is dominated by ambipolar diffusion, the relationship between the ambipolar diffusion coefficient (D_a) and the electron temperature for a weakly ionized discharge is given by

$$D_a \approx \mu_i T_e \ , \tag{5.1}$$

where μ_i is the ion mobility. The electron temperature is determined by the local balance between the energy gained by the electrons from the electric field and the energy lost to collisions with the gas particles and diffusion. This relation can be expressed by

$$\frac{|q_e E_z|^2 n_e \frac{\nu_c}{\omega}}{2m_e\omega[1+(\nu_c/\omega)^2]} \approx n_e N_g \kappa(T_e) \ , \tag{5.2}$$

where E_z is the local field amplitude at location z, N_g is the density of the gas particles, and κ is an energy loss coefficient dependent on the electron temperature.[130]

The increase in the electron density was also expected since an increase in the electric field is also associated with an increase in the ionization rate due to its dependency to the energy

distribution of the electrons and the cross sections for ionization of the atoms and molecules. It is also possible that the increase in the gas temperature results in an increase in the Penning ionization rate from interactions between metastable states of argon and electronically excited states of nitrogen; increases in interactions between heavy particles are usually correlated with increases in the gas temperature. An example of the changes in the electron temperature and density as a result of varying the power of the microwave beam is shown in Fig. 5.7.

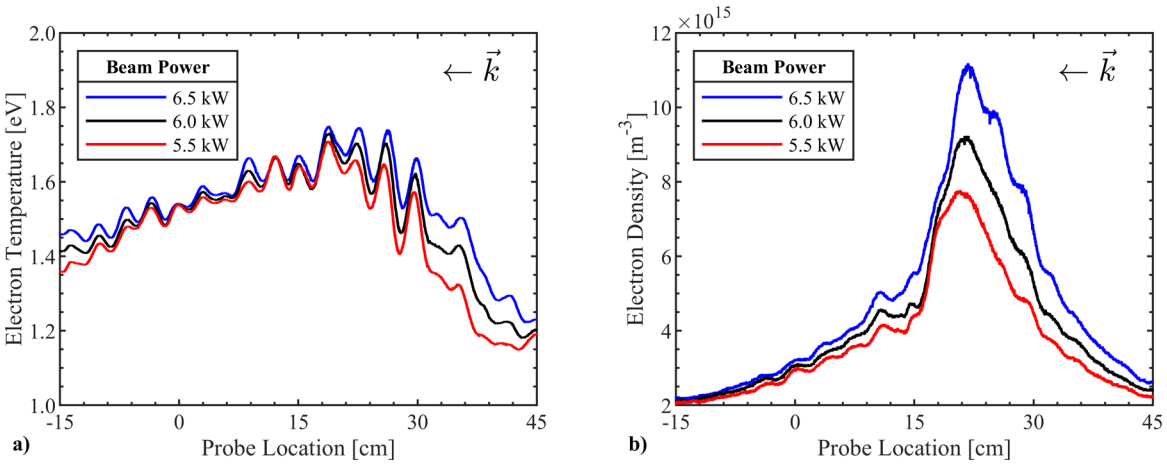

Figure 5.7: Spatially resolved electron **a)** temperature and **b)** density measurements of stable Ar-N_2 (4% N_2) plasma generated at 200 mTorr with various input microwave beam powers.

5.2.2 Effects of Changes in Gas Pressure

When the gas pressure was decreased at a fixed gas composition and beam power, it was interesting to see that the electron temperature remained relatively constant as it would be expected for the electron temperature to increase due to the drop in the neutral gas density. Perhaps the change in gas pressure between measurements was too small to make any noticeable difference in the electron temperature; again, it all comes down to the balance of energy gains and losses of the system. On the other hand, the effects of gas pressure were more noticeable in the electron density which decreased as the gas pressure decreased. The decrease in the electron density was expected because at a lower gas pressure there would be less neutral gas particles for free electrons to ionize.

The changes in the peak electron temperature and density due to changes in the gas pressure are shown in Fig. 5.8

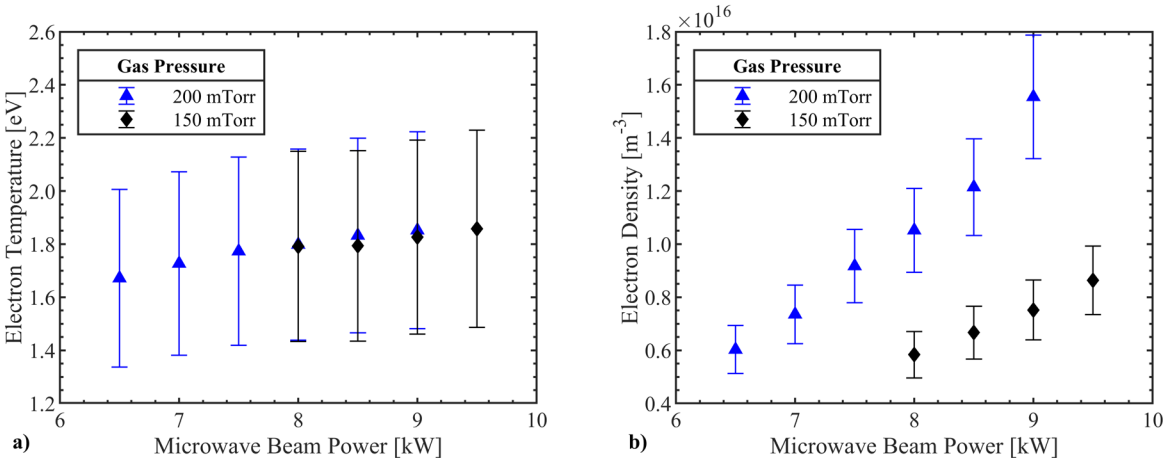

Figure 5.8: Peak electron **a)** temperature and **b)** density as a function of microwave beam power for stable Ar-N_2 (6% N_2) discharges generated at 200 mTorr and 150 mTorr.

5.2.3 Effects of Changes in Gas Composition

The last variable that was controlled in this investigation was the concentration of the molecular gases in the discharge. Probe measurements recorded a slight decrease in the peak electron temperature and a significant decrease in the peak electron density as the concentration of nitrogen in the discharge increased at a fixed microwave beam power and gas pressure. Molecular nitrogen is known to quench the energy of free electrons through its vibrational levels, as they can easily be excited at low energies levels (1.5 eV to 4.5 eV range). This quenching effect is likely responsible for the decrease in the electron temperature; simulation results that support this claim are discussed in the next section (Sect. 5.2.2). There are several factors that could be contributing to the decrease in the electron density as the concentration of nitrogen increases: increased channels for recombination, and metastable states of argon losing the excess energy to nitrogen. Molecular and atomic nitrogen ions serve as additional recombination channels, which could potentially increase electron losses to recombination. The interactions between metastable states of argon and different states of nitrogen can also contribute to the decrease in the electron density

as these interactions can decrease the density of the metastable states that are essential to the ionization of argon atoms; these interactions could also result in Penning ionization of excited nitrogen molecules. Lastly, the increase in the available vibrational levels that comes from increasing the concentration of nitrogen increases the probability of free electrons transferring energy to a vibrational state instead than to a metastable state of argon. The changes on the electron temperature and density due to increases in the nitrogen content of the discharge are shown in Fig. 5.9.

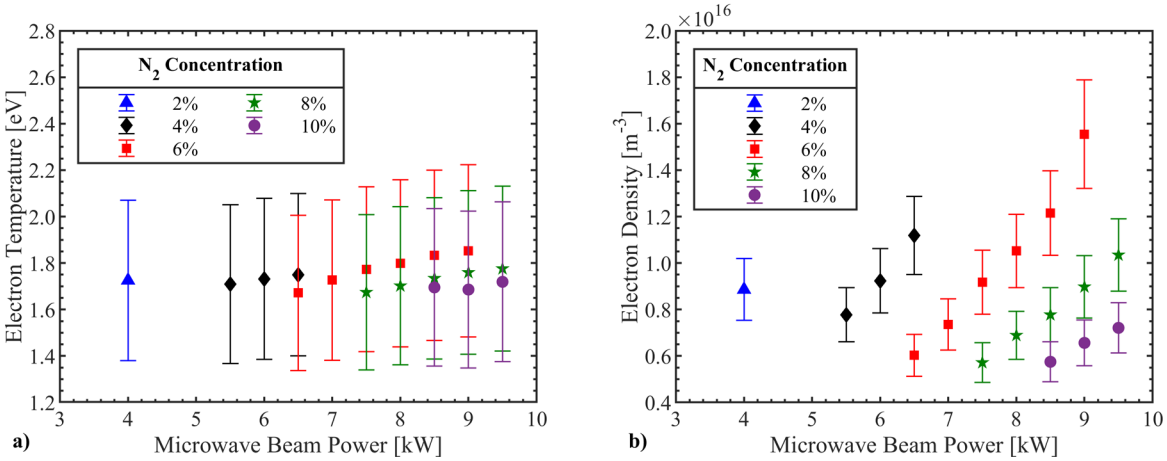

Figure 5.9: Peak electron **a)** temperature and **b)** density as a function of microwave beam power of stable Ar-N_2 discharges generated at 200 mTorr with various concentrations of N_2.

The electron temperature and density trends that were observed in Ar-N_2 discharges were also observed in discharge generated from gas mixtures of Ar-O_2 and Ar-N_2-O_2. One of the main differences between the plasma parameters of the discharges was that a significant increase in the electron temperature was measured in discharges containing oxygen; the peak electron temperatures increased by approximately 140% compared to Ar-N_2 discharges generated under similar operational conditions. While an increase in the electron temperature could be expected due to molecular oxygen not quenching the energy of the electrons as much as molecular nitrogen, it was unclear the extent of the increase in the electron temperature one could expect; note that electron collisions with oxygen are more likely to result in dissociative electron attachment than

vibrational excitation, as discussed in Sect. 4.3.2. Given that molecular oxygen is an electronegative gas that produces negative ions in a discharge, there is a chance that the presence of negative ions affected the accuracy of the triple probe measurements.

Optical emission spectroscopy measurements and simulations also calculated higher electron temperatures in Ar-O_2 discharges than in Ar-N_2 discharges, but significantly lower than those measured by the probe; optical emission spectroscopy measurements are discussed later in this section and simulation results are discussed in the next section. Unfortunately, the triple probe method used for this investigation does not address corrections needed to account for the presence of negative ions in the discharge. Furthermore, given that the floating triple probe method operates in the ion saturation region of the current-voltage characteristic curve, it is likely that negative ion current was not collected by the probe as negative ions would not have enough energy to overcome the repulsive potential of the probe. It is unclear what are the sources and the extent of the inaccuracies in triple probe measurements of discharges containing oxygen, but it is likely that its related to the presence of negative ions; further research is needed to better understand how the presence of negative ions affect triple probe measurements and ways to correct for the effects (if possible).

A decrease in the peak electron density was also measured in discharges containing oxygen; on average the decrease in the peak electron density was approximately 80% when compared to Ar-N_2 discharges generated under similar operational conditions. The decrease in the electron density would also be expected given that molecular oxygen is known to capture free electrons through dissociative electron attachment. However, given that there is a chance that there could be a larger error in the triple probe measurements of the electron temperature, this error would carry through the calculations of the electron density in addition to any other error on the

measured ion current that might be associated to the source(s) of error in the electron temperature measurements; the relation of the electron density and the measured electron temperature is given by Eqn. 3.25. Unfortunately, there were no other experimental measurements made of the electron density, but simulations results provided some insight into the expected electron temperature and densities based on the global kinetics of the species in the discharge. It is important to note that even if the absolute values of the triple probe measurements were inaccurate, the effects of changes in the gas pressure, gas composition, and power of the microwave beam in discharges containing oxygen were similar to those observed in Ar-N_2 discharges. Spatial electron temperature and density profiles of discharges containing oxygen are shown in Figs. 5.10 and 5.11; note that measurements shown were conducted under similar conditions (200 mTorr and 96% Ar) to those shown in Fig. 5.7.

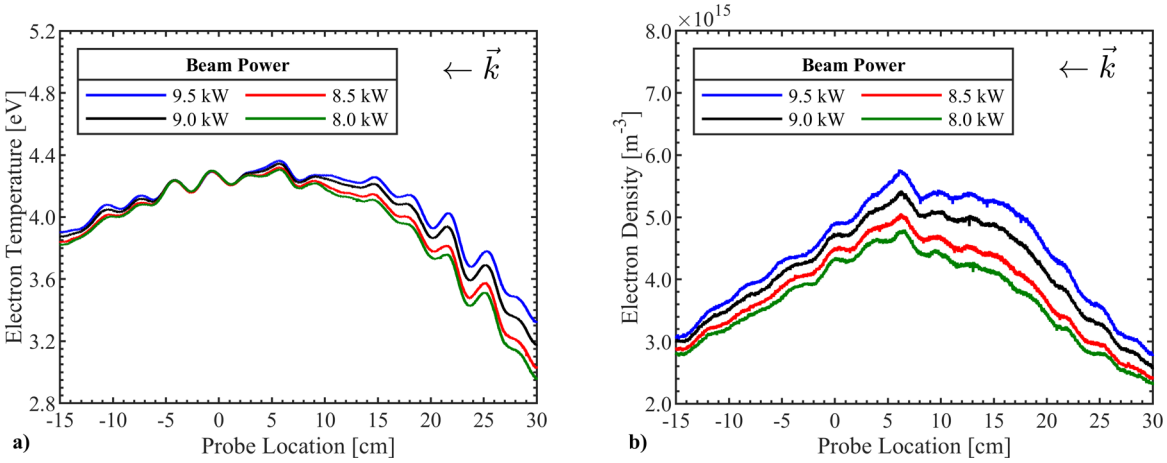

Figure 5.10: Spatially resolved electron **a)** temperature and **b)** density measurements of stable Ar-O_2 (4% O_2) plasma generated at 200 mTorr with various input microwave beam powers.

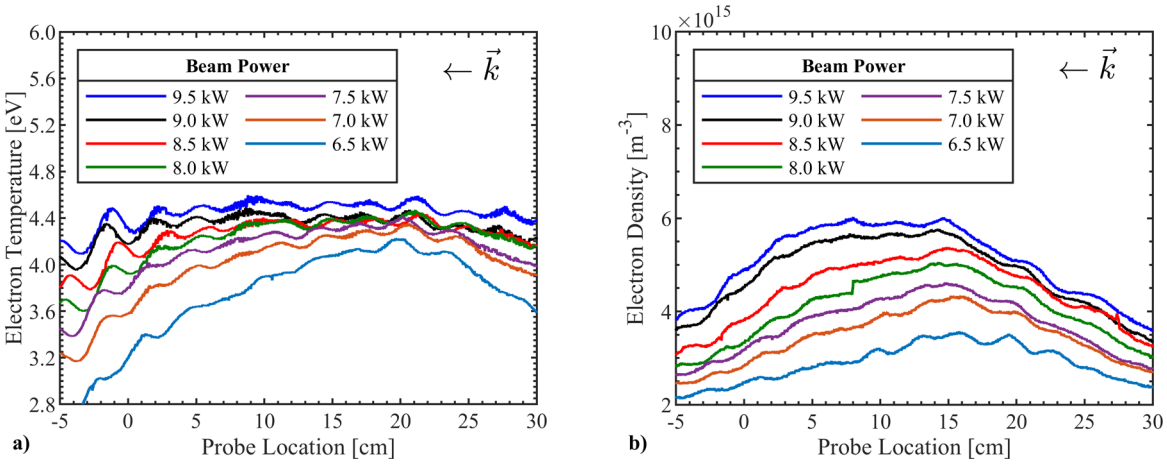

Figure 5.11: Spatially resolved electron **a)** temperature and **b)** density measurements of stable Ar-N_2-O_2 (2% N_2, 2% O_2) plasma generated at 200 mTorr with various input microwave beam powers.

The electron temperature was also calculated from optical emission spectroscopy measurements of light emitted from the decay of excited argon atoms using a CRM. While this diagnostic method is non-invasive, the measurement is an averaged over the line-of-sight of the collection optics; the spatial resolution is not as good as that of an electrostatic probe. In general, the electron temperature calculated from spectral measurements of Ar-N_2 discharges was within error of the average electron temperature measured by triple probe; a comparison of these measurements is shown in Fig. 5.12. Unfortunately, the same could not be said of measurements of the discharges containing oxygen as on average the measurements were off by approximately 2 eV (approximately 1 eV for error bars to overlap). It is unclear which of the two diagnostic methods is the more accurate when measuring the electron temperature in discharges containing oxygen; the probe measurements did not account for the presence of negative ions, and the CRM did not account for argon interactions with the molecular gases. A comparison of the electron temperatures calculated by the CRM and measured by the triple probe in Ar-O_2 and Ar-N_2-O_2 discharges is shown in Fig. 5.13 and 5.14.

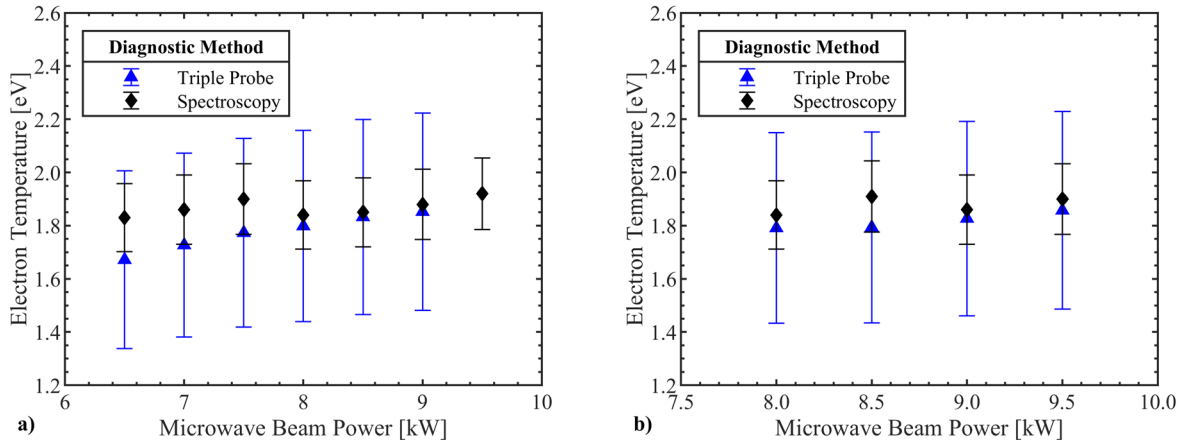

Figure 5.12: Average electron temperature of a stable Ar-N_2 (6% N_2) plasma at **a)** 200 mTorr and **b)** 150 mTorr measured by optical emission spectroscopy and floating triple probe methods.

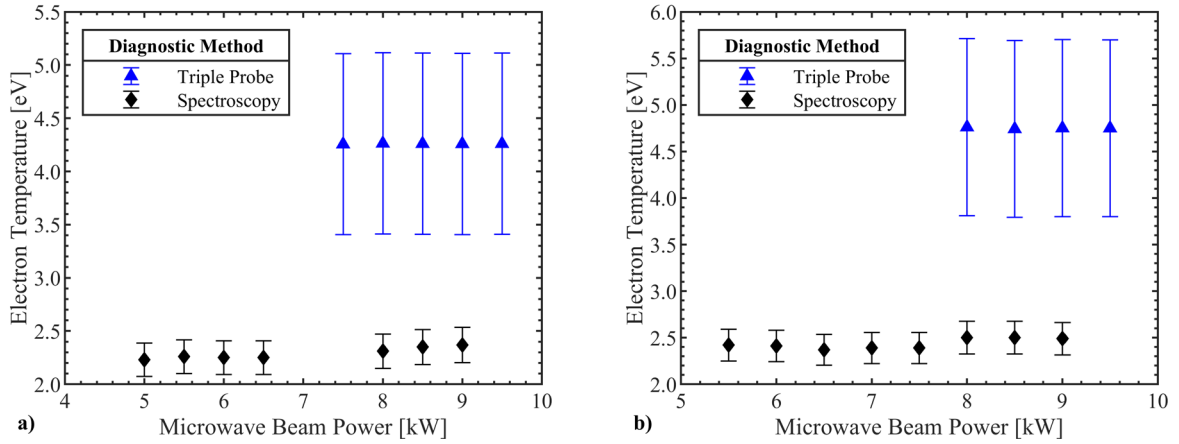

Figure 5.13: Average electron temperature of a stable Ar-O_2 (2% O_2) plasma at **a)** 200 mTorr and **b)** 150 mTorr measured by optical emission spectroscopy and floating triple probe methods.

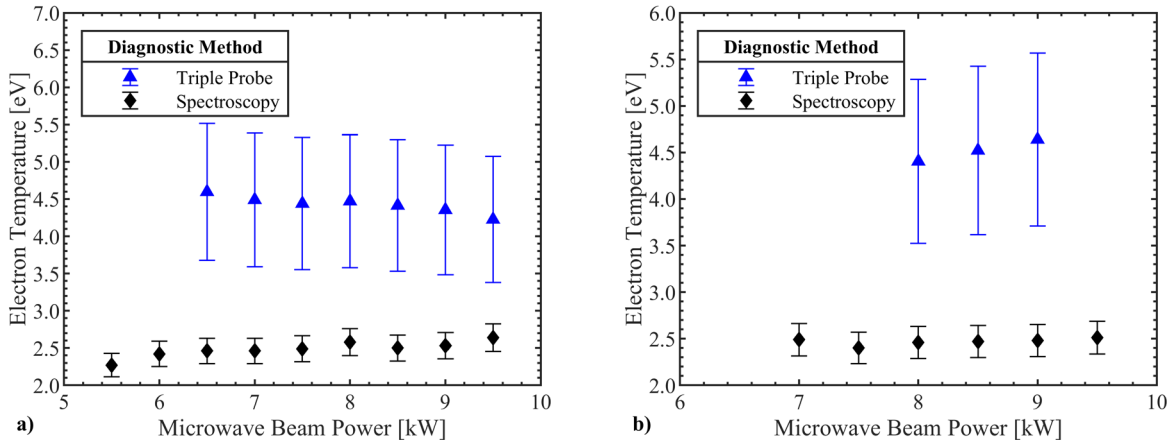

Figure 5.14: Average electron temperature of a stable Ar-N_2-O_2 (2% N_2, 2% O_2) plasma at **a)** 200 mTorr and **b)** 150 mTorr measured by optical emission spectroscopy and floating triple probe methods.

5.2.4 Scaling Parameter

The E/N_g ($V\text{-}cm^2$) ratio is the scaling parameter for electric fields in low temperature discharges. In microwave discharges the effective E/N_g ratio is given by

$$\left(\frac{E}{N_g}\right)_{eff} = \frac{\sqrt{2}E_{rms}}{N_g}\sqrt{\frac{\nu_c^2}{\nu_c^2+\omega^2}}\,, \tag{5.3}$$

where E_{rms} is the root-mean-square (RMS) electric field of the microwave beam and ω is the angular frequency of the microwave beam. An 11.8 kV/m RMS electric field was estimated near the microwave beam's geometric focus from low power measurements in vacuum conditions scaled to an input power of 10 kW. The RMS electric fields were also estimated for input powers as low at 4 kW; the estimated RMS electric fields ranged from 7.5 kV/m to 11.8 kV/m for input powers ranging from 4 kW to 10 kW. The collision frequency was calculated from

$$\nu_c = k_m N_g\,, \tag{5.4}$$

where k_m is the rate coefficient for momentum transfer. The rate coefficient was approximated as 3×10^{-8} cm^3/s for elastic, electron-neutral collisions for electron energies in the range of 1 eV to 3 eV.[71] The neutral gas density (cm^{-3}) was calculated from

$$N_g = 2.687 \times 10^{19}\left(\frac{273 p_g}{760 T_g}\right), \tag{5.5}$$

where p_g and T_g are the gas pressure and temperature, respectively. For discharges containing nitrogen, the gas temperature was estimated from the 2-0 band of nitrogen's first positive system; the gas temperature ranged between 350 K to 550 K for most of the tested conditions.

For Ar-N_2 discharges the effective E/N ratio was estimated to be between 1.1 Td to 1.7 Td when using the RMS electric field measured near the geometric focus of the microwave beam; note that 1 Td = 10^{-17} $V\text{-}cm^2$. The average electron temperature and density increased as the E/N ratio increased for E/N values calculated at 200 mTorr. At 150 mTorr the same trend was

observed, but the electron density was lower than those measured at 200 mTorr for similar E/N values; these trends are shown in Fig. 5.15. This disagreement could be because the approximations assumed a constant electric field throughout the discharge, when in reality the electric field varied along the length of the discharge. Furthermore, the approximations did not take into account changes in the size and location (relative to the beam's geometric focus) of the discharge, which would affect the average electric field within the discharge. Better agreement between the 200 mTorr and 150 mTorr results would require an increase and decrease in the E/N ratios estimated for the 200 mTorr and 150 mTorr tested conditions, respectively.

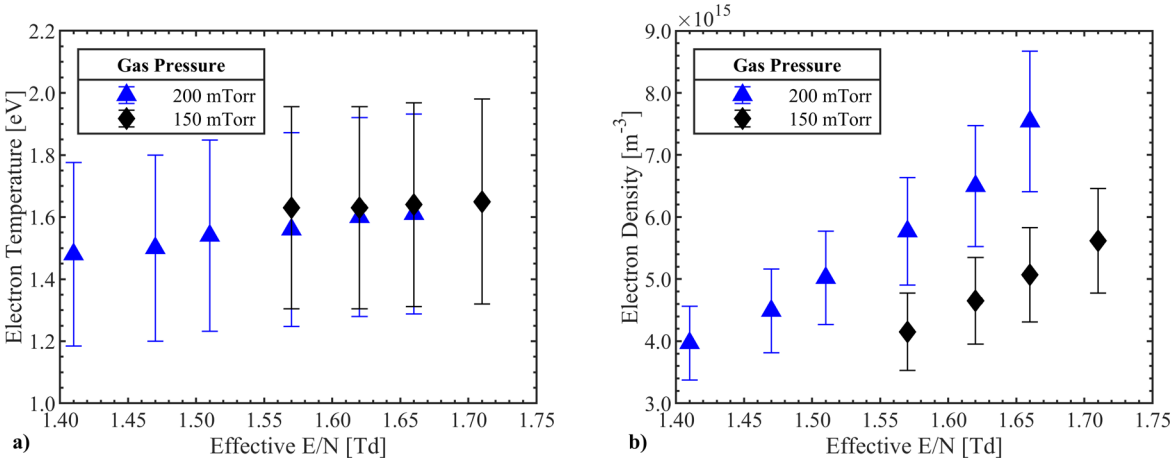

Figure 5.15: Average electron **a)** temperature and **b)** density as a function of the effective E/N ratio for Ar-N_2 (6% N_2) discharges generated at the focus of CW microwave beam.

5.3 GlobalKin Simulations

GlobalKin, a zero-dimensional global kinetics model, was used to simulate discharges under similar conditions to those present in the AFRL's experimental setup. The global model has an internal Boltzmann's equation solver that determines the electron energy distributions based on a set of initial conditions provided by the user; the frequency at which the Boltzmann's equation is solved thereafter can be set by the user. These solutions are then used to determine the rate coefficients of the reactions (from a look up table) necessary to solve the rate and energy balance

equations. A more thorough description of the global model, including the rate and energy balance equations solved by the model, can be found in the studies of Lietz and Huang.[131], [132]

Given that the global model is zero-dimensional, the spatial effects could not be simulated. However, by simulating inductively couple plasmas under similar operational conditions (gas pressure, composition, flow rate, and absorbed power) as those in the AFRL's experimental setup, rough estimates of the densities and temperatures of the electrons, ions, and neutrals were obtained. The main challenge with the simulations was determining the proper input parameters for the simulations; gas pressure, composition, and flow rate were straightforward parameters, but the size of the discharge and the power absorbed require some consideration. In *GlobalKin*, the size of the discharge is assumed to be the same as the size of the cylindrical discharge vessel, but discharges generated in the AFRL's experimental setup do not occupy the entire volume of the vacuum chamber. It was determined, from simulations conducted with various discharge vessel dimensions, that using the characteristic lengths (e.g., the diameter of the beam at its focus) of the microwave beam profile resulted in the most reasonable plasma parameters.

5.3.1 Discharge Vessel Dimensions

The diameter of a microwave beam near the beam's geometric focus was approximated from the location at which the percent of the peak amplitude of the electric field component fell to approximately 22.4%.[8] The amplitude of the electric field near the beam's geometric focus was measured by Hoff *et al*.; however, they only measured down to where field drops to approximately 30% of its peak amplitude, so a Gaussian curve was fit to the data to predict the location at which

[8] Note that there are different ways of estimating the diameter of the beam at its focus: some use the FWHM of the intensity profile, others use the locations at which the peak intensity falls to $1/e^2$ (approximately 13.5%). In this investigation it was decided to use most of the beam's intensity profile, so the beam diameter was defined by a 95% drop in the peak intensity, which translates to a 77.6% drop in the magnitude of the peak electric field; note that the intensity is proportional to the magnitude of the electric field squared.

the amplitude drops to 22.4%.[2] CST Microwave Studio simulations of the RF electric field magnitudes at the beam's geometric focus conducted by Hoff *et al*. predicted a slightly narrower beam profile than the one predicted from measurements, so the 25.6 cm beam diameter predicted from measurements was favored in this case and used in the *GlobalKin* simulations. A comparison of the measured and predicted electric field profiles is shown in Fig. 5.16.

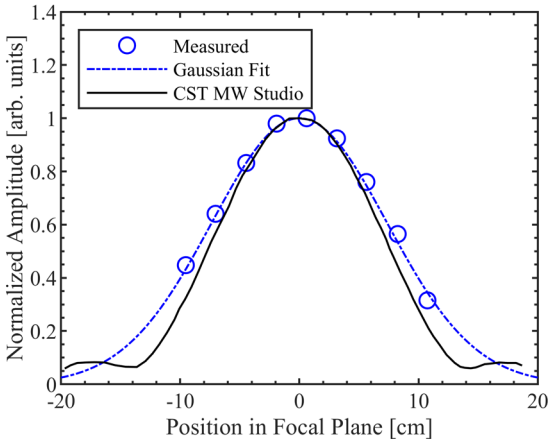

Figure 5.16: RF electric field magnitudes at the beam's geometric focus. Data from Hoff *et al*. was used in the making of this figure.[2]

The Rayleigh length is the distance from the focus at which the wavefront curvature is a maximum; this distance is defined by the location at which the beam radius increases by a factor of $\sqrt{2}$ relative to the radius at the beam's focus. Assuming a Gaussian beam profile, the Rayleigh length is given by

$$z_R = \frac{\pi w_0^2}{\lambda}\ , \tag{5.6}$$

where w_0 is the radius of the beam at its geometric focus, and λ is the wavelength of the microwave beam. The confocal parameter (two times the Rayleigh length) of the microwave beam was taken as a reasonable length of the cylindrical discharge vessel in the simulations. However, the confocal parameter was larger than the distance between the borosilicate windows in the experimental setup, so the actual length of the chamber was used instead in the simulations. The length and radius of

the cylindrical discharge plasma boundaries were set to 130 cm and 12.8 cm, respectively, as an approximation to the average volume of the discharges generated in the experimental setup.

5.3.2 Absorbed Power

Estimates of the microwave power absorbed by the plasma were made by calculating the spatial change in power, $e^{-2k_i x}$, where k_i is the imaginary component of the wavenumber, k. The dispersion relation of an electromagnetic wave traveling through a partially ionized, unmagnetized plasma is given by

$$k^2 = \frac{1}{c^2}\left(\omega^2 - \frac{\omega_p^2}{1 - i\nu_c/\omega}\right). \tag{5.7}$$

The plasma frequency was calculated from the triple probe electron density measurements and averaged over distances equal to one-tenth of the microwave wavelength; this distance was determined by the step size at which the numerical solutions converged. The collision frequency was calculated from Eqn. 5.4 using neutral gas density values determined from experimental gas temperature measurements; note that the gas temperature measurements were made from the 2-0 band of nitrogen's first positive system, so for Ar-O_2 discharges the gas temperature was assumed to be 400 ± 50 K.

Once the attenuation of the electric field is calculated, the power absorbed by the discharge can be approximated by the time averaged Poynting vector relation

$$\langle S \rangle = \frac{1}{2}\varepsilon_0 c E_0^2 , \tag{5.8}$$

where E_0 is the peak electric field. Here it was assumed that the defocusing effects of the discharge were negligible and that all power losses were to the discharge. Initial electric field values were determined from electric field measurements performed by Hoff *et al*. for the beam in free space;

a 11.8 kV/m RMS electric field was calculated for a 10 kW microwave beam near the focus.[2] Note that the square of the RMS electric field is given by

$$E_{rms}^2 = \frac{1}{2} E_0^2 , \tag{5.9}$$

which can directly be substituted into Eqn. 5.8 for quick scaling of the electric field with changes in power of the beam.

5.3.3 Reacting Species

GlobalKin allows the user to select the species to be included in the simulation, which are then used to determine the reactions included in the simulation from an extensive database of reactions. Simulations of Ar-N_2 discharges took into consideration 19 reacting species and 233 reactions; a list of the reacting species is provided in Table 5.1. For Ar-O_2 discharges, 24 species and 345 reactions were included in the simulations; a list of the reacting species is provided in Table 5.2. Lastly, 37 species and 601 reactions were included in the simulations of Ar-N_2-O_2 discharges; a list of the reacting species is provided in Table 5.3.

Table 5.1: Species included in simulations of Ar-N_2 discharges.

State	Species			
Ground:	Ar	N_2	N	—
Excited:	Ar4s($^1P_1$)	Ar4s($^3P_0$)	Ar4s($^3P_1$)	Ar4s($^3P_2$)
	Ar(4p)	Ar(4d)	Ar_2*	$N_2(\upsilon)$
	N_2*	N_2**	N*	—
Charged:	e^-	N^+	N_2^+	Ar^+
	Ar_2^+	—	—	—

Table 5.2: Species included in simulations of Ar-O_2 discharges.

State	Species			
Ground:	Ar	O_2	O	O_3
Excited:	Ar4s($^1P_1$)	Ar4s($^3P_0$)	Ar4s($^3P_1$)	Ar4s($^3P_2$)
	Ar(4p)	Ar(4d)	Ar_2*	O_2(υ)
	O_2*	O_2*(1s)	O*	O(1s)
Charged:	e^-	Ar^+	Ar_2^+	O_2^+
	O^+	O_2^-	O^-	O_3^-

Table 5.3: Species included in simulations of Ar-N_2-O_2 discharges.

State	Species			
Ground:	Ar	N_2	N	O_2
	O	O_3	N_2O	NO_2
	NO	—	—	—
Excited:	Ar4s($^1P_1$)	Ar4s($^3P_0$)	Ar4s($^3P_1$)	Ar4s($^3P_2$)
	Ar(4p)	Ar(4d)	Ar_2*	N_2(υ)
	N_2*	N_2**	N*	O_2(υ)
	O_2*	O_2*(1s)	O*	O(1s)
Charged:	e^-	Ar^+	Ar_2^+	N^+
	N_2^+	O_2^+	O^+	O_2^-
	O^-	O_3^-	N_2O^+	NO^+

5.3.4 Results

In general, simulations of Ar-N_2, Ar-O_2, and Ar-N_2-O_2 discharges showed similar trends in the electron temperature and density as those observed in triple probe measurements when the molecular gas concentration was increased at fixed input power and pressure; an example of these trends from the simulations conducted are shown in Fig. 5.17. There was also agreement in the trend of the changes in electron temperature as the gas pressure was varied; electron temperature increased as gas pressure increased. However, there was disagreement in the trends of the electron density as the gas pressure was varied. In the experiments, the electron density decreased as the

gas pressure decreased, while in the simulations the electron density increased; simulation results of the electron temperature and density at different gas pressures are shown in Fig. 5.18.

This disagreement could be due to the fact that the volume of the discharge vessel was kept constant in all the simulated conditions, while in the experiments the volume of the discharge increased as the pressure decreased; the decrease in the electron density would be as a result of a decrease in the absorbed power per unit volume (assuming the total absorbed power remained unchanged). This was confirmed by simulations conducted for determining the dimensions of the discharge vessel, where the electron density decreased as the volume of the discharge vessel increased; results of simulations these simulations are shown in Fig. 5.19. The electron density increased by approximately 6% for every 50 mTorr the gas pressure was decreased, which is relatively small compared to the 32% decrease in the electron density obtained from a small increase in the radius of the discharge vessel (12.8 cm to 15 cm). Based on these results, it is reasonable to assume that a matching trend of the electron density could be obtained if the volume of the discharge was adjusted to account for expansion of the discharge that result from a decrease in the gas pressure.

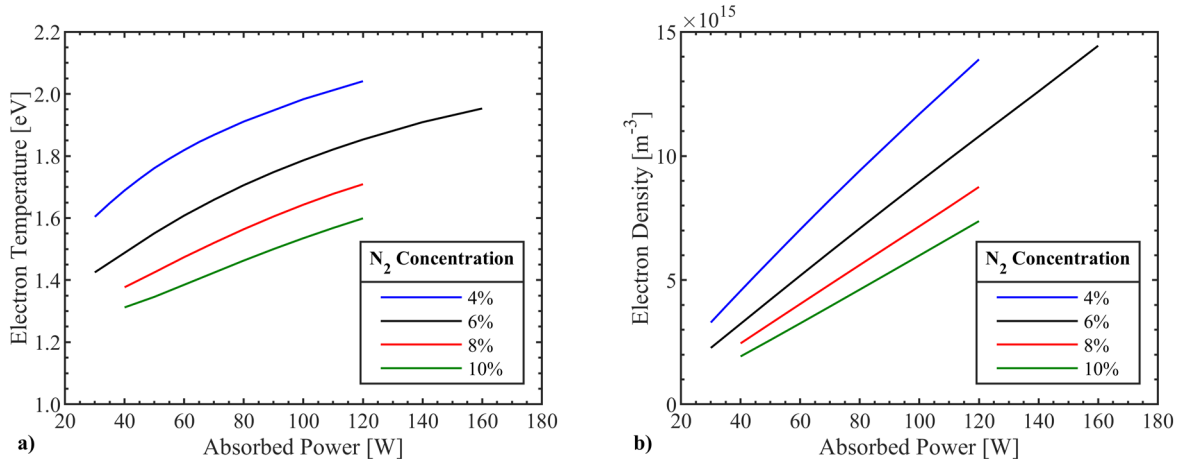

Figure 5.17: *GlobalKin* results of the **a)** electron temperature and **b)** density as a function of absorbed power. The Ar-N_2 discharge was simulated at 200 mTorr for various concentrations of nitrogen.

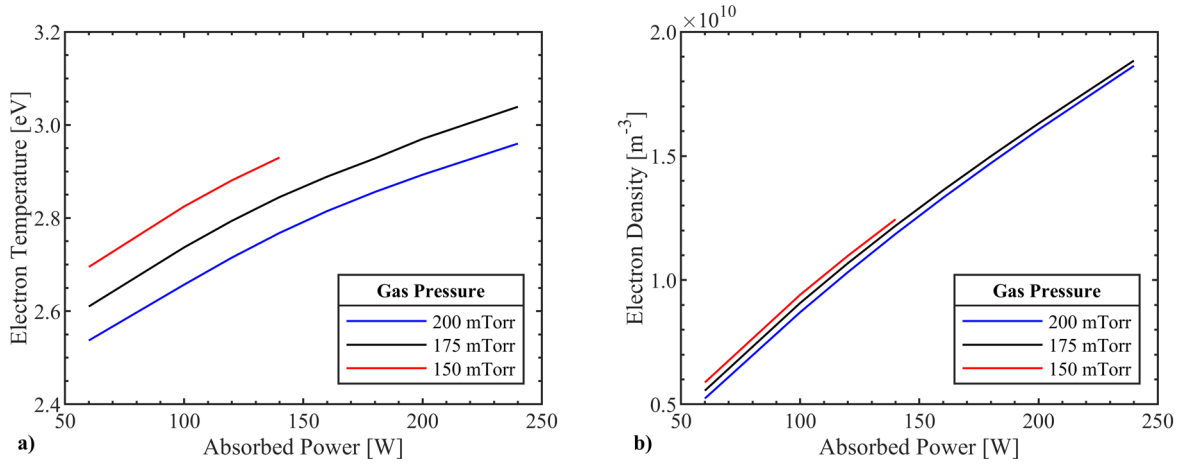

Figure 5.18: *GlobalKin* results of the **a)** electron temperature and **b)** density as a function of absorbed power. The Ar-O_2 (2% O_2) discharges were simulated at 150, 175, and 200 mTorr.

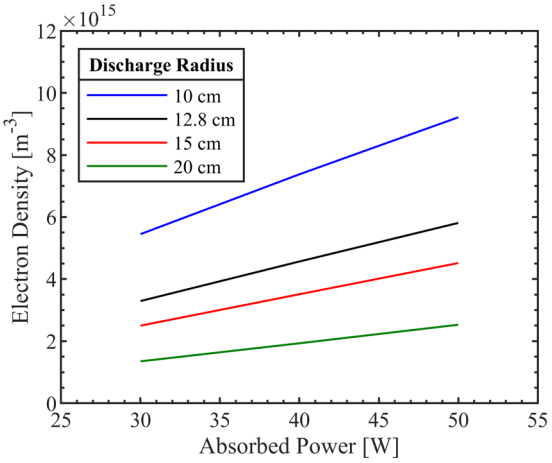

Figure 5.19: Electron densities predicted by *GlobalKin* simulations of Ar-N_2 discharges at 200 mTorr. The radius of the discharge vessel was the only parameter varied in this study.

There was good agreement in the values of the electron temperature and density predicted by the simulations to those measured experimentally for Ar-N_2 discharges. *GlobalKin* simulations assume a homogeneous discharge that fills the volume of the discharge vessel, while the discharges produced in the AFRL's experimental setup are inhomogeneous (gradients in the electron temperature and density) and do not fill the volume of the discharge vessel so they have plenty of room to expand. This leads to the question of whether the simulation results are a better representation of the peak or average measured plasma parameters. The average of the plasma parameters was taken over six wavelengths (38.4 cm) centered at the peak density; not all probe

measurements were taken over the same length, so to keep consistency between averages a fixed length was determined. From Figs. 5.20 and 5.21, it can be seen that the measured peak electron temperature closely aligned with the simulated values and that on average its values were slightly closer to the predicted values than the average electron temperature measured. On the other hand, the measured average electron density values are closer to the predicted values than the measured peak electron density values.

Simulations conducted to determine the discharge vessel dimensions, showed that the electron temperature of the discharge decreased as the discharge vessel increased in size (at fixed absorbed power); the predicted electron temperatures of this study are shown in Fig. 5.22. This suggests that a slight increase in the volume of the discharge vessel for each simulated condition would improve the agreement between experimental and simulated results. Technically, the same could be achieved in the other direction, but if one recalls from Sect. 4.3, the discharge increased in size as the power of the microwave beam was increased, so increasing the volume would be a more reasonable approach to take. Furthermore, the difference between the peak electron density values and the predicted values increased as the absorbed power increased, which meant that the volume would have to decrease more at higher absorbed powers than at lower; this would go against the behavior observed in the experiments.

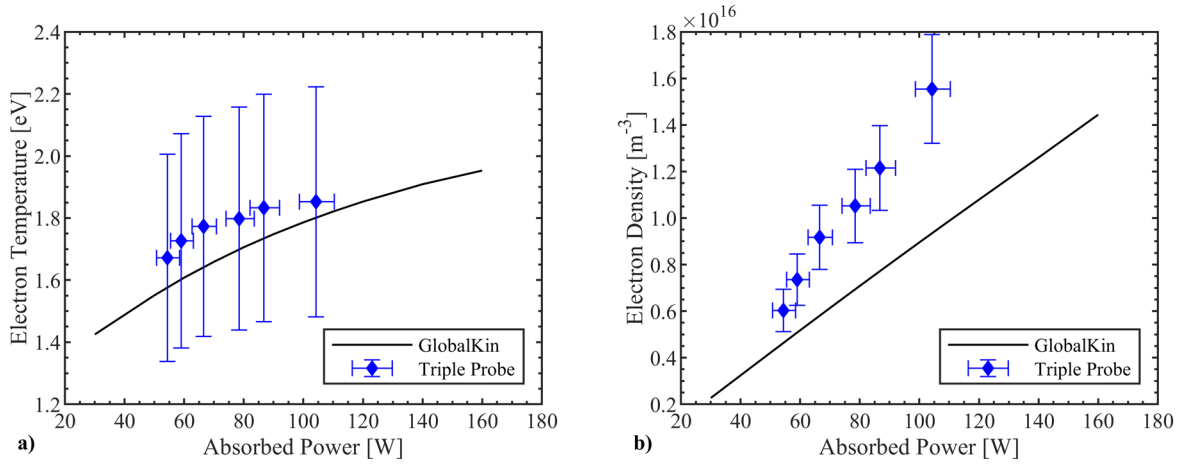

Figure 5.20: *GlobalKin* and triple probe results of the **a)** peak electron temperature and **b)** density as a function of absorbed power. The Ar-N_2 (6% N_2) discharges were simulated at 200 mTorr.

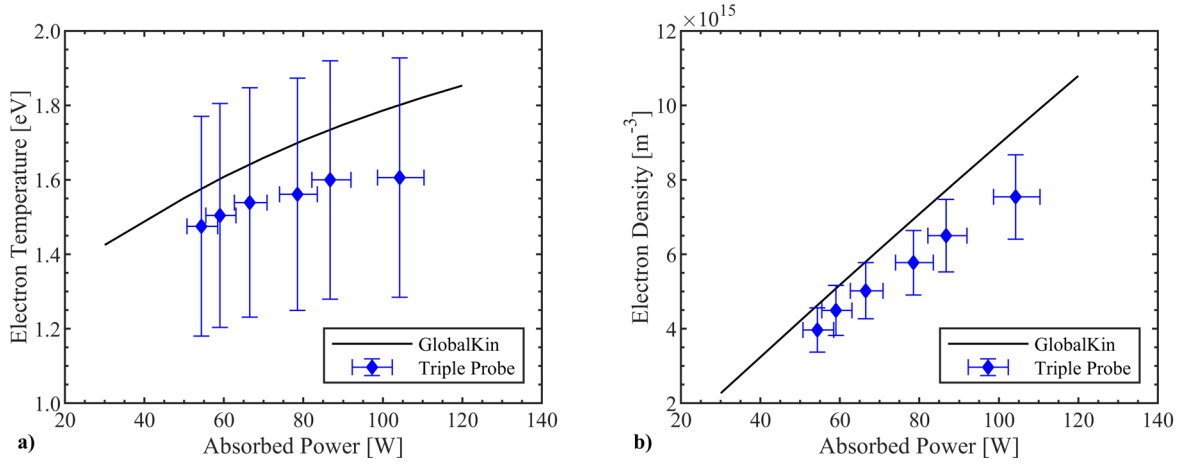

Figure 5.21: *GlobalKin* and triple probe results of the **a)** average electron temperature and **b)** density as a function of absorbed power. The Ar-N_2 (6% N_2) discharges were simulated at 200 mTorr.

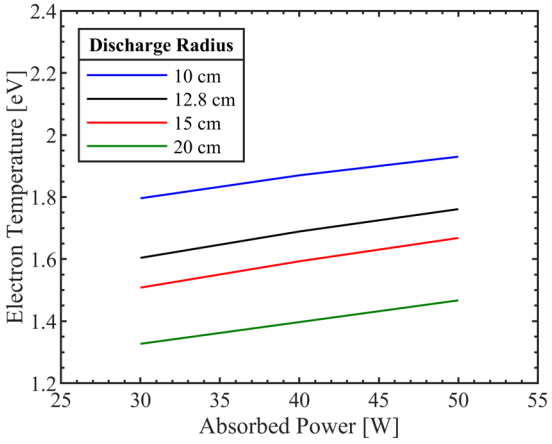

Figure 5.22: Electron temperatures predicted by *GlobalKin* simulations of Ar-N_2 discharges at 200 mTorr. The radius of the discharge vessel was the only parameter varied in this study.

Simulations of Ar-O_2 and Ar-N_2-O_2 discharges were also conducted for all tested conditions, but the agreement was not as good as in Ar-N_2 discharges. The disagreement between triple probe and simulated results was evident in the electron temperature where the average difference is in the order of 160%. The electron temperatures predicted by the simulations are much closer to the electron temperatures obtained from the optical emission spectroscopy measurements than the probe measurements, which suggests the triple probe overestimated the electron temperature. It is unclear to what extent this overestimation affected the electron density other than through the error in the electron temperature, especially since there are no other experimental measurements of the electron density to compare the results to. A comparison with simulations would be difficult to make given that the approximation of the absorbed power depends on the electron density, so any errors in the electron density measurements would also carry on to the approximation of the absorbed power. Examples of the typical comparison of experimental and simulated plasma parameters in Ar-O_2 and Ar-N_2-O_2 discharges are shown in Figs. 5.23 and 5.24.

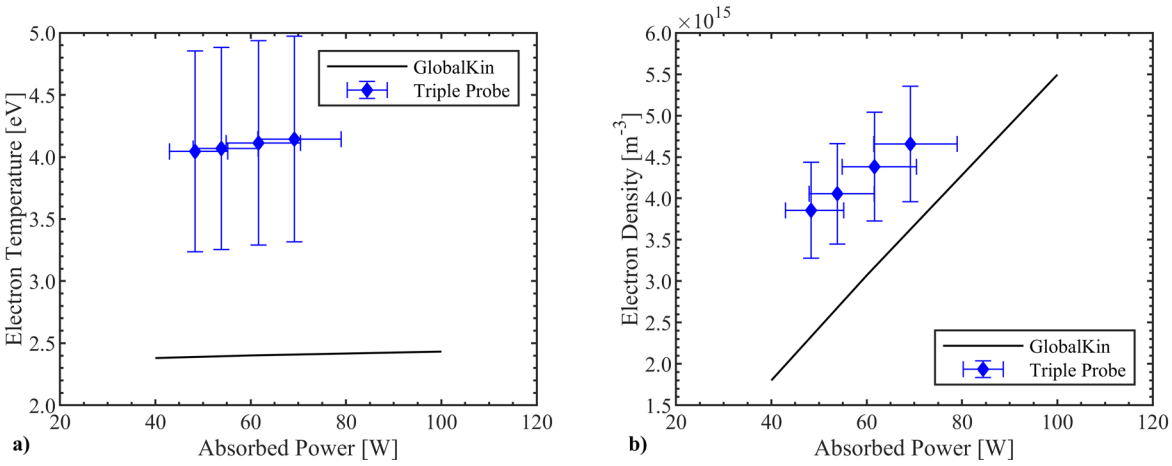

Figure 5.23: *GlobalKin* and triple probe results of the **a)** average electron temperature and **b)** density as a function of absorbed power. The Ar-O_2 (4% O_2) discharges were simulated at 200 mTorr.

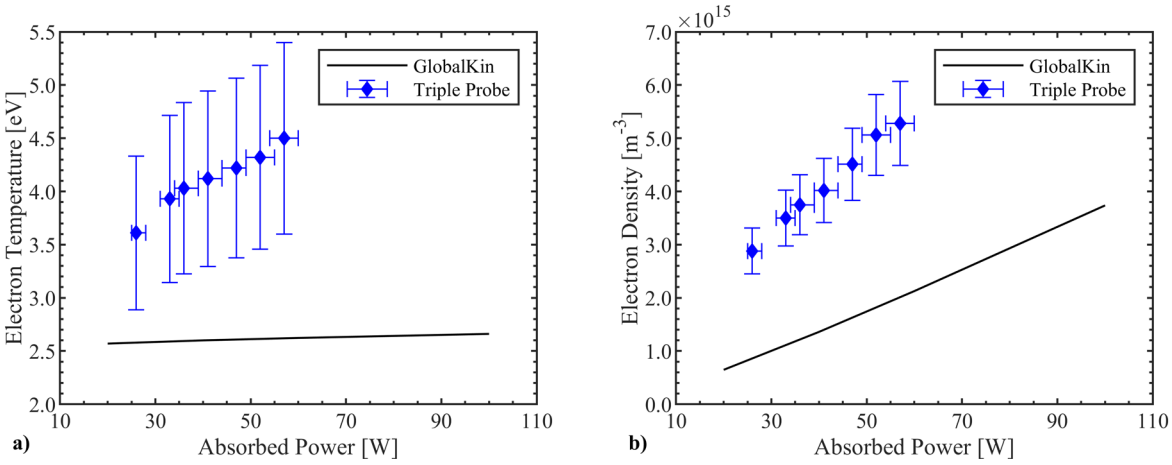

Figure 5.24: *GlobalKin* and triple probe results of the **a)** average electron temperature and **b)** density as a function of absorbed power. The Ar-N_2-O_2 (2% N_2, 2% O_2) discharges were simulated at 200 mTorr.

5.4 Closing Comments

Striated discharges have been studied for over a century and are still not fully understood due to the diverse conditions and patterns in which they have been observed. While there are similarities in the behavior and properties exhibited by striated discharges, the source of the instability can vary between type of discharge system. While the source(s) of the striated discharges observed in the AFRL's experimental setup have still not been determined, the results from studies conducted to data suggest that standing waves within the discharge might be the cause of the striations in the discharge. Results that support that hypothesis so far include:

1. Distances between the striations measured through images captured by the fast frame camera are approximately equal to half the wavelength of the microwave beam.
2. Distances between the periodic spatial oscillations of the electron temperature and density are approximately half the wavelength of the microwave beam near the center of the discharge (where pattern #2 is observed).
3. Two-dimensional and one-dimensional simulations of the discharge (no chamber) conducted by Reid showed a periodic spatial variations in the electron density and electric field that resembled a standing wave pattern.[133]

Additional experiments are planned for the future that should provide a better insight into the source of the striations.

Experimental measurements of the electron temperature and density in Ar-N_2 discharges were in good agreement with values predicted by *GlobalKin* simulations. Unfortunately, the same could not be said of the Ar-O_2 and Ar-N_2-O_2 discharges where results suggested the presence of oxygen in the discharge affected the triple probe measurements, which appeared to overestimate the electron temperatures. While there was disagreement in the values of the electron temperature and densities in discharges containing oxygen, the trends of the measured plasma parameters were the same throughout all three gas mixtures. Furthermore, it was noted that some of the disagreements observed between simulations and experiments could be fixed by providing more realistic inputs to the simulation, like adjusting the size of the discharge vessel for every simulated condition. By matching simulations results to experimental results there is the possibility that the volume of the discharge could be approximated more accurately, which could provide some insight into the parameters (other than the beam profile) that influence the size of discharges generated at the focus of microwave beams.

Chapter VI

Concluding Remarks

6.1 Conclusion

There are limited studies reported in the literature of CW microwave discharges generated in laboratory conditions. This dissertation research expanded on the investigations of Hoff *et al*. providing new insights into the behavior and properties of discharges generated at the focus of CW microwave beams.[2] The effects of gas pressure, gas composition, and power of the microwave beam on the behavior and characteristics of the discharge were the focus of this investigation. It was determined that the stability of discharges generated in the experimental setup could be controlled by adjusting the gas composition and power of the microwave beam; the combinations of the control parameters that yield stables discharges in the AFRL's experimental setup are provided in this investigation. While the exact cause of the instabilities observed is not fully understood, triple probe results presented in this investigation suggest that a multi-step process might be responsible for the transitions between stable and quasi-stable discharges; thermal instabilities are currently being considered as a possible initial source of the quasi-stable discharges.[71], [94], [95]

The studies of striated stable discharges showed that there were similarities between the striations observed in microwave discharges and the striations reported in DC and RF glow discharges. Among the similarities was the anticorrelation between the electron temperatures and densities measured along the length of the striated pattern observed near the center of the discharge.

The main differences were the fact that the striations in the AFRL's experimental setup formed along the direction of the microwave beam propagation vector, while those reported in DC and RF glow discharges formed along the direction of the electric field. Another noticeable difference was that up to three different striation patterns were observed simultaneously in microwave discharges compared to the one periodic pattern commonly reported in DC and RF glow discharges. While the exact physics of striation formation is not fully understood, a combination of the results presented in this investigation and results from the studies of Reid, suggest that the striation patterns observed in the AFRL's experimental setup could be caused by standing waves that develop within the discharge boundaries.[133] Additional experiments are planned that should provide an answer to whether or not striations in the discharges observed in this investigation are caused by standing waves.

Characterization of the stable discharges resulted in good agreement between experimental (probe and spectroscopy) and simulated results in Ar-N_2 discharges; however, the same could not be said of the Ar-O_2 and Ar-N_2-O_2 discharges. Results from discharges containing oxygen suggest that the presence of oxygen in the discharge affected the triple probe measurements. It is unclear what precisely in the oxygen was causing the overestimation of the electron temperature, given that the concentration of negative oxygen ions (O^-, O_2^-, and O_3^-) was expected to be too low in the discharges to have any significant effect on the probe measurements. The expected low concentration of negative oxygen ions was confirmed by *GlobalKin* simulations, which predicted negative oxygen ions only make up approximately 5% of the negative species population in discharges formed from Ar-O_2 gas mixtures containing 8% molecular oxygen; electronegative plasmas usually have negative ion densities on the same order of magnitude or higher than the electron density. While the presence of oxygen caused significant error in the measured values of

the electron temperature and density, the measured plasma parameters followed the same trends as Ar-N_2 discharges when exposed to changes in the gas pressure, concentration of the molecular gas, and power of the microwave beam.

In general, the observed trends in the electron temperature and density included:

1. Electron temperature and density increased as the power of the microwave beam increased.
2. Electron temperature and density decreased as the concentration of the molecular gases increased in the discharge.
3. Electron temperature decreased as the gas pressure increased, while the electron density increased.

All but one of these trends were also observed in the *GlobalKin* simulations. This discrepancy could be attributed to the fact that the volume of the discharge vessel was kept constant for all simulated conditions. While *GlobalKin* did not take the effects of electromagnetic waves have in a discharge (e.g., microwave reflections, and spatial variations of plasma parameter) into consideration, the predicted electron temperatures and densities in Ar-N_2 discharges were remarkably close to the average values measured by the triple probe. Furthermore, the electron temperatures predicted by *GlobalKin* in discharges containing oxygen were within error of those calculated from optical emission spectroscopy measurements, suggesting that the electron densities predicted by the model are likely to be within a small percent from the real values as well.

6.2 Future Work

There is still a lot to learn from the CW microwave-driven discharges generated at the AFRL, especially from quasi-stable discharges. There are plans to make improvements to the

plasma diagnostic systems and methods in order to characterize the ionization fronts observed in quasi-stable discharges. Optical emission spectroscopy will be used to measure the electron temperature and the gas temperature (in discharges containing nitrogen) of the ionization front as it passes over the collection optics. Spectral measurements will need to be made at various locations in order to track how the plasma temperatures evolve as the ionization front propagates upstream of the microwave beam's geometric focus. While non-invasive diagnostic methods are preferred when characterizing quasi-stable discharges, there are plans to use an improved triple probe system as well.

The improved triple probe system will be designed to reduce its effects on the discharge and microwave beam; its success at achieving this will be evaluated based on its ability to take measurements in the same conditions as the spectroscopy system. If successful, all the measurements conducted for this investigation will be retaken to assess the extent of the disturbances from the probe used in this work. Furthermore, the improved probe would allow for studies on the evolution of electron temperature and density of quasi-stable discharges to be conducted along the path of the ionization fronts produced; this could provide some insight into the source of the rapid increase in electron density in quasi-stable discharges.

In regard to discharge stability, experiments to measure the relative change in the electric field strength along the length of the discharge are planned for the future. A coaxial RF probe (also known as a Lecher wire probe) was constructed for this experiment based on a design proposed by Ellis to measure electromagnetic radiation in gas discharges.[134] Results from these experiments will provide the last piece of information needed to determine the source of the striations observed in microwave discharges generated at the AFRL.

Additional *GlobalKin* simulations will also be conducted in the future to study the changes in the size of stable discharges as the gas pressure, the concentration of the molecular gases and power of the microwave beam are varied. The approach that will be taken in this study is to vary the volume of the simulated discharge vessel until the predicted plasma parameters match the average values measured by the triple probe; this should provide some insight into how much the discharge is changing in size as the control parameters are varied. Something that would help improve the accuracy of the comparison would be arrays of detectors to measure the transmitted and reflected power directly instead of relying on probe measurements for approximations of the absorbed power. Microwave interferometry would be another way of improving the accuracy of the comparison as it would allow measurements of electron density to be taken non-invasively; the main challenge with this method is designing a system with high enough resolution capable of resolving the periodic variations in the density at a reasonable cost.

There are plans to add a second translation stage to the experimental setup, which would expand the type of experiments one can perform in the setup. An example of an experiment that could be performed with a second translation stage is a study to determine the distance from the discharge a wall can be before it starts affecting the characteristics of the discharge. This could be done by attaching a piece of material (conductor or dielectric) to the secondary stage and measuring changes in the discharge as the surface moves closer to the discharge; measurements could be done with invasive and non-invasive methods for comparison purposes. Another experiment that could be performed with the addition of a secondary linear translation stage is a three-dimensional mapping of the discharge assuming the discharge is radially symmetrical. This would provide a more accurate and complete characterization of the discharge and how it changes as the control parameters are varied.

Appendix A

Triple Probe Data Processing MATLAB Scripts

MATLAB scrip used for analysis of triple probe data. Note that the code uses a function called intersections.m written by Douglas M. Schwarz that can be downloaded from the MATLAB file exchange. Other than the aforementioned function, this code calls two other functions written by the author; these are provided at the end of the main script.

MAIN SCRIPT:

```
% Calculates the electron temperature and density from collected TLP data.
% Outputs cell containing the electron temperatures and densities at
% all measured locations for every input file.
% Input MAT-files contain raw data in [m x 3] arrays, where the first
% column contains the time stamp, the second column the measured Vd
% (voltage potential between the positive and floating probe), and the
% third column the voltage drop across the load resistor between the
% positive and negative probes.
% Input MAT-files must be named as "Test_X.mat" where "X" is a number
% between 1 and infinity (e.g. Test_1.mat, Test_2.mat, Test_3.mat, etc).

%-------------------------------------------------------------------------
% Author: Adrian Lopez
% Email: alopz@umich.edu
%-------------------------------------------------------------------------

%=========================================================================
%-------------------------- Required Inputs ------------------------------
%=========================================================================

% File range of interest - this are the "X" values of the files name
fstart = 1;       % Starting file number
fend = 8;         % Ending file number

% Gas Composition Information
N2_p = 0.02;      % Percent of N2 in gas mixture
O2_p = 0.00;      % Percent of O2 in gas mixture
```

```
% Probe Information
RL = 96.2;        % Load Resistor [Ohms]
L = 8.0;          % Probe length [mm]
r = 0.508;        % Probe radius [mm]

% DAQ noise
Vnoise = 0.0001;    % Average DAQ noise across load resistor channel [V]

% Translation Stage Information
d = 15;           % Max probe location downstream from geometric focus [cm]
v = 0.265;        % Translation stage speed [cm/s]

%=========================================================================
%---------------------------- End of Inputs ----------------------------
%=========================================================================

Data_Folder = uigetdir(path,'Select folder containing the data MAT-files');
if Data_Folder == 0
   clearvars
   return
end
tic

% Mass of particles
Ar = 39.948;         % Mass of Ar in amu
N2 = 28.013;         % Mass of N2 in amu
O2 = 31.998;         % Mass of O2 in amu
me = 9.109e-31;      % Mass of electron in kg

% Variables calculated from initial inputs
Ar_p = 1-N2_p-O2_p;                  % Percent of Ar in gas mixture
M = Ar_p*Ar+N2_p*N2+O2_p*O2;         % Effective gas mass in amu
S = 2*pi*r*L+pi*r^2;                 % Surface area [mm2] - cylindrical probe
k = 0.657*(1.67e-27*M/me)^0.5;       % Constant used in (27) - Sin-Li Chen 1971
nfiles = fend-fstart+1;              % Total # of files to analyze

% Variables with set initial values
Rp = 1;                  % Sets initial probe radius to Debye length ratio
jj = 1;                  % Sets initial index value
R0 = cell(1,nfiles);     % Creates cell for storing results

% Solves the correction factor for rp <= 4.6 - value is constant
eta0 = TLP_Correction_Factor(M,Rp);

% Outputs the linear fit values of Te as a function of Vd for rp <= 4.6
```

```
P0 = TLP_Corrected_Te(eta0);

% Main for-loop that loads MAT-files and analyze them one at a time
for j = fstart:fend
    disp(j)

    % Loads MAT-files
    filename = ['Test_',num2str(j),'.mat'];
    data = load(fullfile(Data_Folder,filename));
    data = cell2mat(struct2cell(data));

    % Assigns data column vectors from MAT-file to new variables
    tstamp = data(:,1);  % Time stamp data
    Vd = data(:,2);      % Potential between positive and floating probes
    Vdrop = data(:,3);   % Measured voltage drop across load resistor

    % Data corrections/conversions
    VdropC = Vdrop-Vnoise;      % Subtracts average DAQ noise from Vdrop
    dL = data(:,1).*v-d;        % Converts time stamps to distance

    % Smooths out data through a moving mean
    Vd = movmean(Vd,1000);
    VdropC = movmean(VdropC,1000);

    % Calculates the electron temperature and density without correction
    % factor - Sin-Li Chen 1965
    Te = Vd./log(2);                                    % Electron temperature [eV]
    I = 1e6.*VdropC./RL;                                % Current through load resistor [µA]
    f = 1.05e9.*Te.^(-0.5).*(exp(log(2))-1).^(-1);      % Intermediate calculation
    ne = M^0.5.*I.*f./S;                                % Electron density [cm-3]

    % Calculates probe radius to Debye length ratio for correction factor
    D_L = 7434.*(Te./ne).^0.5;     % Debye length [mm]
    rp = round(r./D_L,1);          % Probe radius to Debye length ratio

    % Downsample data to reduce runtime of code - no data features are lost
    Vd = downsample(Vd,3);
    I = downsample(I,3);
    rp = downsample(rp,3);
    dL = downsample(dL,3);
    Te = downsample(Te,3);

    % Corrects the electron temperature and density assuming rp <= 4.6 at
    % all measured locations - Sin-Li Chen 1971
    TeC = polyval(P0,Vd);                               % Corrected electron temperature [eV]
    lwf = lambertw(2*exp(2/eta0+1)/(eta0*k^2));         % Lamber-W Function
```

```
Vf = (2+eta0-eta0.*lwf)./(2*eta0);                    % Intermediate calculations
df = exp(Vd./TeC)-(1-eta0.*Vd./TeC).^0.5;
f =  1.05e9.*TeC.^(-0.5).*(1-eta0.*Vf+eta0/2).^0.5./df;
neC = M^0.5.*I.*f./S;                                 % Corrected ne [cm-3]

% Additional corrections for results where rp > 4.6 - Sin-Li Chen 1971
ndx = rp>4.6;           % Creates logical array based on rp > 4.6
if max(ndx)             % Makes additional corrections if ndx is "True"
   subRp = rp(ndx);    % Creates array with rp values where ndx is "True"
   subVd = Vd(ndx);  % Creates array with Vd values where ndx is "True"
   subI = I(ndx);       % Creates array with I values where ndx is "True"

   % Creates arrays to store corrected Te and ne values
   subne = zeros(1,length(subRp));
   subTe = zeros(1,length(subRp));

   % Solves for correction factor corresponding to subRp(1)
   eta1 = TLP_Correction_Factor(M,subRp(1));

   % Outputs the linear fit values of Te(Vd) for subRp(1)
   P1 = TLP_Corrected_Te(eta1);

   % Initial value to conditional statement
   rp_chk = subRp(1);

   % Determines # of iterations to be performed
   m = length(subRp);

   % Loop for additional corrections corresponding to rp > 4.6
   for kk = 1:m
      disp(kk)

      % Skips recalculating eta1 and P1 if subRp does not change
      if rp_chk == subRp(kk)
         subTe(kk) = polyval(P1,subVd(kk));  % Corrected Te [eV]
         lwf = lambertw(2*exp(2/eta1+1)/(eta1*k^2));
         Vf = (2+eta1-eta1*lwf)/(2*eta1);
         df = subTe(kk).^(0.5).*(exp(subVd(kk)./subTe(kk))...
             -(1-eta1.*subVd(kk)./subTe(kk)).^0.5);
         f =  1.05e9*(1-eta1.*Vf+eta1/2)^0.5./df;
         subne(kk) = M^0.5.*subI(kk).*f./S;   % Corrected ne [cm-3]

      % Recalculates eta1 and P1 for new subRp value
      else
         eta1 = TLP_Correction_Factor(M,subRp(kk));
         P1 = TLP_Corrected_Te(eta1);
```

```
            subTe(kk) = polyval(P1,subVd(kk));                    % Corrected Te [eV]
            lwf = lambertw(2*exp(2/eta1+1)/(k^2*eta1));
            Vf = (2+eta1-eta1.*lwf)./(2*eta1);
            df = subTe(kk).^(0.5).*(exp(subVd(kk)./subTe(kk))...
                -(1-eta1.*subVd(kk)./subTe(kk)).^0.5);
            f =  1.05e9.*(1-eta1.*Vf+eta1/2).^0.5./df;
            subne(kk) = M^0.5.*subI(kk).*f./S;                    % Corrected ne [cm-3]
        end

        rp_chk = subRp(kk);
    end

    % Updates corrected values in main results vector
    TeC(ndx) = subTe;
    neC(ndx) = subne;
end

% Flips distance column to account for the direction the probe is moving
if mod(j,2) == 0        % RL - Direction
    % Do nothing
else
    dL = flipud(dL);   % LR - Direction
end

% Stores all results in cell
R0{jj} = [dL,TeC,neC];

jj = jj+1;
end
toc
clearvars -except R0
```

Function 1 of 2:

```
% Correction factor, eta, for triple probe measurements
function eta = TLP_Correction_Factor(M,Rp)

me = 9.109e-31;  % mass of electron in kg

k = 0.65*(1.67e-27*M/me)^0.5;
k1 = 0.73*(1.67e-27*M/me)^0.5;

% Ion sheath radius to probe radius ratio
q = [1 1.01 1.02 1.04 1.06 1.08 1.1 1.15 1.2 1.3 1.4 1.5 1.6 1.7 1.8...
    1.9 2 2.1 2.2 2.3 2.4 2.5 2.6 2.7 2.8 2.9 3 3.2 3.4 3.6 3.8 4];

% Values for corresponding q - Langmuir (1923)
B = [0 0.0001 0.0004 0.00159 0.00356 0.00630 0.00980 0.02186 0.03849 ...
    0.08504 0.14856 0.2282 0.3233 0.4332 0.5572 0.6947 0.8454 1.0086 ...
    1.1840 1.3712 1.5697 1.7792 1.9995 2.2301 2.4708 2.7214 2.9814 ...
    3.5293 4.1126 4.7298 5.3795 6.0601];

% Fit polynomial to B^2 for 1 < q < 4.1
p = polyfit(q',B',8);

% New table of values for q and B^2
q1 = (1:0.001:2)';
q1_2 = q1.^2;

B1 = polyval(p,q1);
B1 = abs(B1);

if Rp < 4.7
    % For rp < 4.7, eta is apprx. constant
    eta = 1/(lambertw(2*k1^2));

else
    % For rp >=4.7, eta changes exponentially
    y = (0.97*Rp^2.*B1.*q1).^(2/3)+0.5;

    yf = (0.5:0.01:10)';
    qf = k./exp(yf);
    qf_2 = qf.^2;

    [zx0,zy0] = intersections(y,q1_2,yf,qf_2,false);

    xf = (0:0.1:20)';
    y1 = zx0+0.5;
```

```
    y1 = y1.*ones(size(xf));
    y2 = zx0-0.5;
    y2 = y2.*ones(size(xf));

    [~, zy1] = intersections(y,q1_2,y1,xf,false);
    [~, zy2] = intersections(y,q1_2,y2,xf,false);

    eta = (zy1-zy2)/zy0;
end
```

Function 2 of 2:

```
% Calculates the Te and ne with correction factor
function P = TLP_Corrected_Te(eta)

T_min = 0.5;
T_max = 4;
T = (T_min:0.01:T_max).';

Vd3 = 37.20;
Vd2_min = 1;
Vd2_max = 2;

Vd2 = (Vd2_min:0.01:Vd2_max).';
[m,~] = size(Vd2);
TeC = ones(size(Vd2));


for j = 1:m
LS = exp(-Vd2(j,1)./T).*(sqrt(1-eta.*Vd2(j,1)./T)...
   +sqrt(1+eta.*(Vd3-Vd2(j,1))./T));
RS = ones(size(T));

[T1,~] = intersections(T,LS,T,RS,false);

TeC(j,1) = T1;

end

P = polyfit(Vd2,TeC,1);

clearvars -except P
```

Appendix B

Modifications to Biloiu's Model

Modified version of the N2Spectra.m script used in Biloiu's model.

```
% This code is written for the paper
% 'Gas Temperature Determination from fits of the 0-0,1-0, and 2-0
% bands of the first positive system of nitrogen' of C.Biloiu et al
% by X. Sun (xsun@mix.wvu.edu), Mar. 2006

%=============================================
%---------------------------- Modifications ----------------------------
%=============================================
% Modified by: Adrian Lopez, May 2019
% E-mail:     alopz@umich.edu

% - Removes Ar I lines from 2-0 band and replace it with numerically
%   generated data from input guesses
%    - Use the 771.3 and 773.0 nm lines as reference for fitted guess
% - Changed lsqcurvefit to nlinfit
%    - Needed for error bar calculations of Tr
% - Outputs the 95% confidence interval for the Tr parameter
% - Removed unnecessary commands

%=============================================
%-----------------------------------------------------------------------
%=============================================

function [coef,data,cinterval]=N2Spectra(band,data_exist, fitting,...
                    parameters,J_ranges,coef_init,lambda, real_intens)

global param head_num J_stsp
param = parameters;
head_num = band;
J_stsp = J_ranges;

% Create a zero array with same size as real_intens
fitting_intens = zeros(size(real_intens));
```

```
% coef: rotation temperature,background level, wvlngth shift, strength
coef = coef_init;                    % Initial guess
coef(4) = 1500;
strength = coef(4);
cal_intens = Trans_XTo0(coef, lambda);  % Theoretical calculation

% Find the peak value of band head
if (head_num == 0)
   bh_wvlngth = 1051.00;
end
if (head_num == 1)
   bh_wvlngth = 891.24;
end
if (head_num == 2)
   bh_wvlngth = 775.32;
end
[lngth, ~] = size(lambda);
delta_lambda = (lambda(lngth)-lambda(1))/lngth;
index_pos = 1;
while (lambda(index_pos)<bh_wvlngth)
   index_pos = index_pos+1;
end

% Normalize intensities to the peak value of the band head
low_range = index_pos - fix(0.5/delta_lambda);
up_range = index_pos + fix(0.5/delta_lambda);
peak_bandhead = max(real_intens(low_range:up_range));
norm_real_intens = real_intens *100.0 / peak_bandhead;
peak_bandhead2 = max(cal_intens(low_range:up_range));
norm_cal_intens = cal_intens *100.0 / peak_bandhead2;

%=========================================================================
%------------------------------------------ Removes Ar I Peaks ------------------------------------
%=========================================================================
[~,n0] = max(norm_real_intens);
ndx_min = n0-30;
ndx_max = n0+28;
norm_real_intens(ndx_min:ndx_max) = norm_cal_intens(ndx_min:ndx_max);
%=========================================================================
%------------------------------------------ End of Modification -----------------------------------
%=========================================================================
cinterval = 0;
% Calculates best fit spectra for input spectra
if (fitting == 1)
   % guess the strength
   coef(4) = strength*100.0/peak_bandhead2;
```

```
%=========================================================================
%------------------------ Modified Fit and Confidence Interval Calculation ------------------------
%=========================================================================
   % Added options for increased accuracy of the fit
   opts = statset('nlinfit');
   opts.MaxIter = 1000;
   opts.TolFun = 1e-10;
   opts.TolX = 1e-10;

   [coef,residual,~,covP] = nlinfit(lambda,norm_real_intens,...
                          @Trans_XTo0, coef,opts);
   fitting_intens = Trans_XTo0(coef, lambda);
   cinterval = nlparci(coef,residual,'covar',covP);
end
%=========================================================================
%------------------------------------------ End of Modification ------------------------------------
%=========================================================================

% plotting the original data
   plot(lambda, norm_cal_intens, 'b');
   hold on

if (data_exist == 1)
   plot(lambda,norm_real_intens, 'r');
   hold on
end

if (fitting == 1)
   plot(lambda,fitting_intens, 'k');
   sse = sum(residual.^2);
   sst = sum((norm_real_intens-mean(norm_real_intens)).^2);
   r_square = 1-sse/sst;
   strcat('R_Square is :', num2str(r_square))
end
hold off

%save
data = [lambda'; norm_real_intens'; fitting_intens'];
```

Bibliography

[1] A. F. Aleksandrov, A. A. Kuzovnikov, and V. M. Shibkov, "Freely Localized SHF Discharge in a Focused Beam," *Inzhernerno-Fizicheskii Zhurnal*, vol. 62, no. 5, pp. 726–732, 1992.

[2] B. W. Hoff *et al.*, "Apparatus for generating quasi-free-space microwave-driven plasmas," *Rev. Sci. Instrum.*, vol. 87, no. 3, 2016.

[3] H. M. Mott-Smith and I. Langmuir, "The theory of collectors in gaseous discharges," *Phys. Rev.*, vol. 28, no. 4, pp. 727–763, 1926.

[4] J. G. Laframboise, "Theory of Spherical and Cylindrical Langmuir Probes in a Collisionless, Maxwellian Plasma at Rest," 1966.

[5] J. D. Swift and J. R. Schwar, *Electrical Probes for Plasma Diagnostics*. American Elsevier, 1969.

[6] E. V. Shun'ko, *Langmuir Probe in Theory and Practice*. Universal Publishers, Boca Raton, FL, 2008.

[7] F. F. Chen, "Langmuir Probe Diagnostics," in *Mini-Course on Plasma Diagnostics, IEEE ICOPS*, 2003.

[8] P. M. Bryant, "Theory of cylindrical Langmuir probes in weakly ionized, non-thermal, stationary and moderately collisional plasmas," *Plasma Sources Sci. Technol.*, vol. 18, no. 014013, 2009.

[9] V. I. Demidov, S. V. Ratynskaia, and K. Rypdal, "Electric probes for plasmas: The link between theory and instrument," *Rev. Sci. Instrum.*, vol. 73, no. 10, p. 3409, 2002.

[10] R. L. Merlino, "Understanding Langmuir probe current-voltage characteristics," *Am. J. Phys.*, vol. 75, no. 12, pp. 1078–1085, 2007.

[11] V. A. Godyak and B. M. Alexandrovich, "Comparative analyses of plasma probe diagnostics techniques," *J. Appl. Phys.*, vol. 118, no. 233302, 2015.

[12] E. O. Johnson and L. Malter, "A Floating Double Probe Method for Measurements in Gas Discharges," *Phys. Rev.*, vol. 80, no. 1, pp. 58–68, 1950.

[13] K. Yamamoto and T. Okuda, "On the Floating Probe Method for the Measurement of Ionized Gas," *J. Phys. Soc. Japan*, vol. 11, no. 1, pp. 57–68, 1956.

[14] J. L. Jauberteau and I. Jauberteau, "Floating double probe in non-Maxwellian plasmas: Determination of the electron density and mean electron energy," *Contrib. to Plasma Phys.*, vol. 58, pp. 239–251, 2018.

[15] T. Welzel, T. Dunger, H. Kupfer, and F. Richter, "A time-resolved Langmuir double-probe method for the investigation of pulsed magnetron discharges," *J. Appl. Phys.*, vol. 96, no. 12, pp. 6994–7001, 2004.

[16] T. Okuda and K. Yamamoto, "Asymmetrical Triple Probe Method for Determining Energy Distribution of Electron in Plasma," *J. Appl. Phys.*, vol. 31, no. 1, pp. 158–162, 1960.

[17] J. D. Swift, "Asymmetrical double-probe systems," *J. Phys. D. Appl. Phys.*, vol. 2, pp. 134–136, 1969.

[18] H. Amemiya and G. Fuchs, “Range of application for asymmetric double probes,” *Jpn. J. Appl. Phys.*, vol. 30, no. 12A, pp. 3531–3532, 1991.
[19] S. Saito, M. A. Razzak, S. Takamura, and M. R. Talukder, “Development of asymmetric double probe formula and its application for collisional plasmas,” *J. Appl. Phys.*, vol. 107, no. 123306, 2010.
[20] F. F. Chen and J. P. Chang, *Lecture Notes on Principles of Plasma Processing*. Springer, 2003.
[21] B. E. Cherrington, “The Use of Electrostatic Probes for Plasma Diagnostics-A review,” *Plasma Chem. Plasma Process.*, vol. 2, no. 2, pp. 113–140, 1982.
[22] N. Hershkowitz, *How Langmuir Probes Work*. 2013.
[23] J. Asmussen, R. Mallavarpu, J. R. Hamann, and H. C. Park, “The Design of a Microwave Plasma Cavity,” *Proc. IEEE*, vol. 62, no. 1, pp. 109–117, 1974.
[24] R. Mallavarpu, J. Asmussen, and M. C. Hawley, “Behavior of a microwave cavity discharge over a wide range of pressures and flow rates,” *IEEE Trans. Plasma Sci.*, vol. 6, no. 4, pp. 341–354, 1978.
[25] J. Asmussen, “Electron cyclotron resonance microwave discharges for etching and thin-film deposition,” *J. Vac. Sci. Technol. A Vacuum, Surfaces, Film.*, vol. 7, no. 3, pp. 883–893, 1989.
[26] S. S. Zuo, M. K. Yaran, T. A. Grotjohn, D. K. Reinhard, and J. Asmussen, “Investigation of diamond deposition uniformity and quality for freestanding film and substrate applications,” *Diam. Relat. Mater.*, vol. 17, no. 3, pp. 300–305, 2008.
[27] S. Allison, A. L. Cullen, and A. Zavody, “A Microwave Plasma Discharge,” *Nature*, vol. 193. p. 156, 1962.
[28] C. W. Hamilton, “Sustained, localized, pulsed-microwave discharge in air,” *Nature*, vol. 188, no. 4756, pp. 1098–1099, 1960.
[29] G. M. Batanov *et al.*, “Plasma chemistry and thin film deposition in discharges excited by intense microwave beams,” *Plasma Sources Sci. Technol.*, vol. 2, no. 3, pp. 164–172, 1993.
[30] G. M. Batanov, I. A. Kossyi, N. I. Malykh, A. A. Matveev, A. V. Sapozhnikov, and V. P. Silakov, “Characteristics of microwave beam breakdown in nitrogen and oxygen,” *Tech. Phys. Lett.*, vol. 23, no. 5, pp. 405–407, 1997.
[31] G. M. Batanov, I. A. Kossyi, and V. P. Silakov, “Gas-discharge method for improving the environmental characteristics of the atmosphere (In memory of G.A. Askar’yan),” *Plasma Phys. Reports*, vol. 28, no. 3, pp. 204–228, 2002.
[32] G. A. Askaryan *et al.*, “A freely localized microwave discharge for removal of chlorofluorocarbon contamination from the atmosphere,” *J. Phys. D. Appl. Phys.*, vol. 27, no. 6, pp. 1311–1318, 1994.
[33] G. A. Askar’yan, G. M. Batanov, I. A. Kossyy, and A. Y. Kostinskiy, “Aftereffects of microwave discharges in the stratosphere,” *Sov. Phys. Usp.*, vol. 31, no. 10, pp. 957–959, 1988.
[34] K. V. Artem’ev *et al.*, “Subthreshold self-sustained discharge initiated by a microwave beam in a large volume of high- pressure gas,” *J. Phys. Conf. Ser.*, vol. 907, no. 012022, 2017.
[35] Y. Hidaka *et al.*, “Plasma structures observed in gas breakdown using a 1.5 MW, 110 GHz pulsed gyrotron,” *Phys. Plasmas*, vol. 16, no. 5, 2009.
[36] J. S. Hummelt, M. A. Shapiro, and R. J. Temkin, “Spectroscopic temperature

measurements of air breakdown plasma using a 110 GHz megawatt gyrotron beam," *Phys. Plasmas*, vol. 19, no. 12, 2012.
[37] S. C. Schaub, J. S. Hummelt, W. C. Guss, M. A. Shapiro, and R. J. Temkin, "Electron density and gas density measurements in a millimeter-wave discharge," *Phys. Plasmas*, vol. 23, no. 8, 2016.
[38] I. A. Kossyi, "No SNSS Microwave Discharge as a New Type of Large-Size Plasma Source," in *AIAA Aerospace Sciences Meeting and Exhibit*, 2006.
[39] A. F. Aleksandrov, A. S. Zarin, A. A. Kuzovnikov, V. M. Shibkov, and L. V Shibkova, "Plasma parameters of a nonself-sustained microwave discharge created by a programmed pulse," *Tech. Phys.*, vol. 42, no. 7, pp. 733–736, 1997.
[40] A. A. Kuzovnikov, V.M.Shibkov, and L. V Shibkova, "Electron kinetics in a discharge plasma produced by a focused microwave beam in free space," *Tech. Phys.*, vol. 42, no. 6, 1997.
[41] V. M. . Shibkov, A. F. Aleksandrov, A. P. Ershov, I. B. Timofeev, V. A. Chernikov, and L. V. Shibkova, "Freely localized microwave discharge in a supersonic gas flow," *Plasma Phys. Reports*, vol. 31, no. 9, pp. 795–801, 2005.
[42] A. L. Vikharev *et al.*, "Nonlinear dynamics of a freely localized microwave discharge in an electromagnetic wave beam," *Sov. Phys. JETP*, vol. 67, no. 4, pp. 724–728, 1988.
[43] A. Cook, M. Shapiro, and R. Temkin, "Pressure dependence of plasma structure in microwave gas breakdown at 110 GHz," *Appl. Phys. Lett.*, vol. 97, no. 1, pp. 3–5, 2010.
[44] A. Cook, J. Hummelt, A. Shapiro, and R. J. Temkin, "Observation of plasma array dynamics in 110 GHz milimeter-wave air breakdown," *Phys. Plasmas*, vol. 18, no. 10, p. 100704, 2011.
[45] A. M. Cook, J. S. Hummelt, M. A. Shapiro, and R. J. Temkin, "Measurements of electron avalanche formation time in W-band microwave air breakdown," *Phys. Plasmas*, vol. 18, no. 8, 2011.
[46] A. Cook, J. Hummelt, M. Shapiro, and R. J. Temkin, "Milimeter wave scattering and diffraction in 110 GHz air breakdown plasma," *Phys. Plasmas*, vol. 20, no. 4, p. 43507, 2013.
[47] Y. Hidaka, E. M. Choi, I. Mastovsky, M. A. Shapiro, J. R. Sirigiri, and R. J. Temkin, "Imaging of Atmospheric Air Breakdown Caused by a High-Power 110 GHz Pulsed Gaussin Beam," *IEEE Trans. Plasma Sci.*, vol. 36, no. 4, 2008.
[48] W. E. Kock, "Metal-Lens Antennas," *Proc. I.R.E.*, vol. 34, pp. 828–836, 1946.
[49] S. Aisenberg, "Multiple probe measurements in high-frequency plasma lasers," *J. Appl. Phys.*, vol. 35, no. 1, pp. 130–134, 1964.
[50] S. L. Chen and T. Sekiguchi, "Instantaneous direct-display system of plasma parameters by means of triple probe," *J. Appl. Phys.*, vol. 36, no. 8, pp. 2363–2375, 1965.
[51] M. A. Meier, G. A. Hallock, and R. D. Bengtson, "Turbulent Plasma by the Time-Domain Triple-Probe Method," *Contrib. to Plasma Phys.*, vol. 38, no. S, pp. 98–103, 1998.
[52] N. A. Gatsonis, L. T. Byrne, J. C. Zwahlen, E. J. Pencil, and H. Kamhawi, "Current-Mode Triple and Quadruple Langmuir Probe Methods With Applications to Flowing Pulsed Plasmas," *IEEE Trans. Plasma Sci.*, vol. 32, no. 5, pp. 2118–2129, 2004.
[53] R. Reid, "Private Communication." 2017.
[54] S. L. Chen, "Studies of the Effect of Ion Current on Instantaneous Triple-Probe Measurements," *J. Appl. Phys.*, vol. 42, no. February 1970, pp. 406–412, 1971.
[55] H.-J. Kunze, *Introduction To Plasma Spectroscopy*. Springer, 2009.

[56] J. E. Allen, R. L. F. Boyd, and P. Reynolds, “The collection of positive ions by a probe in an electrical discharge,” *Proc. R. Soc. London. Ser. A. Math. Phys. Sci.*, vol. B70, pp. 297–304, 1957.
[57] K. U. Riemann, “Bohm criterion and sheath formation,” *J. Phys. D. Appl. Phys.*, vol. 24, no. 4, pp. 493–518, 1991.
[58] I. Langmuir and K. Blodgett, “Currents Limited by Space Charge Between Coaxial Cylinders,” *Phys. Rev.*, vol. 22, p. 353, 1923.
[59] A. Thorne, *Spectrophysics*, 2nd ed. Chapman and Hall Ltd, 1988.
[60] H. R. Griem, *Principles of Plasma Spectroscopy*. Cambridge University Press, 1997.
[61] H. R. Griem, *Plasma Spectroscopy*. McGraw-Hill, 1964.
[62] J. Cooper, “Plasma spectroscopy,” *Reports Prog. Phys.*, vol. 29, pp. 34–130, 1966.
[63] G. V. Marr, *Plasma Spectroscopy*, 1st ed. Elsevier Publishing, 1968.
[64] M. Simek, “On the Use of the Numerical Simulation of the First Positive System of N_2: III. Numerical Thermometer on (v’,0) bands, v’ = 0-3,” *Res. Rep. IPPCZ - 345*, 1994.
[65] M. Simek, “On the Use of the Numerical Simulation of the First Positive System of N_2: II. Fast Trot Estimation from the Partially Resolved (3,0) Band,” *Plasma Chem. Plasma Process.*, vol. 15, no. 3, pp. 451–463, 1995.
[66] C. Biloiu, X. Sun, Z. Harvey, and E. Scime, “An alternative method for gas temperature determination in nitrogen plasmas: Fits of the bands of the first positive system ($B^3\prod_g \rightarrow A^3\Sigma_u^+$),” *J. Appl. Phys.*, vol. 101, no. 073303, 2007.
[67] R. A. Dressler, Y. Chiu, O. Zatsarinny, K. Bartschat, R. Srivastava, and L. Sharma, “Near-infrared collisional radiative model for Xe plasma electrostatic thrusters : the role of metastable atoms,” *J. Phys. D. Appl. Phys.*, vol. 42, no. 185203, 2009.
[68] M. A. Lieberman and A. J. Lichtenberg, *Principles of Plasma Discharges and Materials Processing*. John Wiley & Sons, Inc., 2005.
[69] B. H. Bransden and C. J. Joachain, *Physics of Atoms and Molecules*. John Wiley & Sons, Inc., 1983.
[70] D. J. Griffiths, *Introduction to Quantum Mechanics*. Prentice Hall, Inc., 1995.
[71] A. Fridman and L. A. Kennedy, *Plasma Physics and Engineering*, 2nd ed. CRC Press, 2011.
[72] “National Institute of Standards and Technology (NIST).” [Online]. Available: https://www.nist.gov/pml/atomic-spectra-database.
[73] G. Herzberg, *Molecular Spectra and Molecular Structure I. Spectra of Diatomic Molecules*. D. Van Nostrand Company, Inc., 1950.
[74] A. Lofthus and P. H. Krupenie, “The Spectrum of Molecular Nitrogen,” *J. Phys. Chem. Ref. Data*, vol. 6, no. 1, pp. 113–290, 1977.
[75] U. Fantz, “Basics of plasma spectroscopy,” *Plasma Sources Sci. Technol.*, vol. 15, no. 4, 2006.
[76] H.-J. Werner, J. Kalcher, and E.-A. Reinsch, “Accurate ab initio calculations of radiative transition probabilities between the $A^3\Pi_g$, $W^3\Delta_u$, $B'^3\Sigma^-_u$, and $C^3\Pi_u$ states of N_2,” *J. Chem. Phys.*, vol. 81, pp. 2420–2431, 1984.
[77] B. P. Lavrov, M. Osiac, A. V. Pipa, and J. Ropcke, “On the spectroscopic detection of neutral species in a low-pressure plasma containing boron and hydrogen,” *Plasma Sources Sci. Technol.*, vol. 12, no. 4, pp. 576–589, 2003.
[78] L. G. Piper, K. W. Holtzclaw, B. D. Green, and W. A. M. Blumberg, “Experimental determination of the Einstein coefficients for the N_2(B – A) transition,” *J. Chem. Phys.*,

vol. 90, no. 10, pp. 5337–5345, 1989.
[79] E. E. Eyler and F. M. Pipkin, “Lifetime measurements of the $B^3\Pi_g$ state of N_2 using laser excitation,” *J. Chem. Phys.*, vol. 79, no. 8, pp. 3654–3659, 1983.
[80] M. Jeunehomme, “Transition moment of the first positive band system of nitrogen,” *J. Chem. Phys.*, vol. 45, no. 5, pp. 1805–1811, 1966.
[81] R. F. Heidner, D. G. Sutton, and S. N. Suchard, “Kinetic study of $N_2(B^3\Pi_g, \upsilon)$ quenching by laser-induced fluorescence,” *Chem. Phys. Lett.*, vol. 37, no. 2, pp. 243–248, 1976.
[82] D. E. Shemansky, “$A^3\Sigma^+_u$ molecules in the N_2 afterglow,” *J. Chem. Phys.*, vol. 64, no. 2, pp. 565–580, 1976.
[83] T. A. Carlson, N. Durić, P. Erman, and M. Larsson, “Collisional Transfer to the B State in N_2,” *Phys. Scr.*, vol. 19, no. 1, pp. 25–28, 1979.
[84] Y. B. Golubovskii and V. M. Telezhko, “Measurement of Gas Temperature From the Unresolved Rotational Structure of the First Positive Band System of Nitrogen,” *J. Appl. Spectrosc.*, vol. 39, no. 3, pp. 999–1003, 1983.
[85] C. Effantin, C. Amiot, and J. Verges, “Analysis of the (0-0), (1-0), and (2-0) Bands $B^3\Pi_g \rightarrow A^3\Sigma_u^+$ System of $^{14}N_2$ and $^{15}N_2$,” *J. Mol. Spectrosc.*, vol. 76, pp. 221–265, 1979.
[86] J. B. Tatum, “The Interprentation of Intensities in Diatomic Molecular Spectra,” *Astrophys. J., Suppl. Ser.*, vol. 14, pp. 21–55, 1967.
[87] E. E. Whiting, A. Schadee, J. B. Tatum, J. T. Hougen, and R. W. Nicholls, “Recommended conventions for defining transition moments and intensity factors in diatomic molecular spectra,” *J. Mol. Spectrosc.*, vol. 80, no. 2, pp. 249–256, 1980.
[88] V. M. Donnelly, “Plasma electron temperatures and electron energy distributions measured by trace rare gases optical emission,” *J. Phys. D. Appl. Phys.*, vol. 37, pp. R217–R236, 2004.
[89] X. M. Zhu and Y. K. Pu, “A simple collisional-radiative model for low-temperature argon discharges with pressure ranging from 1 Pa to atmospheric pressure: Kinetics of Paschen 1s and 2p levels,” *J. Phys. D. Appl. Phys.*, vol. 43, no. 1, 2010.
[90] S. Siepa, S. Danko, T. V. Tsankov, T. Mussenbrock, and U. Czarnetzki, “On the OES line-ratio technique in argon and argon-containing plasmas,” *J. Phys. D. Appl. Phys.*, vol. 47, no. 44, 2014.
[91] G. F. Karabadzhak, Y. H. Chiu, and R. A. Dressler, “Passive optical diagnostic of Xe propelled Hall thrusters. II. Collisional-radiative model,” *J. Appl. Phys.*, vol. 99, no. 113305, 2006.
[92] S. Tsurubuchi, T. Miyazaki, and K. Motohashi, “Electron-impact emission cross sections of Ar,” *J. Phys. B At. Mol. Opt. Phys.*, vol. 29, pp. 1785–1801, 1996.
[93] R. R. Reid, A. Lopez, and E. Thornton, “Stability and Long Time Behavior of Plasmas Sustained in Quasi-Free-Space Using High Power Microwave Beams,” *(Pending)*, 2019.
[94] L. M. Kagan and M. C. Kelley, “ A thermal mechanism for generation of small-scale irregularities in the ionospheric E region ,” *J. Geophys. Res. Sp. Phys.*, vol. 105, no. A3, pp. 5291–5303, 2000.
[95] W. L. Nighan, “Causes of thermal instability in externally sustained molecular discharges,” *Phys. Rev. A*, vol. 15, no. 4, pp. 1701–1720, 1977.
[96] R. Reid, A. Lopez, and E. Thornton, “Doppler Velocimetry of Plasma Ionization Fronts in High Power Microwave Beams,” in *APS Division of Plasma Physics*, 2018.
[97] N. Dyatko, Y. Ionikh, and A. Napartovich, “Influence of Nitrogen Admixture on Plasma Characteristics in a dc Argon Glow Discharge and in Afterglow,” *Atoms*, vol. 7, no. 13,

2019.
[98] S. Hübner, E. Carbone, J. M. Palomares, and J. Van Der Mullen, “Afterglow of argon plasmas with H_2, O_2, N_2, and CO_2 admixtures observed by thomson scattering,” *Plasma Process. Polym.*, vol. 11, no. 5, pp. 482–488, 2014.
[99] V. Laporta, R. Celiberto, and J. Tennyson, “Resonant vibrational-excitation cross sections and rate constants for low-energy electron scattering by molecular oxygen,” *Plasma Sources Sci. Technol.*, vol. 22, no. 2, 2013.
[100] T. W. Shyn and C. J. Sweeney, “Vibrational-excitation cross sections of molecular oxygen by electron impact,” *Phys. Rev. A*, vol. 48, no. 2, pp. 1214–1217, 1993.
[101] Y. Itikawa, “Cross Sections for Electron Collisions with Oxygen Molecules,” *J. Phys. Chem. Ref. Data*, vol. 38, no. 1, pp. 1–20, 2009.
[102] M. Allan, “Measurement of absolute differential cross sections for vibrational excitation of o2 by electron impact,” *J. Phys. B At. Mol. Opt. Phys.*, vol. 28, no. 23, pp. 5163–5175, 1995.
[103] Y. Itikawa, “Cross Sections for Electron Collisions with Nitrogen Molecules,” *J. Phys. Chem. Ref. Data*, vol. 35, no. 1, pp. 32–50, 2006.
[104] G. J. Schulz, “Vibrational excitation of N_2, CO, and H_2 by electron impact,” *Phys. Rev.*, vol. 135, no. 4A, 1964.
[105] A. G. Robertson, M. T. Elford, R. W. Crompton, M. A. Morrison, W. Sun, and W. K. Trail, “Rotational and vibrational excitation of nitrogen by electron impact,” *Aust. J. Phys.*, vol. 50, no. 3, pp. 441–472, 1997.
[106] R. K. Asundi, J. D. Craggs, and M. V. Kureepa, “Electron attachment and ionization in oxygen, carbon monoxide and carbon dioxide,” *Proc. Phys. Soc.*, vol. 82, no. 6, pp. 967–978, 1963.
[107] P. H. Krupenie, “The Spectrum of Molecular Oxygen,” *J. Phys. Chem. Ref. Data*, vol. 1, no. 2, pp. 423–534, 1972.
[108] J. J. B. Abria, “Research on the laws of induction of currents by currents,” *Ann. Chim. Phys.*, vol. 7, p. 462, 1843.
[109] A. Garscadden, P. Bletzinger, and T. C. Simonen, “Dispersion and stability of moving striations,” *Phys. Fluids*, vol. 12, no. 9, pp. 1833–1844, 1969.
[110] A. J. Balloni, S. Aihara, and P. H. Sakanaka, “Observation of the ionization waves in a plasma produced by radio frequency in a magnetic mirror,” *Plasma Phys. Control. Fusion*, vol. 30, no. 12, pp. 1659–1664, 1988.
[111] S. M. A. Durrani, P. Vidaud, and D. R. Hall, “Measurements of striation formation time in an N2 α RF discharge,” *J. Plasma Phys.*, vol. 58, pp. 193–204, 1997.
[112] R. A. Goldstein, M. A. Huerta, and J. C. Nearing, “Stationary striations in an argon plasma as a bifurcation phenomenon,” *Phys. Fluids*, vol. 22, no. 2, pp. 231–240, 1979.
[113] A. V. Gurevich, K. P. Zybin, and A. V. Lukyanov, “Stationary striations developed in the ionospheric modification,” *Phys. Rev. Lett.*, vol. 75, no. 13, pp. 2622–2625, 1995.
[114] V. I. Kolobov, “Striations in rare gas plasmas,” *J. Phys. D. Appl. Phys.*, vol. 39, no. 24, 2006.
[115] H. C. J. Mulders, W. J. M. Brok, and W. W. Stoffels, “Striations in a low-pressure RF-driven argon plasma,” *IEEE Trans. Plasma Sci.*, vol. 36, no. 4 PART 1, pp. 1380–1381, 2008.
[116] H. S. Robertson and J. J. Herring, “Ambipolar diffusion in radio-frequency-excited magnetoplasmas,” *Phys. Fluids*, vol. 12, no. 4, pp. 836–839, 1969.

[117] K. Takahashi and A. Ando, “Observation of stationary plasma striation and collimated plasma transport in a 100-khz inductively coupled plasma discharge,” *IEEE Trans. Plasma Sci.*, vol. 42, no. 10, pp. 2784–2785, 2014.
[118] H. Ghomi, S. Sadrieyeh, and N. N. Safa, “A simple explanation of Schottky condition through striations,” *IEEE Trans. Plasma Sci.*, vol. 36, no. 4, pp. 1004–1005, 2008.
[119] R. Kumar, S. V. Kulkarni, and D. Bora, “Cylindrical stationary striations in surface wave produced plasma columns of argon,” *Phys. Plasmas*, vol. 14, no. 12, 2007.
[120] R. Kumar and D. Bora, “Experimental investigation of different structures of a radio frequency produced plasma column,” *Phys. Plasmas*, vol. 17, no. 4, 2010.
[121] O. A. Nerushev, S. A. Novopashin, V. V. Radchenko, G. I. Sukhinin, and V. V. Sukhovskii, “Glow Intensity Profile in a Spherically Stratified Gas Discharge,” *Plasma Phys. Reports*, vol. 29, no. 9, pp. 796–801, 2003.
[122] S. A. Novopashin, V. V. Radchenko, and S. Z. Sakhapov, “Plasma parameters of a spherically stratified gas discharge,” *J. Eng. Thermophys.*, vol. 17, no. 1, pp. 71–73, 2008.
[123] L. Pekarek, “Ionization waves (striations) in a discharge plasma,” *Uspekhi Fiz. Nauk*, vol. 94, no. 3, pp. 463–500, 1968.
[124] H. Zhu, Z. Su, and Y. Dong, “Experimental studies on striations in helium glow discharge,” *Appl. Phys. Lett.*, vol. 111, no. 054104, 2017.
[125] D. Mackey, L. Plantie, and M. M. Turner, “Instabilities and pattern formation in low temperature plasmas,” *Appl. Math. Lett.*, vol. 18, pp. 865–873, 2005.
[126] A. V. Gurevich, “Nonlinear effects in the ionosphere,” *Uspekhi Fiz. Nauk*, vol. 50, no. 11, pp. 1091–1121, 2007.
[127] W. F. Utlaut and R. Cohen, “Modifying the Ionosphere with Intense Radio Waves,” *Sci. New Ser.*, vol. 174, no. 4006, pp. 245–254, 1971.
[128] R. R. Reid, “Private Communication.” 2019.
[129] M. C. Kelley *et al.*, “Density depletions at the 10-m scale induced by the Arecibo heater,” *J. Geophys. Res.*, vol. 100, no. A9, pp. 17367–17376, 1995.
[130] G. J. M. Hagelaar, K. Hassouni, and A. Gicquel, “Interaction between the electromagnetic fields and the plasma in a microwave plasma reactor,” *J. Appl. Phys.*, vol. 96, no. 4, pp. 1819–1828, 2004.
[131] A. M. Lietz and M. J. Kushner, “Air plasma treatment of liquid covered tissue: Long timescale chemistry,” *J. Phys. D. Appl. Phys.*, vol. 49, no. 42, p. 425204, 2016.
[132] S. Huang, “Modeling of Downstream and Direct Plasma Systems for Highly Selective and Anisotropic Etching,” University of Michigan, 2019.
[133] R. Reid and A. Lopez, “Periodic Density Fluctuations in Plasmas Sustained in Focused Microwave Beams,” in *IEEE Pulsed Power and Plasma Science*, 2019.
[134] R. F. Ellis, G. D. Tsakiris, C. Z. Wang, and D. A. Boyd, “UPPER HYBRID EMISSION FROM A MAGNETIZED,” *Plasma Phys. Control. Fusion*, vol. 28, no. 1B, pp. 327–345, 1986.